

Universiteit
Leiden
The Netherlands

Novel transmitter designs for magnetic resonance imaging

Aussenhofer, S.A.

Citation
Aussenhofer, S. A. (2018, April 11). *Novel transmitter designs for magnetic resonance imaging*. Retrieved from https://hdl.handle.net/1887/61005

Version:	Not Applicable (or Unknown)
License:	Licence agreement concerning inclusion of doctoral thesis in the Institutional Repository of the University of Leiden
Downloaded from:	https://hdl.handle.net/1887/61005

Note: To cite this publication please use the final published version (if applicable).

Cover Page



Universiteit Leiden



The following handle holds various files of this Leiden University dissertation:
http://hdl.handle.net/1887/61005

Author: Aussenhofer, S.A.
Title: Novel transmitter designs for magnetic resonance imaging
Issue Date: 2018-04-11

NOVEL TRANSMITTER DESIGNS

FOR MAGNETIC RESONANCE IMAGING

NOVEL TRANSMITTER DESIGNS

FOR MAGNETIC RESONANCE IMAGING

Proefschrift

ter verkrijging van
de graad van Doctor aan de Universiteit Leiden
op gezag van Rector Magnificus Prof. mr. C.J.J.M. Stolker,
volgens besluit van het College voor Promoties
te verdedigen op 11.04.2018 om 10.00 uur

door

Sebastian Arnold AUSSENHOFER

geboren te Karlstadt, Duitsland
in 1981

promotor:	Prof. dr. A.G. Webb
co-promotor:	Prof. dr. P. Boernert
Promotiecommissie:	Prof. dr. ir. C.A.T van den Berg Universitair Medisch Centrum Utrecht
	Prof. dr. ir. J. Dankelman Technische Universiteit Delft
	Dr. ir. A.J. Nederveen Academisch Medisch Centrum Amsterdam

Copyright © 2017 by S.A. Aussenhofer

ISBN 978-94-92801-28-9

The work presented in this thesis was carried out at the C.J. Gorter Center, department of Radiology at the Leiden University Medical Center.
This research was supported by the European Community Seventh Framework Programme, project number 241711: SUB nanosecond Leverage In PET/MR ImAging (SUBLIMA).

For Annika and Changjuan

CONTENTS

1 Introduction and Outline **1**

1.1 Outline of chapters . . . 3
1.2 The History of Magnetic Resonance Imaging . . . 4
1.3 Theory of Magnetic Resonance Imaging . . . 6
1.3.1 Nuclear Spin and Magnetic Moment . . . 6
1.3.2 Nucleus in a Magnetic Field . . . 9
1.4 Conventional RF coil design . . . 13
1.5 Implications of UHF MRI on RF coil design . . . 17
1.6 Dielectric Resonator Antennas . . . 19
1.6.1 Dielectric Materials - Insulators and Conductors . . . 19
1.6.2 Dielectrics in an external electric Field . . . 20
1.6.3 The Leyden Jar . . . 22
1.6.4 The parallel plate capacitor . . . 23
1.6.5 History of Dielectric Resonators . . . 27
1.6.6 Intrinsic features of Dielectric Resonators . . . 28
1.6.7 Modes in Dielectric Resonators and their Nomenclature . . . 29
1.6.8 Dielectric Resonator Design . . . 30
1.7 Plasma Antennas . . . 35
1.7.1 Introduction to Plasma . . . 35
References . . . 39

2 Design and evaluation of a detunable water-based dielectric resonator **43**

2.1 Introduction . . . 45
2.2 Methods . . . 47
2.2.1 HEM Resonator Design . . . 47
2.2.2 Detuning the HEM Resonator . . . 49
2.2.3 Birdcage Coil . . . 51
2.2.4 Coil Characterization . . . 51
2.2.5 Electromagnetic Simulations . . . 51
2.2.6 MRI Experiments . . . 52

2.3 Results . . . 53
2.3.1 Coil Characterization . . . 53
2.3.2 Simulation Results . . . 53
2.3.3 Phantom Experiments . . . 55
2.3.4 In Vivo Results . . . 58
2.4 Discussion . . . 59
References . . . 61

3 High-permittivity solid ceramic resonators for high-field human MRI 63
3.1 Introduction . . . 65
3.2 Experiment . . . 67
3.2.1 High-permittivity ceramic materials . . . 67
3.2.2 Eletromagnetic simulations . . . 67
3.2.3 Electrical characterization . . . 67
3.2.4 MRI experiments . . . 68
3.2.5 Reference resonator . . . 68
3.3 Results . . . 69
3.3.1 Electromagnetic simulations and electrical characterization . . . 69
3.3.2 Phantom MRI measurements . . . 73
3.3.3 In vivo MRI experiments . . . 74
3.4 Discussion . . . 75
3.5 Conclusion . . . 77
References . . . 78

4 High permittivity ceramic resonators for cardiac imaging at 7.0 T 81
4.1 Introduction . . . 83
4.2 Materials and Methods . . . 84
4.2.1 Design of individual ceramic resonators . . . 84
4.2.2 Reference loop coil . . . 86
4.2.3 Electromagnetic simulations . . . 86
4.2.4 Hardware setup and characterization . . . 88
4.2.5 MRI acquisition protocol and parameters . . . 88
4.3 Results . . . 90
4.3.1 Coil characterization . . . 90
4.3.2 Single element analysis . . . 91
4.3.3 Array analysis . . . 95
4.3.4 In vivo results . . . 98

4.4 Discussion . . . 99
References . . . 101

5 Evaluation of plasma-based transmit coils for magnetic resonance 103
5.1 Introduction . . . 105
5.2 Production of the Plasma . . . 107
5.3 Results . . . 109
5.4 Discussion . . . 113
5.5 Acknowledgments . . . 115
References . . . 116

6 General Discussion and Future Developments 117
6.1 General Discussion . . . 118
6.1.1 Discussion on Dielectric Resonators . . . 118
6.1.2 Discussion on Plasma based RF Coils . . . 121
6.2 Future Developments . . . 123
6.2.1 Improved Coupling Schemes for DRAs . . . 123
6.2.2 Odd ratio DRAs . . . 124
6.2.3 Hybrid DRA / Plasma RF Coils . . . 125
6.2.4 Silent Plasma Gradient Coils . . . 126
6.2.5 Nonlinear Plasma Coils for multi-band MRI . . . 128
6.2.6 Plasma based RF shields . . . 129
6.2.7 Reconfigurable Plasma RF Coils . . . 131
6.2.8 Hybrid Plasma / Lumped Element RF Coils . . . 132
6.2.9 Double tuned Birdcage Coils . . . 133
References . . . 134

7 Acknowledgements 137

8 Bibliography 141
References . . . 142

Summary 152

Samenvatting 154

Curriculum Vitæ 157

List of Publications 159

1

Introduction and Outline

1

In this thesis new transmit systems for magnetic resonance imaging (MRI) have been studied in terms of novel resonator designs. Instead of trying to adapt established technologies from lower field strengths that are mainly based on lumped element designs it was the goal of this work to investigate alternative solutions. The higher field strength of the 7.0 Tesla MRI system and thus higher B_1 transmit frequency (~ 300 MHz) allows for designs and concepts to work that would have not been possible at lower frequencies. Especially dielectric resonators and their potential use in human MRI were investigated. The thesis closes with a truly novel resonator design based on plasma technology.

1.1. OUTLINE OF CHAPTERS

In chapter one a brief history of magnetic resonance imaging (MRI) is given followed by a review of classical RF coil design. The chapter continues with the introduction of the concept of dielectric resonators, their mode of operation and general design examples. The chapter closes with an introduction to plasma physics.

In chapter two a hybrid-electromagnetic-mode (HEM) resonator was designed and built for human wrist imaging at 7.0 Tesla. The idea was to build a first usable resonator using the dielectric properties and geometry of a common dielectric material (water) instead of using lumped element to design a MRI coil. This design was compared to a similar sized conventional MRI coil and is an elegant alternative design for quadrature fed transmit coils in MRI. Beside showing the proof of principle also a new mean of detuning this dielectric resonator has been found and worked out.

In chapter three a HEM resonator for 7.0 Tesla human digit imaging was investigated based on ceramics as a low loss dielectric material. Ceramics allows for more compact designs of dielectric resonators in human MRI. In this chapter it is furthermore shown that ceramic resonators can be double tuned simply by changing the boundary conditions.

In chapter four the concept of dielectric resonators based on low loss ceramics was further investigated. The dielectric resonator was now used in a different mode (transverse electromagnetic (TE) mode) that gives similar electric and magnetic fields like a loop coil. An eight channel transmit/receive array for cardiac imaging at 7.0 Tesla field strength was built from eight ceramic resonators. This design was compared to a conventional loop coil design of similar size in several human volunteers. Basic measures of the performance of the resonator were investigated and compared to the established loop coil design.

In chapter five a novel resonator design is described that uses a plasma as a resonator instead of dielectrics or lumped elements. This novel design allows for new concepts in MRI coil building. The basic principle of the working mechanisms is given as well as the proof of concept.

The thesis closes with chapter six with a general discussion. Furthermore, possible future developments based on the findings of this thesis are theorized.

1

1.2. THE HISTORY OF MAGNETIC RESONANCE IMAGING

SINCE the first experiments on the nuclear magnetic resonance (NMR) phenomena by Bloch [2] and Purcell [27] in 1946 and the first magnetic resonance imaging (MRI) experiments by Lauterbur [20] and Mansfield [21] MRI has been constantly in development. This development has helped to establish MRI as the gold standard for clinical imaging and provide ever better insight into the human body for diagnosis, understanding and hopefully to cure diseases.

The number of MRI examinations carried out per year in the Netherlands has been steadily increasing and is now in the order of 50 exams per 1000 population [23]. The increased need for examinations in the number of exams is not only due to an ageing population but also to the ever increasing efficiency of modern MRI machines that allow for new diagnostics and stratification.

Efficiency in MRI is proportional to the signal-to-noise ratio (SNR) [32]. The higher the SNR that a system can deliver, the faster a patient examination can be completed. Consequently, since the 1970's when Philips set out to produce a first MRI system, it has been a goal of the scientific community to increase the signal-to-noise-ratio (SNR). One way of improving the SNR is to increase the main magnetic field strength (B_0). Currently the standard clinical B_0 magnetic field strengths are 1.5 and 3.0 Tesla. In the early years of the 21st century the first 7.0 Tesla human scanners became available. It might be expected that these machines would, due to their higher magnetic field strength, inherently provide a higher SNR than their current clinical counterparts. Nevertheless, further technical development is needed for these machines to be able to deliver their full potential.

Until the introduction of 3.0 Tesla human scanners the increase of the B_0 field strength did not cause too many problems from a development perspective because the wavelength of the radio frequency (~64 MHz at 1.5 Tesla and ~128 MHz at 3.0 Tesla) of the systems used to excite the spin system was significantly longer than the dimensions of the human body. With 3.0 Tesla systems however, it was observed that although the SNR increased as would be expected due to the higher B_0, the image uniformity in some cases was not as predicted and as known from lower field MRI [9]. It soon became apparent that those image disturbances did not occur due to broken hardware of the imaging system but instead were caused by fundamental physics [37].

The number of artefacts was found to increase with increasing B_0. At 3.0 Tesla, the

presence of artefacts was to an extent that they could still be used for clinical imaging [31]. For the first 7.0 Tesla systems, the further increase in artefacts prevented their meaningful use [6, 43]. Homogeneous spin excitation within the field of view with a body coil became impossible. At higher B_0 field strengths, the corresponding electric field has a wavelength that is a fraction or a multiple of the anatomical feature being imaged. This leads to non-uniformity in the B_1 transmit field that causes shading artefacts in the images better known as dielectric effects as they can be seen in figure 1.1. To circumvent those problems it was soon understood that new means of transmit systems – preferably much closer to the anatomy – would be needed in ≥ 7.0 Tesla systems.

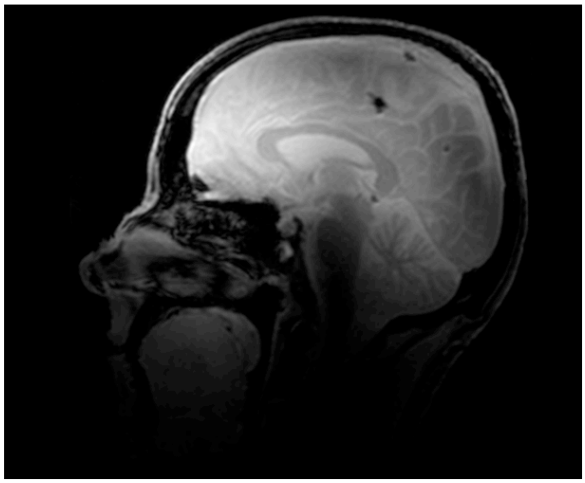


Figure 1.1: Human head MRI image acquired at 7.0 Tesla field strength. Shading artefacts can easily be seen.

A built in transmit coil (also known as a body coil on lower field systems) cannot be used with these “new” systems because interaction between high frequency transmit pulses and the human body prevents generation of a homogeneous B_1 excitation field. Instead, a local transmit and receive coil for the body part under investigation is typically used; only for imaging of body parts that are small compared to to the wavelength of the electric field, is it sometimes possible to implement, alternatively, a “simple” hardware solution, e.g. for digital imaging. Unfortunately this is seldom the case. In particular with neurological and cardiological imaging, dielectric effects cannot be adequately compensated for and new solutions are needed.

It was thus the aim of this thesis to develop novel transmitter designs for magnetic field imaging that could be used at 7.0 Tesla field strength.

1

1.3. THEORY OF MAGNETIC RESONANCE IMAGING

1.3.1. NUCLEAR SPIN AND MAGNETIC MOMENT

A magnetic resonance imaging (MRI) experiment is performed by placing an object inside a superconducting magnet, which produces a static magnetic field B_0. In this case all nuclei with a non-zero nuclear magnetic moment or nuclear spin $\vec{I}$ can be detected using MRI (the ^1H nucleus is of particular interest for reasons which are explained below). It has been shown that there is a linear relationship between the nuclear magnetic moment $\vec{\mu}$ and angular momentum $\vec{P}$

$$\vec{\mu} = \gamma \vec{P}. \tag{1.1}$$

Here γ is the proportionality constant (also known as the gyromagnetic ratio) of a nucleus.

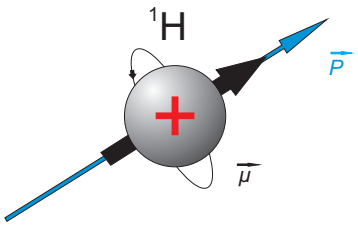


Figure 1.2: Magnetic moment of a hydrogen core.

In the classical model, rotation of a charged particle, described by its angular momentum $\vec{P}$, induces a magnetic dipole field. The direction and magnitude of this field are described by the magnetic moment $\vec{\mu}$, see figure 1.2. The vector $\vec{\mu}$ is collinear with the angular momentum $\vec{P}$ of the sphere. If a cylindrical permanent magnet is brought into an external magnetic field in order to minimize its potential energy, it experiences a mechanical torque bringing the magnet into alignment with the external field. If the magnet is rotating around its longitudinal axis it will possess angular momentum. Due to the conservation momentum the magnet cannot align parallel to the external field. Consequently, the magnet experiences a torque perpendicular both to the external field and the angular momentum, which results in rotation (precession) of the magnet. The frequency of this precession is called the Lamor frequency and corresponds to its resonance frequency $\omega_0 = \gamma B_0$.

When an external field is applied to e.g. a hydrogen-^1H nucleus, its spectral lines are split. This is also known as the Zeeman Effect. This splitting is attributed to ^1Hinteraction between the magnetic field and the magnetic dipole moment associated with the orbital angular momentum. When considering an isolated magnetic moment within a static magnetic field, one will find that transitions between the different energy levels are prohibited due to the law of energy conservation. Transitions can exclusively be induced by an additional time-dependent electromagnetic radio frequency (RF) field that interacts with the magnetic moment, the effect is known as magnetic resonance (MR).

In MRI, transitions are induced by an electromagnetic radio-frequency (RF) field $B_1(t)$ with the angular frequency ω_{RF}, which is irradiated perpendicular to the direction of the static magnetic field B_0 . Such a time-dependent magnetic field, however, can only induce transitions fulfilling the selection rule $\Delta m = \pm 1$, i.e., transitions between neighboring energy levels. As a consequence, the energy $E_{RF} = \hbar\omega_{RF}$ of a photon of the RF field must be identical with the energy difference $\Delta E = \hbar\omega_0 = \gamma\hbar B_0$ between two neighboured energy levels, which yields the resonance condition

$$\omega_{RF} = \omega_0 = \gamma B_0.$$

Due to thermal motion the magnetic moments of nuclei in a macroscopic object cancel out each other, no net magnetization is detectable. However, if this object is taken into an external magnetic field B_0 only $2I+1$ (spin levels) discrete orientations of the magnetic moments are allowed. If the object is in thermal equilibrium the spin levels are described by Boltzmann statistics:

- the lower the energy $E_m = -\gamma\hbar B_0 m$ of a state, the greater the occupation number.

The macroscopic magnetization is described by the magnetization vector M_0 which is defined as the vector sum of the nuclear magnetic moments per unit volume V. It can be calculated as

$$M_0 = |M_0| = \frac{1}{V}\sum_{i=1}^{N}(\mu_z)_i = \frac{N}{V}\cdot\frac{I(I+1)\gamma^2\hbar^2 B_0}{3k_b T},$$

where k_b is the Boltzmann's constant and $\hbar$ is the Planck's constant. This equation also explains why the enhancement of magnetic resonance imaging (MRI) is only possible by altering B_0 as T is given by the human body and γ is determined from the nucleus under investigation.

nuclei	net Spin	γ (MHz/T)
^{1}H	1/2	42.58
^{2}H	1	6.54
^{31}P	1/2	17.25
^{23}Na	3/2	11.27
^{14}N	1	3.08
^{13}C	1/2	10.71
^{19}F	1/2	40.08

Table 1.1: Nuclei, net spin and the gyromagnetic ratio for relevant nuclei in magentic resonance imaging.

The most interesting magnetic isotope for MR-imaging is the ^{1}H isotope: hydrogen is present in abundance in biologic tissue (and the water therein); the ^{1}H nucleus has a large gyromagnetic ratio; and, ^{1}H has 99.98 percent natural isotopic abundance. A table of MR-relevant properties of nuclei is given in the table 1.1.

Nuclei other than ^{1}H are often referred to as X-core nuclei. As the gyromagnetic ratio is different for those nuclei than from ^{1}H they require suitable transmit and receive hardware with a working frequency different from the one of ^{1}H. These other nuclei are often interesting for spectroscopy and functional studies as kidney function or muscle properties. These x-core nuclei profit highly from higher B_0 field strength and will be more important in the future due to improvements in hardware design.

1.3.2. NUCLEUS IN A MAGNETIC FIELD

The phenomenon of nuclear magnetic resonance (NMR), on which MRI is based, was independently discovered by Bloch [2] and Purcell [27]. In the absence of an external magnetic field, the orientation of a proton's spins is random as shown in figure 1.3:

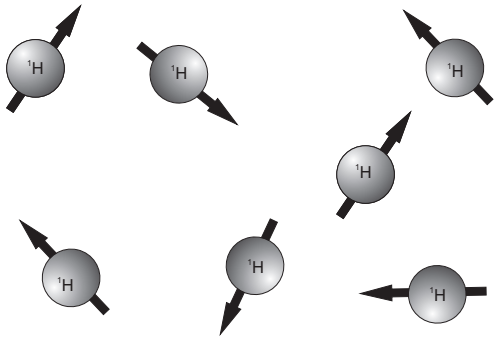


Figure 1.3: Proton spins in the absence of an outer magnetic field.

In the presence of an external magnetic field like in figure 1.4, a spinning, charged particle will behave like a small magnet and will align either parallel or anti-parallel to the direction of the B_0-field. The energies of these two spin states are similar and consequently they are similarly populated (according to a Boltzmann distribution). The parallel state has slightly lower energy: from one million protons, approx. one more is aligned parallel than anti-parallel at 1.5 Tesla.

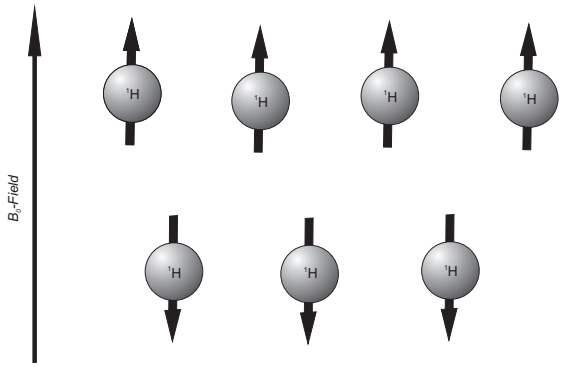


Figure 1.4: Proton spins in the presence of an outer magnetic field. There is an alignment of the spin either parallel or anti parallel to the B_0 field.

1

When aligned to an external static magnetic field, a proton will begin to precess around the direction of the static magnetic field with a frequency that is proportional to the strength of the static magnetic field, see figure 1.5. This precession can be seen as being analogous to precession of a "heavy" spinning top in the presence of gravity.

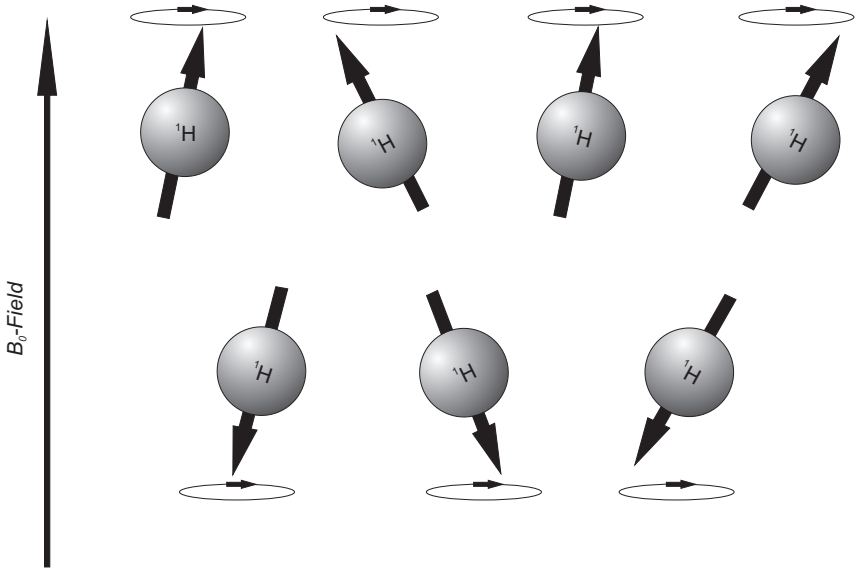


Figure 1.5: Proton spins in the presence of an outer magnetic field precessing out of phase.

In figure 1.6 a volume V containing protons is brought into an external magnetic field B_0. The proton spins form a spin system with a net magnetization represented by the vector M_0. While the nuclear magnetic moment μ can take only discrete values and angles to the B_0 vector, the magnetization vector M_0 can take any value from 0 – 180 degrees with 0 degrees representing collinear alignment and 180 degrees the anti-parallel state. A radio frequency (RF) field is then applied perpendicular to B_0 causing the protons to precess coherently, thus making it possible to detect the sum of all protons precessing as an induced voltage in a tuned resonator.

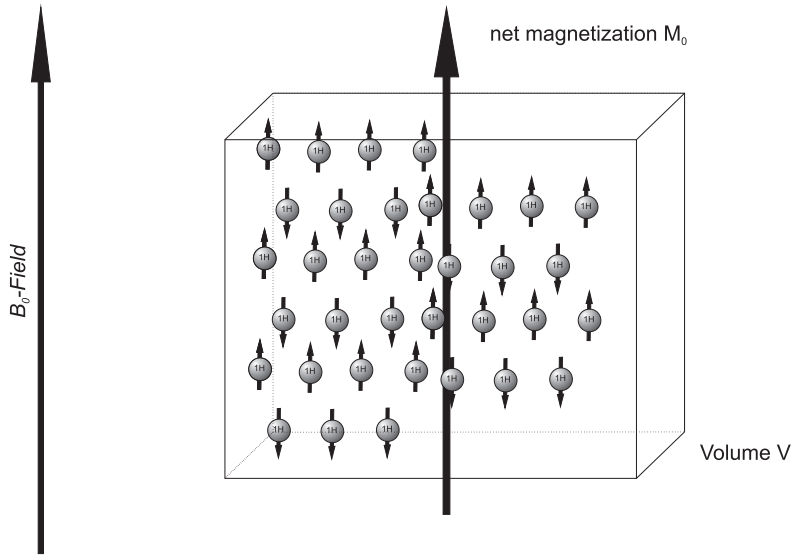


Figure 1.6: Proton spins in the presence of an outer magnetic field forming a spin system in the volume V with a net magnetization M_0.

To facilitate understanding, it is possible to change to a frame that rotates with the angular frequency ω around the z-axis of the laboratory frame. In this frame, the magnetization M is split-up into the two components M_z and M_{xy}.
If an RF field is then applied during the time t_p the magnetization is rotated by the flip angle

$$\alpha = \omega_1 t_p = \gamma B_1 t_p.$$

It is therefore possible to tilt the spin system out of equilibrium with RF power. Angles of from $0-180$ are allowed for this operation, thus allowing more or less excitation of the spin system. If the duration t_p of the RF field is chosen to rotate the magnetization in the rotating frame by 90 degrees, then this pulse is denoted as a 90 degree or $\pi/2$ pulse. Accordingly, the magnetization M is rotated by 180 degrees when the duration of the RF pulse is doubled at the same flux density B_1. This pulse, which inverts the magnetization from the positive to the negative z-direction, is called a 180 degree or π pulse.

To get spatial information, magnetic field gradients are applied in all three dimensions, see figure 1.7. Due to these gradient fields the precession frequencies of the protons can be related to points in space and the phase and frequency of the precessing magnetization can be measured by an RF resonator.

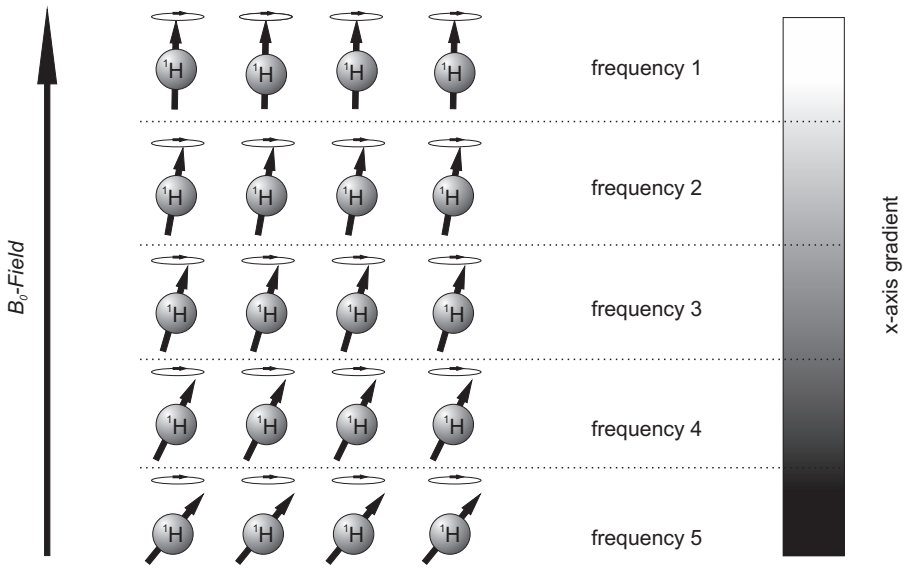


Figure 1.7: Frequency difference due to the presence of magnetic gradient field that is acting on the precessing proton spins in order to get spatial resolution. The frequency differs from slice to slice because of a slightly different B_0 value due to the gradient.

The induced signal in the resonator is then digitized and processed with an inverse two-dimensional Fourier transform to convert the signal into the spatial domain that will produce the picture.

For an in-depth introduction to magnetic resonance imaging the reader is referred to textbooks like [12].

1.4. CONVENTIONAL RF COIL DESIGN

CONVENTIONAL radio frequency (RF) coil design started in the 1950s when Gersch and Loesch [10] conducted their experiments on nuclear magnetic resonance (NMR) samples in an oscillating magnetic field. The main difference between an RF coil and an antenna is that an antenna is built to be a perfect radiator. This means that as much as possible of the amount of power applied to the antenna's terminals shall be radiated away from the antenna into free space into the far field region of the antenna. An RF coil on the other hand, tries to establish an oscillating magnetic field to excite the spin system. Here, the goal is to maximize the strength of the magnetic field in a very close vicinity to the coil that is usually within or less than a wavelength of the applied radio frequency. While on a transmit antenna, for example for a terrestrial music station in the very high frequency band (VHF), the applied oscillating current at the terminals helps to radiate the wave away by producing alternating magnetic (H) and electric (E) waves that are perpendicular to each other; on a RF coil this effect is usually unwanted. Radiated power in an MRI coil is a loss mechanism and thus decreases efficiency. The E-field is a rather annoying companion of the H-Field for the RF coil designer, as the E-field is to be blamed for dielectric interactions with human tissue that causes unwanted heating. This is why the amount of radio frequency radiation that is transmitted into the human body during an MRI exam is limited and needs to be monitored. Moreover, international guidelines exist that set-outlimits for the maximum amount of power that shall be applied to a human body. These values are usually referred to as the specific-absorption-rate (SAR).

In a simple embodiment, a radio frequency coil can be formed from a capacitor and an inductor as in figure 1.8. The capacitor stores electrical energy of an E-field, while the conductor L stores energy in the form of an H-field in its vicinity. While the mechanisms by which these devices operate are interesting, a discussion hereover is beyond the scope of this introduction – the interested reader is referred to the literature; see, for example [11] – it is further interesting to note that the storage capacity of the capacitor depends not only on its physical dimensions but also on the dielectric material used between its plates. The operating angular frequency ω of such a simple antenna (in MRI it is also referred to as a loop coil) is given by equation 1.2

$$\omega = \frac{1}{\sqrt{LC}} \tag{1.2}$$

where L is the inductance in Henry and C the capacitance in Farad. The angular

frequency ω can easily be converted into the unit for oscillations per second – Hertz – by division by 2π.

In order to use such a coil for NMR or MRI, it would have to be coupled to the transmitter and receiver by appropriate means, so that the impedance at the loop terminals would be matched to the system impedance; this is in order to allow maximum power transfer. This procedure is usually referred to as matching and can be realized either inductively or capacitively. The process of impedance matching is well described in the literature [26]. Furthermore, the angular frequency ω must be match with the resonance frequency of the NMR or MRI system ω_{system}, as given by equation 1.3

$$\omega_{system} = \gamma B_0 \tag{1.3}$$

where γ is the gyromagnetic ratio and B_0 the main magnetic field strength, for example 3.0 Tesla. Here γ is a physical constant that is dependent on the nucleus under investigation. The value for γ of the ^{1}H nuclei, for example, is 267.513×10^6 rad $s^{-1} T^{-1}$. It can thus be easily shown that the resonance frequency ω_{system} of a 3.0 Tesla MRI system must be 802.539×10^6 rad s^{-1} which equals ~128 MHz.

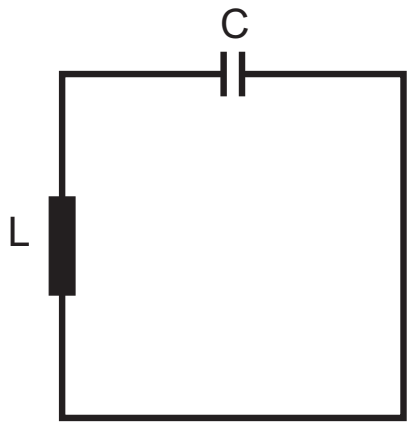


Figure 1.8: Most simple form of a radio frequency circuit (in MRI also called coil) consisting of an inductor L and a capacitor C. The capacitor C can store electric energy and the inductor L can store magnetic energy. The circuit can resonate at a resonance frequency ω that depends on the values of the inductor and capacitor.

TRANSMIT CASE

The RF-resonator, also often referred to as the coil, acts as an antenna in the near-field that converts the cable-bound electric energy to a free-air electromagnetic near-field wave. It is most desirable that all power coming from the amplifier is transferred into free space to avoid losses. Therefore, parts of the spectrometer should be connected with little to no losses. This is achieved by using 50 Ohm coaxial cables, and by adjusting the load to 50 Ohms by matching and tuning of the coil. The coil behaves then as a pure resistive load during transmission. As can be shown easily, the maximum power from a source with impedance Z_0 is transferred to a load when Z_l is the complex conjugate to the impedance of the source $Z_0 = Z_l^*$.

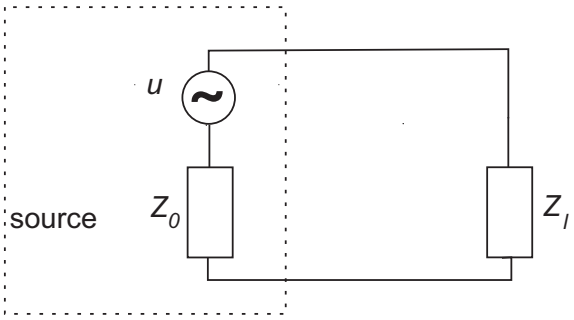


Figure 1.9: Equivalent electrical circuit of source and load in a MRI system.

It can be shown that the dissipated Power P_{loss} is

$$P_{rad} = \frac{U_0^2 Re\{Z_l\}}{|Z_0 + Z_l|^2},$$

with $U_0 = \frac{U}{\sqrt{2}}$.

It is obvious that the maximum power is transferred when the right-hand side of the equation is maximum. This is the case when

$$Re\{Z_0\} = Re\{Z_l\}$$

and

$$Im\{Z_0\} = -Im\{Z_l\}$$

The total power delivered then is

$$P = Re\{UI^*\} = \frac{U_0^2}{4Re\{Z_0\}}.$$

This also explains why all components of a RF system should have the same impedance and should be connected via lines with the same impedance. It also explains why, at best, only 50 percent of the available power can be transmitted from the source into free air.

The equations above further explains why an antenna designer must, at the same time as designing an antenna, also design a matching network if the impedance of the antenna and the line are not equal (as is usually the case). The matching network transforms the impedance and makes it possible that the source sees a perfect match on the end of the line, instead of a mismatched antenna. The same is true for the antenna; also here the matching network makes the line look like a perfect match for the antenna's own impedance. Thus, a maximum of power transfer can be achieved even though the source, line, and the antenna do not have the same impedance.

RECEIVE CASE

The receiver chain consists of an NMR-probe and a pre-amplifier: shown schematically in figure 1.10.

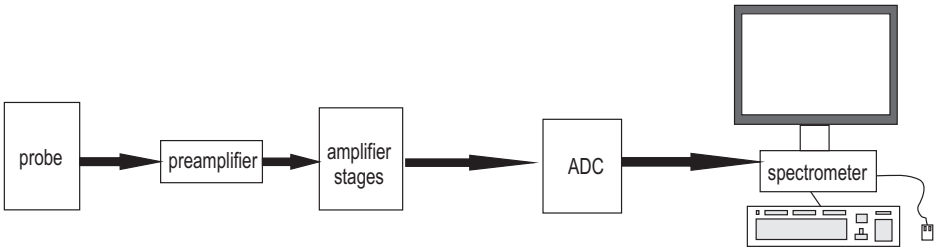


Figure 1.10: Amplifier stages. The weakly induced MRI-signal within the coil needs to be amplified to a level where digitization can take place.

Relaxation of spins in the tissue causes a current to be induced in the RF-resonator that is then amplified by the pre-amplifier. The signal is then fed through further amplification stages and after several steps of amplification, is digitized and fed into the spectroscope computer.

frequency [MHz]	free space wave length [cm]	cable velocity	fraction of wavelength λ	wavelength in cable [cm]	phase [deg]
64	469	0,666	1	313	360
			1/2	156	180
			1/4	78	90
			1/8	39	45
123	244	0,666	1	162	360
			1/2	81	180
			1/4	41	90
			1/8	20	45
298	101	0,666	1	67	360
			1/2	34	180
			1/4	17	90
			1/8	8	45

Table 1.2: Frequency, wavelength in free space and in a cable as well as the phase for frequencies relevant for magnetic resonance imaging.

1.5. IMPLICATIONS OF UHF MRI ON RF COIL DESIGN

WHILE the aforementioned considerations hinder the triumphal march of 7.0 Tesla MRI systems into clinical routine, the new ultra-high field (UHF) MRI systems ($> 7.0T$) also bring possible advantages besides their inherent high signal to noise ratio. These new high field systems run at 7.0 Tesla B_0 field strength, which gives, according to 1.3, a system B1 frequency of around 300 MHz. In this frequency regime, new solutions to RF problems become available that were not practicable at the rather low frequencies used in 1.5 and 3.0 T systems. At higher frequencies, the wavelength decreases as shown as in the table below. At shorter wavelength, micro-strip technology can be used; for example, at 300 MHz, a branch line coupler becomes a reasonable size. The 300 MHz RF devices can be shrunk even further if a substrate with a high permittivity is used. This allows for new designs and the transfer of solutions known from traditional microwave RF engineering. The origin of these advantages become clear when MRI systems of different field strengths and their associated transmit frequencies are compared. As further illustration, the wavelengths for a 1.5 Tesla (frequency 64 MHz), 3.0 Tesla (frequency 128 MHz) and a 7.0 Tesla MRI system are given in the table 1.2:

In RF circuit design, the wavelength of the system needs to be taken into consideration. Due to the large wavelength of several meters both in 1.5 and 3.0 Tesla MRI, certain elements need to be built from equivalent lumped circuit elements. For example, a 90-degree phase shift at 64 MHz would require a cable that is 78 cm long. It is not very

practical to integrate such a long cable into a circuit. Such long cables pose a threat for the patient and can cause spurious RF behaviour if not shielded properly. Thus, at 1.5 or 3.0 Tesla, when, for example, a $\lambda/4$ transmission line section is needed in a RF circuit, an equivalent lumped element circuit is used instead. This design process is schematically given in figure 1.11.

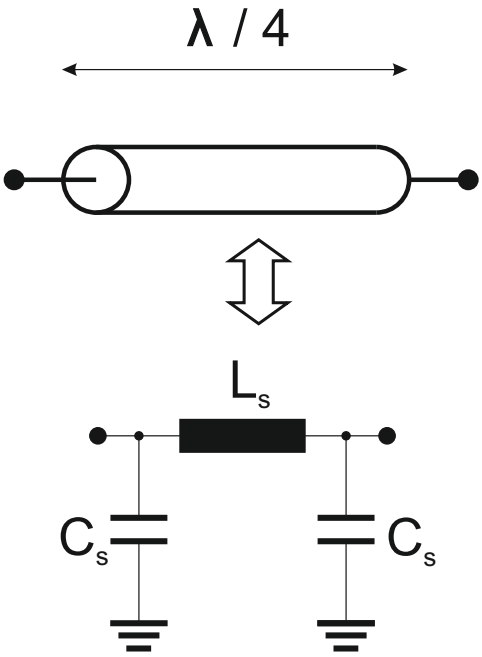


Figure 1.11: Transformation of a $\lambda/4$ transmission line into an equivalent lumped element circuit.

Designing and building such equivalent networks can be cumbersome. While in most cases there are formulas to calculate the relevant values,practical implementation is usually not straightforward (due to unavoidable random tolerances of real world elements and parasitic effects) and manual "tweaking" is often required.

At 7.0 Tesla and above, on the other hand, the working frequency becomes so high, that it is possible to use micro-strip-line technology and place the circuit parts inside the bore of the MRI. These circuits can be further reduced in size if a high permittivity carrier substrate is selected.

1.6. DIELECTRIC RESONATOR ANTENNAS

IN order to understand the concept of dielectric resonator antennas (DRAs), it is important to first know what a dielectric material is. A short answer to the question "What is a dielectric material?" would be:

"A dielectric material is an electrical insulator that can be polarized by an applied electric field."

However, a deeper understanding of the properties of matter are desirable, especially when matter is interacting with an electric field. A short introduction is thus given hereafter. For an in-depth analysis the reader is referred to classical textbooks on electrostatics such as [11, 17].

1.6.1. DIELECTRIC MATERIALS - INSULATORS AND CONDUCTORS

Matter can be subdivided into two classes: conductors and insulators (dielectrics). Conductors consist of an "unlimited" stock of charge carriers that are able to move within the conductor. For example, in metals, one or two electrons of one atom are not bound, but can move freely within the material. In dielectrics, all charge carriers are bound to atoms or molecules. They have only limited mobility in close proximity to the atom or molecule. Since those movements are very small when compared with a conductor, the effect of an external electric field on a dielectric is fundamentally different to its effect on a metal. When a metal gets exposed to an external electric field, the free charge carriers inside the metal will form a shield at the boundary of the metal that is equal in magnitude to the external applied electric field. Due to this effect, an electromagnetic wave can penetrate into a metal only for a very short distance, known as skin depth δ_s. The skin depth depends on the frequency of the incident electromagnetic wave as well as on the conductivity of the metal. We can calculate the skin depth δ_s according to [17] as

$$\delta_s = \sqrt{\frac{2}{\mu\sigma\omega}} \tag{1.4}$$

where $\omega = 2\pi f$ is the frequency in radians per second, μ the permeability in Henry per meter and σ the conductivity of the metal in Siemens per meter. The skin depth is also the reason why in MRI we can use very thin layers of copper as a coil conductor.

1.6.2. DIELECTRICS IN AN EXTERNAL ELECTRIC FIELD

When a quasi-neutral atom is moved into an electric field, it is influenced by the external field as follows: the positively charged core of the atom is displaced in the direction of the external field;the electron cloud of the atom, which is negatively charged, is displaced in the opposing direction. If the external field is strong enough, the atom can be ripped apart; a process that is called ionization. If ionization occurs, the matter becomes a conductor. If the force of the external field and the forces between the core and the electron cloud are weaker, an equilibrium is established, leading to a polarized atom having a small dipole moment p that has the same direction as the external field E. This induced dipole moment p is proportional to the external field E and can be described by

$$p = \alpha E \tag{1.5}$$

where α is a measure of how "polarizeable" an atom is. As α is about $2\pi\epsilon_0 r\text{^}3$, where r is the atom radius, we can conclude that except for the factor ϵ_0 the polarization depends on the volume of the atom.

In molecules the situation is a bit more complex as some molecules can be more or less polarized depending on the orientation of the molecule with respect to the applied external electric field. This is for example the case for carbon dioxide.

If a polar molecule such as hydrogen dioxide (water) is put into an external field, a torque is experienced by the molecule. If the molecule can rotate freely it will rotate until it is aligned with the external electric field. If the external field is removed random movement due to temperature of the material will lead to a depolarization and thus back to a net zero field. Both effects lead to polarization that can be quantified as the dipole moment per unit volume.

For many dielectric materials the amount of polarization P is proportional to the applied external electric field. It can be expressed as

$$P = \epsilon_0 \chi_e E \tag{1.6}$$

wherein χ_e is the electrical susceptibility of a dielectric and ϵ_0 is a term factored out of χ_e. It thus follows that the displacement current D in a linear media is

$$D = \epsilon_0 E + P = \epsilon_0 E + \epsilon_0 \chi_e E \tag{1.7}$$

and thus D is also proportional to E:

$$D = \epsilon E \tag{1.8}$$

with

$$\epsilon = \epsilon_0(1 + \chi_e). \tag{1.9}$$

ϵ is constant known as the dielectric constant or permittivity of a material. In vacuum the susceptibility is zero and thus the dielectric constant is ϵ_0. This is also known as the dielectric constant of a vacuum and has a value of $\epsilon_0 = 8.854 \times 10^{-12}$F/m. One can remove the factor ϵ_0 to obtain a dimensionless number:

$$\epsilon_r = 1 + \chi_e = \frac{\epsilon}{\epsilon_0} \tag{1.10}$$

this is known as the relative dielectric constant of a material.

1

1.6.3. THE LEYDEN JAR

An alternative way to describe the permittivity is to look into historic experiments. Especially the Leyden jar that was invented in the town of Leiden is very suitable for this purpose. In 1745 Pieter van Musschenbroeck [40] in Leiden and Ewald Georg von Kleist discovered independently that charges from an electrostatic generator could be gathered and stored in jar-like devices similar to the one shown in Figure 1.12.

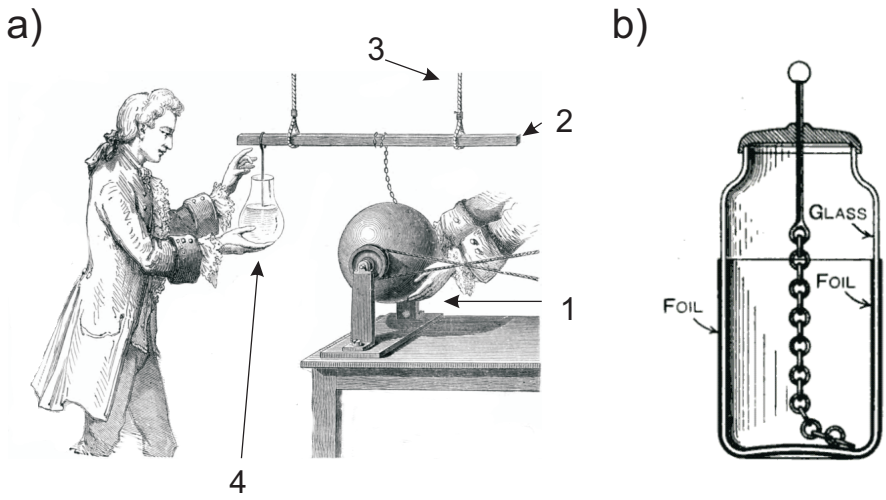


Figure 1.12: a) shows the use of a Leyden jar (4) that is used to store electrostatic energy produced by the electrostatic generator (1). Both devices are connected to each other over conductive elements like the iron bar (2) that is isolated to earth by suspension with ropes (3). b) shows a detailed view of a Leyden jar as they were commonly used until the beginning of the 20th century consisting of a jar that has a metal foil on the inside and outside. The charge is passed through a non-conductive top via a metal rod. The charge is conducted to the inner foil via the central metal chain.

For the first time in history it became possible to store electric charge and accumulate charge of a significant amount. Before the invention of this device only limited amounts of charge could be generated and stored for experiments. The Leyden jar paved the way for the experiments of Galvani, Volta, and Franklin and was widely used in the electromagnetic research community until the 20th century.

The Leyden jar acts as a basic capacitor, wherein the glass of the jar acts as a dielectric. The similarities between the Leyden jar and the parallel plate capacitor are obvious and the working principle is the same. The parallel capacitor is explained in detail in the next section.

1.6.4. THE PARALLEL PLATE CAPACITOR

The Leyden jar basically works in the same way as a parallel plate capacitor as shown in figure 1.13.

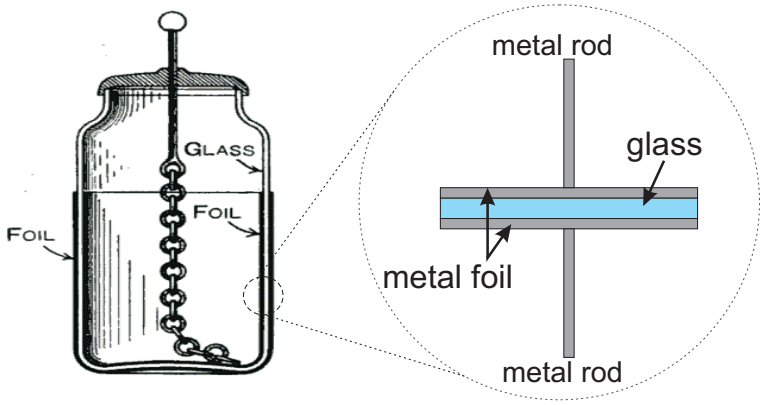


Figure 1.13: From the Leyden jar to the parallel plate capacitor. If one looks closely at a section of the Leyden jar we see a resemblance to a parallel plate capacitor: The inner and outer foil are the metal plates of the capacitor. The glass of the jar acts as a dielectric. The two metal rods are realized by the inner connector inside the jar that is conductively coupled to the charge generator. The second rod of the parallel plate capacitor is a ground connection in case of the Leyden jar usually via the experimentalist or environment.

A Leyden jar can be represented by the following model: two metallic plates with a surface area A are separated by a distance D from each other as in figure 1.14. The space in between those plates is filled with a non-conductive material such as air or vacuum. The capacitance C_0 can be determined with the equation:

$$C_0 = \frac{\epsilon_0 A}{D} \tag{1.11}$$

where ϵ_0 is the permittivity of free space, A the surface area of the plates and D the distance between the plates.

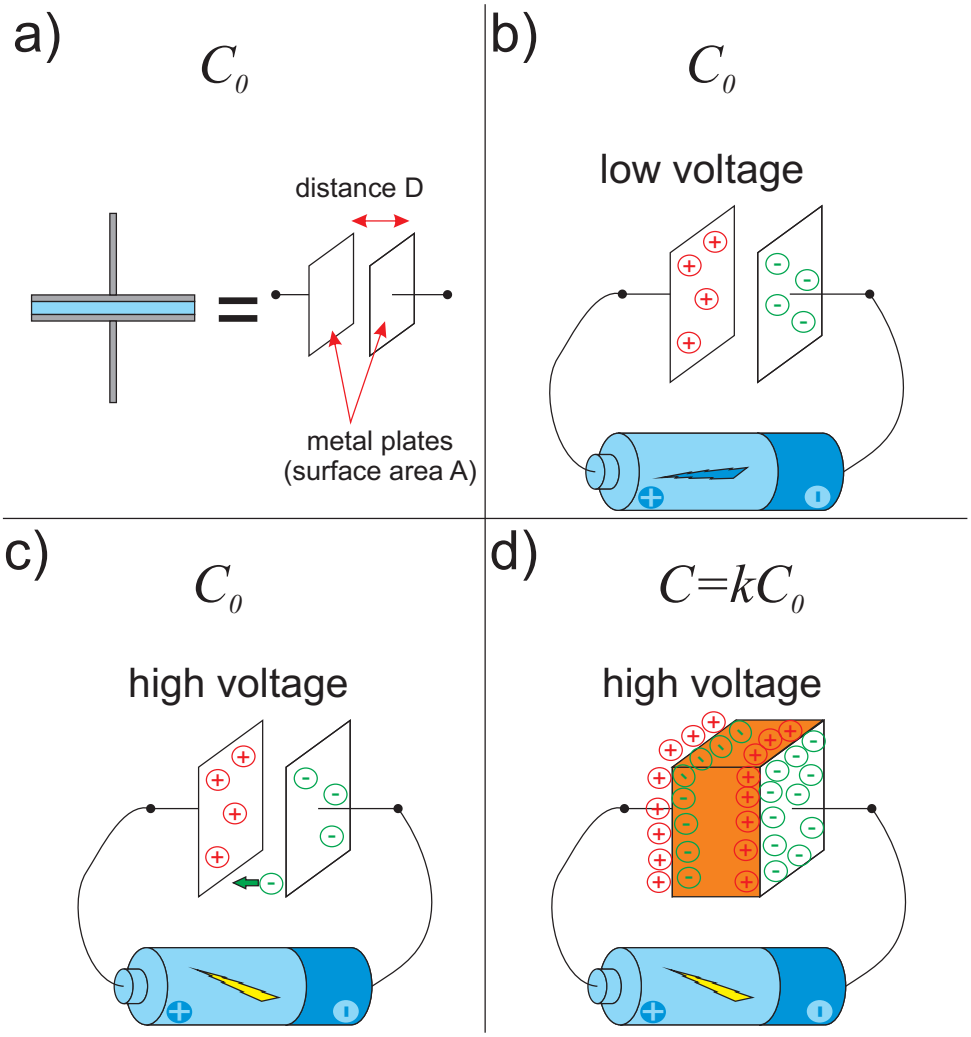


Figure 1.14: In a) we can see that the Leyden jar unit capacitor can be translated into a parallel plate capacitor with two metal plates with the surface area A that are separated by a distance D. In b) the space between the metal plates is filled by vacuum with a dielectric constant of ϵ_0 and the capacitance is C_0. When a low voltage is applied charge of opposite polarity will accumulate on the plates and create and electric field between the plates. In c) the voltage is increased to a high voltage. The high voltage allows an electron to leave its plate. If this occurs in air the air will become ionized and a spark can be observed. The capacitance is still C_0 however in the case when sparking happens the capacitor actually becomes a short and thus $C_0 = 0$ In d) the same high voltage as in c) is applied however the free space between the plates of the capacitor is now filled with a dielectric. The dielectric is polarized thus the capacitance is increased by a factor k. The new capacitance is then $C = kC_0$

If a voltage is applied to such a capacitor from a voltage source, such as a battery, the plates will become charged. One plate will become positively charged, while the other

plate accumulates the negative charges. This separation of charge causes an electric field to be generated between the plates. If the applied voltage is high enough, the air between the plates can become ionized; charge equalization via a spark can result. From a practical point of view, it is desired to prevent sparking. This is achieved by placing an insulator between the plates. The advantages are twofold: 1) the capacitor can be charged with/to a higher voltage and 2) the capacitance is now increased from C_0 to C by a factor of k e.g. more energy can be stored by the capacitor. The applied electric field leads to small displacements of atoms, ions and/or changes in orientation thereof leading to "polarization". The extent to which a material can be polarized is expressed by its permittivity or the dielectric constant. The capacitance C is then determined by:

$$C = C_0 k = \frac{k\epsilon_0 A}{D} \tag{1.12}$$

where k is a proportional factor depending on the insulating material. If we define $k\epsilon_0$ to be the permittivity of the insulator and name it ϵ we can now define the capacitance C as:

$$C = \frac{\epsilon A}{D}. \tag{1.13}$$

We have now defined the permittivity of the insulator to be ϵ, we may also equally refer to it as the dielectric constant of the insulator. It is custom to represent the dielectric constant relative to the dielectric constant of vacuum:

$$\epsilon_r = \frac{\epsilon}{\epsilon_0} \tag{1.14}$$

where ϵ_r is now the relative dielectric constant of a material, ϵ is the dielectric constant of the material and ϵ_0, the permittivity of vacuum ($\epsilon_0 = 8.854 \times 10^{-12}$F/m). It should be noted that the term dielectric constant is in fact not correct as it implies a true natural constant like Boltzmann's or Planck's constant. However, the dielectric constant is dependent on the frequency and on the temperature. It is thus preferable to use the term permittivity. While this behavior is very interesting it is of little practical importance in the frequency and temperature regimes of current human MRI. The interested reader is thus referred to textbooks on solid-state physics that cover this topic in detail such as [34] or [14].

Dielectric materials interact with electromagnetic waves. If a electromagnetic wave travelling in free space for example enters a material with a high permittivity the wave-

length decreases by a factor of $\sqrt{\epsilon_r}$. If the wave moves from one material into a second material with a different permittivity, a part of the wave will be reflected, and a part transmitted. For a more detailed description of this phenomena, see textbooks in electrical engineering or electrodynamics for example [17, 26].

Typical values of ϵ_r range from 1 to 10 for polymers, from 10 to 100 for polar solvents (with water around 80) and from 100s to thousands for inorganic compounds like perovskites. A perovskite is a material with the type of ABX_3 structure such as calcium titanate oxide [39]. One well-known perovskites is barium titanate - a dielectric ceramic. Its dielectric constant can be as high as 7000. The structure of barium titanate is given in figure 1.15.

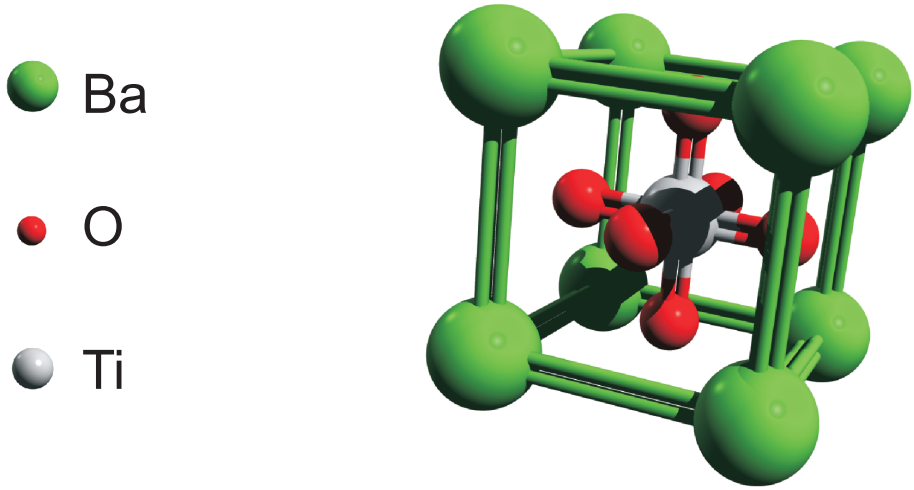


Figure 1.15: Illustration of the perovskite ABX_3 structure on the example of $BaTiO_3$.

Dielectric materials with a high permittivity, low loss and temperature stability are important for the global communications industry; they are commonly used in wireless technology for example in wireless communications base stations. For an introduction to this matter see [41]. High permittivity materials are also interesting candidates for RF coil design because they make efficient electromagnetic field storage devices and their incorporation into a conventional RF coil can significantly change the distribution of magnetic and electric fields within a sample.

1.6.5. HISTORY OF DIELECTRIC RESONATORS

DIELECTRIC resonators (DRAs) were first theorized in 1939 by Richtmyer [33]. Based on the discovery that a cylinder of dielectric material can serve as a guide for electromagnetic waves of certain frequencies he concluded that if such a cylinder would be bent and the ends joint together as in 1.16 such an object would act as an electrical resonator.

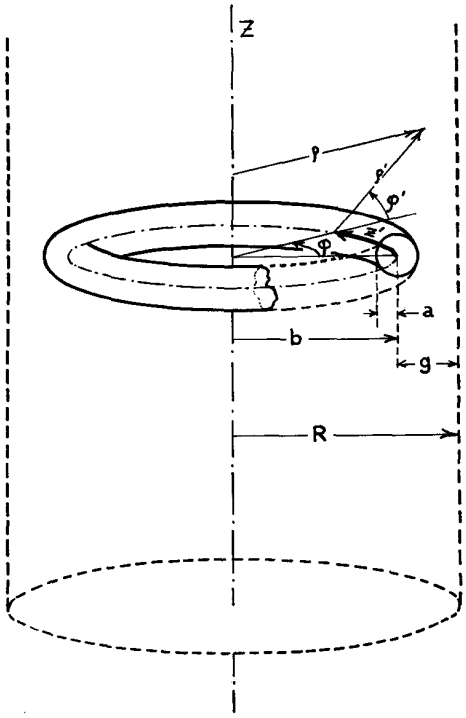


FIG. 2. Dielectric ring resonator, and various quantities used in the analysis: true cylindrical coordinates ρ, z, ϕ; pseudo-cylindrical coordinates ρ', z', ϕ'; and dimensions.

Figure 1.16: Illustration of the dielectric ring resonator suggested in the publication of Richtmyer in 1939 [33].

The description of dielectric resonator modes by Okaya and Barash [24] in the 1960s as well as the development of low loss ceramic materials in the same decade allowed for the first application as high-Q elements for circuit applications such as in filter and oscillator design. Sager and Tisi [35] were the first to mention the possibility to construct very small antennas using dielectric resonators. A more detailed overview of the development of dielectric resonators is given by Petosa in [25].

1.6.6. INTRINSIC FEATURES OF DIELECTRIC RESONATORS

Dielectric resonators offer attractive features:

- very high quality factor if used in shielded applications such as filters and oscillators with $Q_{unloaded} = \frac{1}{tan\delta}$
- effective radiators when in an unshielded environment
- dimensions in the order of $\lambda_0/\sqrt{\epsilon_r}$ where λ_0 is the free-space wavelength and ϵ_r is the dielectric constant of the resonator
- no inherent losses in conductors
- various coupling schemes exist
- various modes exist for a given geometry each with a unique internal and associated external field
- simple design formulas that can be solved using spread sheet software to design for certain dimensions or permittivity

These features make dielectric resonators an interesting candidate for MRI coil technology. DRAs are especially interesting for application at 7.0 Tesla and higher field strengths. At high field strengths, DRAs have dimensions that are more suitable compared to when applying them at lower field strengths. The effect of the B_0 field strength on the dimension of λ_0 is explained by some examples in the following table where the shortened λ_s is calculated depending on different field strength and materials:

frequency [MHz]	λ [cm]	ϵ_r	$\sqrt{\epsilon_r}$	λ_m [cm]	material
64 (1.5T)	469	80	$4\sqrt{5}$	52	water
		1000	$10\sqrt{10}$	15	perovskite
123 (3.0T)	244	80	$4\sqrt{5}$	27	water
		1000	$10\sqrt{10}$	8	perovskite
298 (7.0T)	101	80	$4\sqrt{5}$	11	water
		1000	$10\sqrt{10}$	3	perovskite

The table above shows very clearly why it is not only desirable to use materials with high permittivity for DRAs but also why it is interesting to work at a relatively high field strength.

1.6.7. MODES IN DIELECTRIC RESONATORS AND THEIR NOMENCLATURE

Dielectric resonators support stable, time-invariant electromagnetic field patterns within the resonator which are usually referred to as modes. Modes in dielectric resonators can be classified into three classes:

- Transverse electric **TE** mode
- Transverse magnetic **TM** mode
- Hybrid electromagnetic **HEM** modes

Modes are defined by the field vector that is normal to the propagation: in a TE mode resonator the electric field vector is normal to the propagation, and in a TM mode resonator the magnetic field vector is normal to the direction of propagation.

Different modes are identified by three subscripts for example a TM_{mnp} mode where m, n and p denote the number of the half-wavelength field variations in the azimuthal (ϕ), radial (ρ), and height directions, respectively. An example for the TE and TM mode is given in figure 1.17. The subscript δ is used to indicate when there is less than half-a-wavelength variation in the height direction.

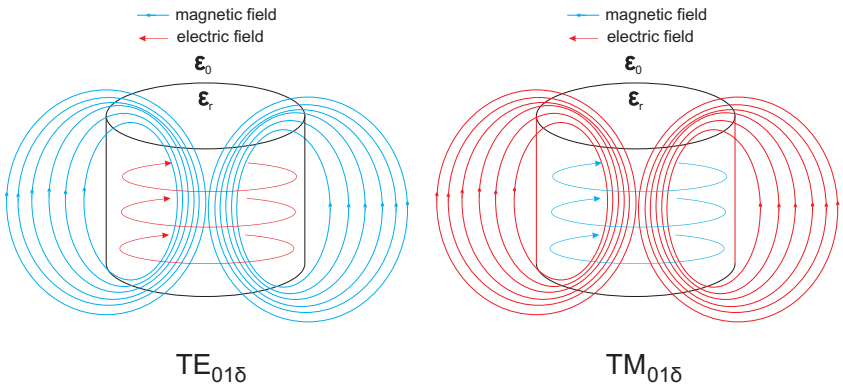


Figure 1.17: Illustration of the TE01δ and the TM01δ mode of a cylindric dielectric resonator.

1

1.6.8. DIELECTRIC RESONATOR DESIGN

Cylindrical dielectric resonators are designed by selecting their dielectric constant ϵ_r and dimension. They can take any desired shape; in practice however, rectangular or cylinder structures are usually used as the mode distributions and the resulting magnetic and electric fields are well known for these structures. These elements are usually machined into puck-like structures that can be either shielded by a metal cavity to maintain high-Q or, if the shield is removed, can become efficient antennas. Dielectric resonators are extensively used in high efficiency oscillators [18] for example. One of the obstacles in using dielectric resonators is the exact design procedure.

To estimate the correct frequency and thus mode three options are currently known:

- design based on electromagnetic simulations
- design based on empirical derived formulas
- design based on empirical experiments

Most high permittivity materials are hard and brittle. Processes for their manufacture are delicate and usually involve multiple steps. As a final step they are often sintered at high pressure and high temperature, which causes the final parts to shrink. This shrinking is not omnidirectional and thus an iterative design process might thus be needed.

A better approach, if geometrically possible, is to sinter a large block, determine the exact permittivity of the sintered block and then machine the block to dimensions that have previously been calculated. Either approach requires good knowledge of the intended final design such as the desired modal pattern, the electromagnetic field distribution for proper probe coupling, geometry and permittivity. One should decide before the design process if a fixed geometry is desired and then the permittivity is altered or vice versa. While changing the permittivity in solids is complicated, it is a rather simple exercise when using liquids as a dielectric material. Liquids can be mixed; thus the permittivity of the mixture can be adjusted. Water has a permittivity of around 80 at room temperature and, due to its natural abundance, is an interesting and inexpensive material for preliminary experiments. In order to change its permittivity, it can be mixed with alcohols for example. Unfortunately, the permittivity is very often too low for design purposes. In our laboratory an interesting alternative to solids was established involving using powdery high permittivity materials that are mixed with water to obtain thick, high permittivity slurries. These slurries can then be filled either into containers with the desired shape or even into bags

that allow conformal placement of high permittivity materials to the human body. These materials have proven very valuable for high field magnetic resonance imaging as they allow the creation of secondary B_1 fields in areas that otherwise suffer low signal intensity [36].

DESIGN BASED ON ELECTROMAGNETIC SIMULATIONS

Nowadays, electromagnetic simulation is widely available. Commercial packages exist that allow fast convergence and simple computation of resonant structures. Especially when simulating highly resonant structures, eigenmode analysis becomes a valuable tool. Electromagnetic simulation software permits modal distribution calculation over a specified bandwidth and the visualization of magnetic and electric field distribution for each of the calculated modes.

In general, two major types of three dimensional electromagnetic analysis for non-radiating structures exist:

1. driven modal analysis
2. eigenmode analysis

While the driven modal analysis uses an external excitation source via wave-ports, eigenmode analysis does not need excitation ports, as stored energy within the structure exists. The driven modal analysis yields s-parameters and the internal fields while the eigenmode analysis gives, additionally to the fields of each mode, also the natural modes and resonances. However, the eigenmode analysis does not provide s-parameters. Driven modal analysis is more often used as the computed s-parameters can be compared with those that have been obtained from a prototype of the resonator.

A characteristic of electromagnetic simulation is that it needs the geometry that the dielectric is to take as an input parameter. For a simple cylinder it is enough to specify the radius and height as well as the material properties. The boundary conditions and background material need to be set and then the simulation can be started. As there are numerous modes possible, one must specify for the simulator how many modes it shall compute. If set up correctly, one of the first modes found by the software should be the TE01δ mode. The calculation time for the first five modes of a model with about 20.000 tetrahedrons is about 20 seconds on a workstation with a single six core Intel Xeon e-1650v3 CPU equipped with 32 gigabytes of random access memory. An increased number of tetrahedrons will give a bit improved accuracy but also will make the computation

effort significantly larger. As an example, for a cylinder with radius 43 millimeters and a height of 39 millimeters filled with distilled water as a dielectric, the first five modes were calculated. The result is shown in figure 1.18.

Solver order: 2nd (constant)
Curved elements: up to order 3 (automatic)

Estimation frequency: 50 MHz

Adaptive Computation

Pass 1:

Eigenmode solver results:

Mode	Frequency	Accuracy
1	418.3124 MHz	1.252e-007
2	538.4263 MHz	1.203e-007
3	538.4678 MHz	1.312e-007
4	569.5293 MHz	2.099e-007
5	569.5693 MHz	1.748e-007

Marked 1570 of 5827 for refinement.

Pass 2:

Eigenmode solver results:

Mode	Frequency	Accuracy
1	417.6731 MHz	9.148e-008
2	538.1474 MHz	3.598e-007
3	538.1558 MHz	1.931e-007
4	569.0552 MHz	1.848e-007
5	569.061 MHz	2.127e-007

Desired accuracy limit reached, mesh adaptation stopped.

Figure 1.18: Simulation results for dielectric resonator. The first five modes have been calculated. The modes two and three as well as four and five are orthogonal modes: the have the same modal pattern but are orthogonal to each other. These modes can be fed in quadrature like the HEM11δ mode.

The software then allows also for a visualization of the single modes: both the electric field and the magnetic field can be visualized. The electric field for the first mode found from figure 1.18 is given in figure 1.19.

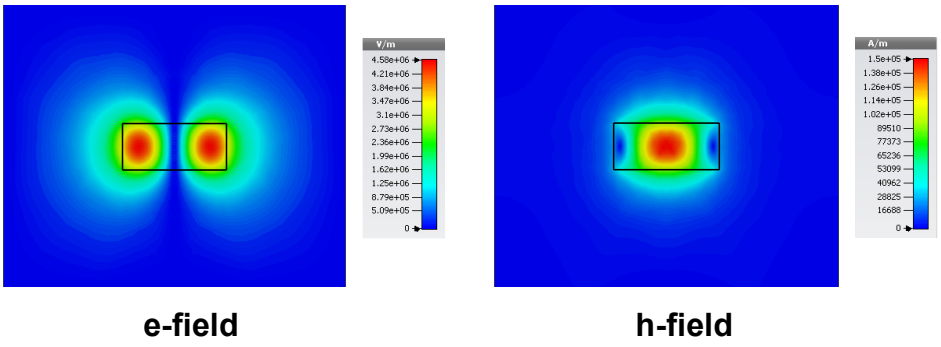


Figure 1.19: Visualization of the electric and magnetic field of the first mode of a cylindric dielectric resonator. The view shows the amplitude of the electric field (left) and the magnetic field (right) in a transversal cut plane through the cylinder.

In our laboratory we used eigenmode analysis due to its fast convergence and thus

reduced computing time. In order to verify the frequencies of the modes we measured the S11-parameter (reflection response) with a simple pickup loop attached to a network analyzer like in figure 1.20.

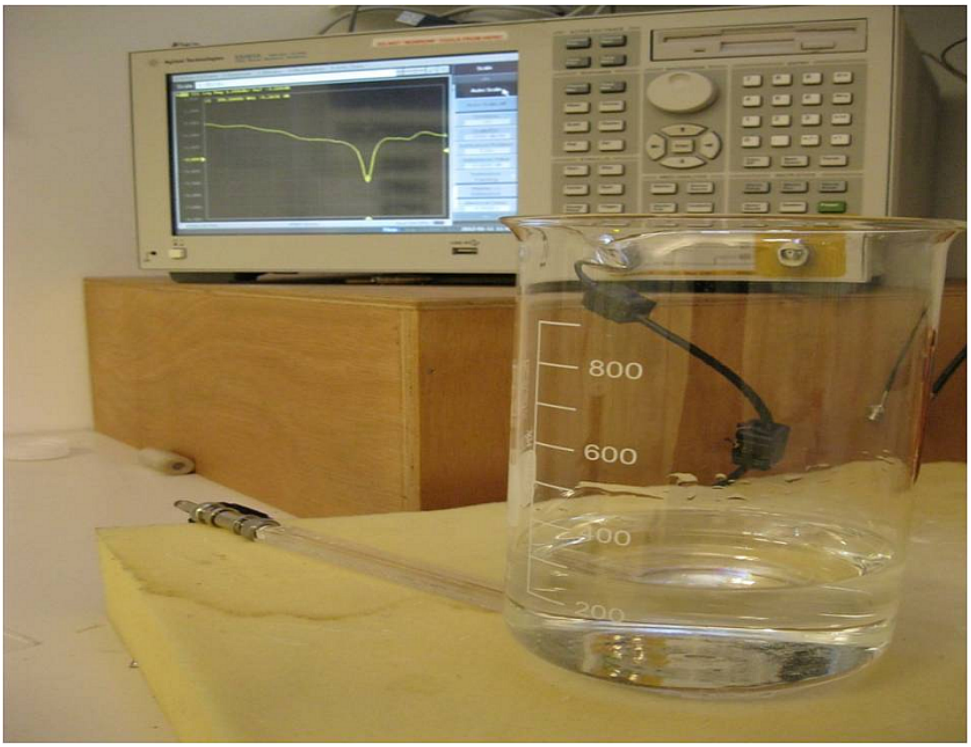


Figure 1.20: Verification of the simulation: a simple loop probe is used to couple into the dielectric resonator (in this case a beaker filled with distilled water). The S11-parameter is measured and the frequency response of the mode can be seen on the network analyser.

Eigenmode analysis is a valuable tool for the design of DRAs, but it has its limitations: due to the nature of eigenmode analysis it is for example not possible to examine a coaxial cylinder with two different permittivities. One would get only the modes for each cylinder not for the superposition e.g. the whole device. However, the coaxial case is quite interesting for magnetic resonance imaging as it represents the case when a dielectric cylinder is loaded with a human body. In those cases, one has to go back to finite difference time domain methods in order to solve the Maxwell equations to get the field distributions for such a device in the loaded case. In those simulations also, excitation ports need to be defined. So far we have implemented this via loops that couple inductively into the DRA.

DESIGN BASED ON EMPIRICAL DERIVED FORMULAS

While closed formulas for an isolated, e.g. surrounded by a conducting wall, DRA exist, those analytical solutions are of very limited help when determing the resonant frequency of a real-world DRA [25]. However, a number of empirical derived expressions exist in the literature [19] that allow the calculation of the lowest resonant frequencies of the TE01δ, HEM11, and TM01 modes for cylindrical DRAs:

$$f_{TE_{01\delta}} = 2.961 \frac{c\epsilon_r^{-0.465}}{2\pi a}\left[0.691 + 0.319\frac{a}{h} - 0.035\left(\frac{a}{h}\right)^2\right] \tag{1.15}$$

$$f_{HEM_{11\delta}} = 2.735 \frac{c\epsilon_r^{-0.436}}{2\pi a}\left[0.543 + 0.589\frac{a}{h} - 0.05\left(\frac{a}{h}\right)^2\right] \tag{1.16}$$

$$f_{TM_{01}} = 2.933 \frac{c\epsilon_r^{-0.468}}{2\pi a}\left[1 - \left(0.075 - 0.05\frac{a}{h}\right)\left(\frac{\epsilon_r - 10}{28}\right)\right]\left[1.048 + 0.377\frac{a}{h} - 0.071\left(\frac{a}{h}\right)^2\right] \tag{1.17}$$

where ϵ_r is the permittivity of the resonator, a the radius and h the height in meters.

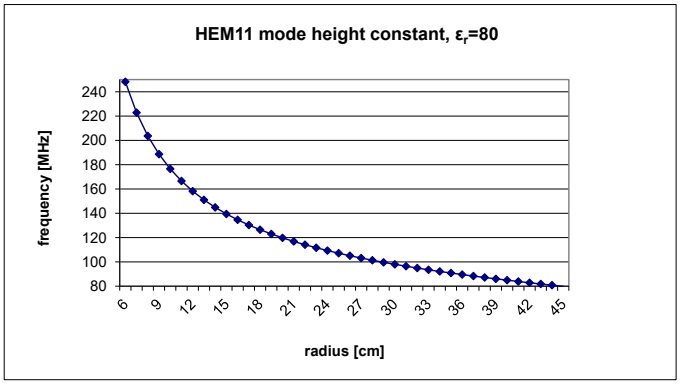


Figure 1.21: An example for a HEM_{11} mode design based on empirical derived formulas. By inserting equation 1.16 into a spread sheet simple design calculations can be made. In this example the height of the cylinder and permittivity were fixed. Now one can choose conveniently the right radius for the required frequency. This example also shows that a water based dielectric resonator would become quite large with a radius of about 20 cm.

1.7. PLASMA ANTENNAS

1.7.1. INTRODUCTION TO PLASMA

CHAPTER five of this thesis introduces a new type of magnetic resonance imaging coil that is based on plasma. As this is a new concept to the world of magnetic resonance imaging a brief introduction into plasma is given here.

The English physicist Sir William Crookes suggested in 1879 [8], while considering the properties of matter in electrical discharges, that these gases are the fourth state of matter. The terminology follows the idea that changes in the state of matter can be achieved by adding energy, for example in the form of heat as shown as in figure 1.22. The term plasma was first introduced by Tonks and Langmuir [38] in the 1920s.

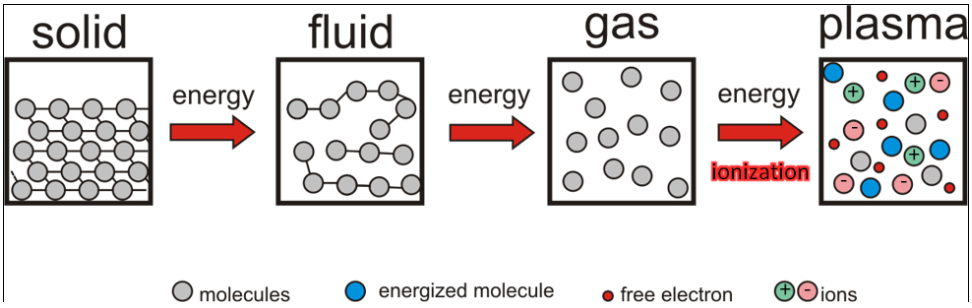


Figure 1.22: Plasma as the fourth state of matter: by adding energy to a solid first a liquid state is created which goes into a gas state if further energy is added. If even more energy is added the molecules in the gas start to ionize thus the gas becomes a plasma. While in the first three phases molecules and atoms move as one unit in the plasma phase ions and electron move separately. Instead of energy or heat one can also define the state of matter by the average kinetic energy per particle.

A gas which is normally an electric insulator becomes a good electrical conductor when it is turned into a plasma. This is because in a plasma a large number of free electrons and positive ions exist alongside neutral atoms and molecules. These electric charges can move freely and are responsible for the electric conductance of the plasma and the quasi-neutrality of plasma. The amount of ionization of a plasma can be described by the ratio of $n_e/(n_e+n_n)$ where n_e is the number of electrons and n_n the density of neutral atoms. The amount of ionization in a fluorescent tube for example is of the order of $\sim 10^{-5}$. A plasma is considered weakly ionized if the degree of ionization is less than 10^{-4}.

The plasma inside a confinement chamber is quasi-neutral because where the plasma

faces a boundary a sheath is formed as shown as in figure 1.23. The effect is similar to metals, that are inside potential free when exposed to an external electric field after a certain distance (also known as the skin depth effect). The sheath shields the inner plasma from the electric field as charge is allowed to concentrate in close proximity to the boundary.

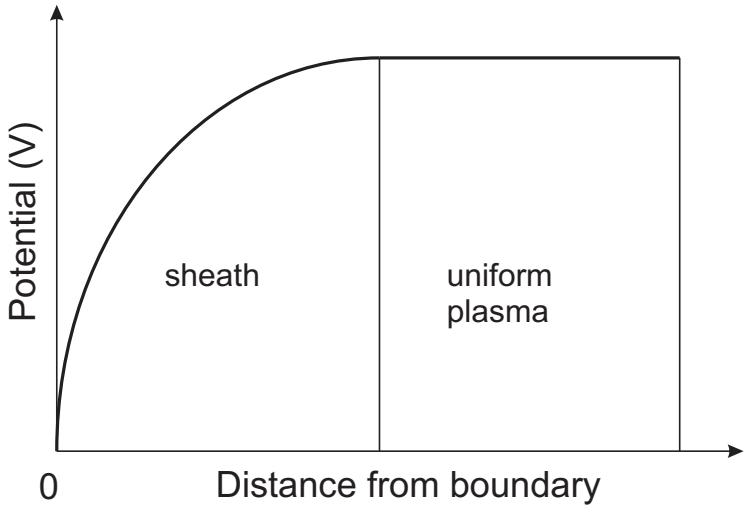


Figure 1.23: A plasma forms a sheath at its borders. While inside the plasma quasi-neutrality is given there is a difference in potential at the border of the plasma. In the sheath region electrons form a shield against the boundary. This means that positive ions will not reach the plasma wall and can thus not leave the plasma. The sheath is a conducting outer layer that is capable of guiding surface waves.

Usually a plasma is described in terms of pressure, density and temperature using statistical mechanics. It is common to classify plasmas according to their density and temperature. The pressure in a plasma is usually calculated by

$$P = \rho T \tag{1.18}$$

where P is the pressure, ρ is the density and T is the temperature.

In general, the forces between the charges inside a plasma can be described using Coulombs law. In a plasma, a positive ion will be surrounded (shielded) by an electron cloud. Coulomb's law does not take shielding of charged particles into account as the several shielding layers restrict the force of attraction of the ion to a finite distance and

not infinity. The shielding of a single charged particle that is taking place in plasmas is the same as in liquids containing ions as has been described by the Dutch physicist Peter Debye. As the shielding of one positive ion is omnidirectional in space, it describes a sphere around the ion, this effect is known as Debye shielding. The aforementioned statements are true for weakly ionized plasma. In a fully ionized plasma the particles are subject only to Coulomb collisions. It is possible, according to [15] to calculate the Debye length λ_d for cases where the ions mobility is negligible as

$$\lambda_d = \sqrt{\frac{\epsilon_0 k_b T_e}{n_e q_e^2}} \tag{1.19}$$

with ϵ_0 being the permittivity of free space, k_b is Boltzmann's constant, T_e the electron temperature, n_e the electron density and q_e is the electron charge.

It is furthermore known that the electrons in a plasma are collectively oscillating, a motion that can be described using wave equations. The ions in the plasma are also moving collectively in a wave form, however at a lower frequency. The collision frequency depends on the 'mean free path' which is defined as the average distance a particles travels between collisions within its medium. The collision frequency is inversely proportional to the density of the medium. The mean free path in solids is usually smaller than in a liquid and much smaller in a gas. As in a plasma mean free paths can be similar to all those three states of matter, also the cross section is invoked to describe the probability of collision. As charged particles are investigated, the cross section is not based on geometry but rather by using the effective area of the electric forces, as this also takes relative speed of the particles into account. The oscillations that arise from disturbances from equilibrium can be described as an angular frequency ω_p (also known as plasma frequency) with

$$\omega_p = \sqrt{\frac{n_e q_e^2}{\epsilon_0 m_e}} \tag{1.20}$$

where n_e is the electron number density (measured in m^{-3}), m_e the electron mass, ϵ_0 the permittivity of free space, and q_e the electron charge. The plasma frequency determines the behaviour of the plasma with respect to electromagnetic waves.

The field of plasma physics is a complex field and the reader can find more information in [1, 13] and [15].

The idea of using plasma as antennas is not entirely new and has been tried in the

fields of communication and radar before [3, 4]. The main reason to use plasma in such fields are the unique properties that plasma antennas offer:

- small radar cross-section when the plasma antenna is not energized
- reconfiguration of the transmit and receive bandwidth by reconfiguring the plasma
- lower noise levels than metal antennas if needed
- plasma can be switched off and on as needed

The plasma can be formed by two electrodes like in AC-mains lighting. However multiple other means of plasma excitation exist such as:

- laser beam
- electric fields
- microwave and RF energy
- chemical process
- contact ionisation
- adiabatic compression
- electron beam
- beam of particles

A well written overview of possible excitation technologies can be found in the publication from Conrads [7].

Yet another interesting means of excitation was suggested by Moisan [22] and Burykin [5]. A plasma column can be excited by a surface wave that is driven from one end of a column. This surface wave can travel along the plasma column for frequencies lower than the plasma frequency. According to Borg [4], the current induced by the surface wave along the column can, under the right circumstances, be very similar to that of a wave propagating on a metallic dipole antenna. This makes plasma columns (that can be used as a mono- or dipole) an interesting candidate for use in high field MRI where several new coil designs using dipoles have been shown to be very promising [16, 28–30, 42].

REFERENCES

[1] P. Bellan. *Fundamentals of plasma physics*. Cambridge University Press, 2006.

[2] F. Bloch. Nuclear induction. *Physical review*, 70(7-8):460, 1946.

[3] G. Borg, J. Harris, N. Martin, D. Thorncraft, R. Milliken, D. Miljak, B. Kwan, T. Ng, and J. Kircher. Plasmas as antennas: Theory, experiment and applications. *Physics of Plasmas (1994-present)*, 7(5):2198–2202, 2000.

[4] G. Borg, J. Harris, D. Miljak, and N. Martin. Application of plasma columns to radiofrequency antennas. *Applied physics letters*, 74(22):3272–3274, 1999.

[5] I. I. Burykin, S. Levitskii, and V. Martynenko. The radiation of electromagnetic waves by a variable cross section cylindrical plasma waveguide. *Radio Engineering and Electronic Physics*, 20:86–91, 1975.

[6] C. M. Collins, W. Liu, W. Schreiber, Q. X. Yang, and M. B. Smith. Central brightening due to constructive interference with, without, and despite dielectric resonance. *Journal of Magnetic Resonance Imaging*, 21(2):192–196, 2005.

[7] H. Conrads and M. Schmidt. Plasma generation and plasma sources. *Plasma Sources Science and Technology*, 9(4):441, 2000.

[8] W. Crookes. On a fourth state of matter. *Proceedings of the Royal Society of London*, 30(200-205):469–472, 1879.

[9] O. Dietrich, M. F. Reiser, and S. O. Schoenberg. Artifacts in 3-t mri: physical background and reduction strategies. *European journal of radiology*, 65(1):29–35, 2008.

[10] U. Gersch and A. Loesche. Untersuchungen der paramagnetischen kernresonanzabsorption im kondensatorfeld. *Annals of Physics*, 455(1-6):167–172, 1957.

[11] J. Griffiths. *Introduction to Electrodynamics*. Prentice Hall, 1999.

[12] E. Haacke, R. Brown, M. Thompson, and R. Venkatesan. *Magnetic Resonance Imaging: Physical Principles and Sequence Design*. John Wiley & Sons, 1999.

[13] J. Harry. *Introduction to Plasma Technology*. Wiley-VCH, 2010.

[14] P. Hofmann. *Solid State Physics: An Introduction*. Wiley-VCH, 2008.

[15] U. Inan and A. Golkowski. *Principles of Plasma Physics for Engineers and Scientists*. Cambridge University Press, 2011.

[16] O. Ipek, A. Raaijmakers, J. Lagendijk, P. Luijten, and C. van den Berg. Optimization of the radiative antenna for 7-t magnetic resonance body imaging. *Concepts in Magnetic Resonance Part B: Magnetic Resonance Engineering*, 43(1):1–10, 2013.

[17] J. Jackson. *Classical Electrodynamics*. Wiley, 1962.

[18] A. Khanna. Review of dielectric resonator oscillator technology. In *1987 IEEE International Frequency Control Symposium Proceedings*, pages 478–486, 1987.

[19] A. Kishk, A. Glisson, and G. Junker. Bandwidth enhancement for split cylindrical dielectric resonator antennas. *Progress In Electromagnetics Research*, 33:97–118, 2001.

[20] P. C. Lauterbur. Image formation by induced local interactions: examples employing nuclear magnetic resonance. *Nature*, 1973.

[21] P. Mansfield. Multi-planar image formation using nmr spin echoes. *Journal of Physics C: Solid State Physics*, 10(3):L55, 1977.

[22] M. Moisan, A. Shivarova, and A. Trivelpiece. Experimental investigations of the propagation of surface waves along a plasma column. *Plasma physics*, 24(11):1331, 1982.

[23] OECD. *Health at a glance 2015: OECD Indicators*. OECD Publishing, 2015.

[24] A. Okaya and L. Barash. The dielectric microwave resonator. *Proceedings of the IRE*, 50(10):2081–2092, 1962.

[25] A. Petosa. *Dielectric Resonator Antenna Handbook*. Artech House Publishers, 2007.

[26] D. Pozar. *Microwave Engineering*. Wiley, 2011.

[27] E. M. Purcell, H. Torrey, and R. V. Pound. Resonance absorption by nuclear magnetic moments in a solid. *Physical review*, 69(1-2):37, 1946.

[28] A. Raaijmakers and C. Berg. Antennas as surface array elements for body imaging at ultrahigh field strengths. *eMagRes*, 2012.

[29] A. Raaijmakers, O. Ipek, D. Klomp, C. Possanzini, P. Harvey, J. Lagendijk, and C. Van den Berg. Design of a radiative surface coil array element at 7 t: The single-side adapted dipole antenna. *Magnetic Resonance in Medicine*, 66(5):1488–1497, 2011.

[30] A. Raaijmakers, P. Luijten, and C. Berg. Dipole antennas for ultrahigh-field body imaging: a comparison with loop coils. *NMR in Biomedicine*, 2015.

[31] H. Rahbar, S. C. Partridge, W. B. DeMartini, B. Thursten, and C. D. Lehman. Clinical and technical considerations for high quality breast mri at 3 tesla. *Journal of Magnetic Resonance Imaging*, 37(4):778–790, 2013.

[32] T. Redpath. Signal-to-noise ratio in mri. *The British Journal of Radiology*, 71(847):704–707, 1998.

[33] R. Richtmyer. Dielectric resonators. *Journal of Applied Physics*, 10(6):391–398, 1939.

[34] M. Rogalski and S. Palmer. *Solid State Physics*. Gordon and Breach Science Publishers, 2000.

[35] O. Sager and F. Tisi. On eigenmodes and forced resonance-modes of dielectric spheres. *Proceedings of the IEEE*, 56(9):1593–1594, 1968.

[36] J. E. M. Snaar, W. M. Teeuwisse, M. J. Versluis, M. A. van Buchem, H. E. Kan, N. B. Smith, and A. G. Webb. Improvements in high-field localized mrs of the medial temporal lobe in humans using new deformable high-dielectric materials. *NMR in biomedicine*, 24(7):873–9, aug 2011.

[37] B. J. Soher, B. M. Dale, and E. M. Merkle. A review of mr physics: 3t versus 1.5 t. *Magnetic resonance imaging clinics of North America*, 15(3):277–290, 2007.

[38] L. Tonks and I. Langmuir. Oscillations in ionized gases. *Physical Review*, 33(2):195, 1929.

[39] K. Uchino. Glory of piezoelectric perovskites. *Science and Technology of Advanced Materials*, 2016.

[40] P. Van Musschenbroek. *Essai de physique*, volume 2. Chez Samuel Luchtmans, Imprimeur de l'Université, 1751.

[41] T. Vanderah. Talking Ceramics. *Science*, 298(5596):1182–1184, 2002.

[42] L. Winter, C. Özerdem, W. Hoffmann, D. Santoro, A. Müller, H. Waiczies, R. Seemann, A. Graessl, P. Wust, and T. Niendorf. Design and evaluation of a hybrid radiofrequency applicator for magnetic resonance imaging and rf induced hyperthermia: electromagnetic field simulations up to 14.0 tesla and proof-of-concept at 7.0 tesla. *PloS one*, 8(4):e61661, 2013.

[43] Q. Yang, J. Wang, and X. Zhang. Analysis of wave behavior in lossy dielectric samples at high field. *Magnetic Resonance in Medicine*, 47(5):982–989, 2002.

2

DESIGN AND EVALUATION OF A DETUNABLE WATER-BASED QUADRATURE HEM_{11} MODE DIELECTRIC RESONATOR AS A NEW TYPE OF VOLUME COIL FOR HIGH FIELD MRI

Sebastian A. AUSSENHOFER

Andrew G. WEBB

Parts of this chapter have been published in Magnetic resonance in medicine: official journal of the Society of Magnetic Resonance in Medicine **68**, 1325-31 (2012) [4].

2

An annular dielectric resonator made from distilled water has been designed to operate in degenerate quadrature HEM_{11} modes at 298.1 MHz (7 Tesla). The circularly polarized B_1^+ field has a high degree of homogeneity throughout a sample placed within the annulus. The sensitivity of the resonator was measured to be essentially identical to that of an eight-rung high-pass birdcage resonator with the same physical dimensions. High resolution in vivo images have been obtained from the human wrist. A new method of electronically detuning the resonator has also been evaluated. The design is extremely simple and rapid to build, with direct applicability to very high field imaging and also potential integration into human and animal hybrid position emission tomography (PET)/MRI and single-photon emission computed tomography (SPECT)/MRI systems due to the lack of conductor attenuation-induced artefacts in the reconstructed nuclear medicine images.

2.1. INTRODUCTION

DESIGNING radiofrequency (RF) coils for magnetic resonance (MR) becomes increasingly challenging at high values of the (operating frequency*coil diameter) product due to well-characterized increases in wavelength effects, radiation loss, and loss in capacitive lumped elements used for resonating and impedance matching the coil. Substitution of transmission line for lumped elements can mitigate some, but not all, of these effects ([14],[15]), with these transmission lines being used either in volume coils or as individual elements of a transmit array [11],[1]. In contrast to MR, electron paramagnetic resonance, which operates over a large frequency range from low GHz (X-band) to several hundreds of GHz (F- and D-band and above) primarily uses cavity resonator designs. Although some MR coil designs do have elements of resonant cavity behaviour, the emphasis for designing high field volume coils has so far been on adapting existing geometries from lower field strengths.

One promising candidate for a different type of high field MR coil is a dielectric resonator (DR) constructed from high permittivity material. DRs are used extensively in the communications and satellite industries. A large number of pure and mixed electromagnetic modes can be supported in a DR depending upon the geometry of the resonator. Computed modal structures of the spatial distribution of the magnetic and electric fields of cylindrical DRs have been shown by Kajfez et al. [8]. Visualization using MRI of many modes of a cylindrical DR has recently been demonstrated [16]. The two lowest frequency modes, the $TE_{10\delta}$ and $HEM_{11\delta}$ are shown in Figure 2.1, with the abbreviations representing transverse electric (TE) and hybrid electromagnetic (HEM), respectively. Different modes are identified by three subscripts m, n, and p, which denote the number of half-wave-length field variations in the azimuthal (ϕ), radial (ρ), and height directions, respectively. The subscript δ is applied when there is less than half-a-wavelength variation in the height-direction. A small number of studies have used DRs in high field MR microscopy [12],[5], as well as one proof-of-principle using a 4 Tesla human scanner [17] using exclusively the $TE_{01\delta}$ mode. The same is true for electron paramagnetic resonance studies, reviewed in Ref. [3]. As shown in Figure 2.1, the $TE_{01\delta}$ mode has a maximum magnetic field component along the major axis of the cylinder (which also corresponds to the location of minimum electric field). However, for MR studies the long axis must be oriented somewhat awkwardly perpendicular to the B_0 field, and it is clearly not possible to operate this mode in quadrature: both of these factors make this mode less than optimal for in vivo imaging experiments. In contrast, two frequency-degenerate orthogonal HEM_{11} modes exist [8] and if the long axis of the cylinder is aligned parallel to B_0 then

quadrature operation is possible. A series of empirical expressions have been derived for the resonance frequencies of the lowest modes of a cylindrical DR [9]. For the HEM_{11} mode this frequency is given by:

$$f_{HEM_{11\delta}} = 2.735 \frac{c\epsilon_r^{-0.436}}{2\pi a}\left[0.543 + 0.589\frac{a}{h} - 0.05\left(\frac{a}{h}\right)^2\right] \tag{2.1}$$

where c is the speed of light, ϵ_r the relative permittivity, a the radius and h the height of the resonator. Although small MR resonators made from high permittivity, low loss materials have been constructed [12],[5], these have required sophisticated fabrication processing involving high pressure compression and controlled sintering conditions, which are very difficult for the larger structures required for in vivo imaging. In contrast, simple deionized water has a high relative permittivity (ϵ_r = 78 at room temperature) and relatively low loss at radio-frequencies (although the loss increases significantly in the microwave range). Application of Eq. 2.1 shows that the dimensions (diameter and length) required for the HEM_{11} mode to resonate at 298.1 MHz (7 Tesla) are of the order of centimetres to tens of centimetres, which lie in the range required for in vivo imaging. For practical applications an annular rather than cylindrical shape must be used, with a clear bore through the centre of the cylinder in order to image the volume of interest. In this article, the properties of such a resonator are investigated in terms of design, efficiency and applicability to in vivo imaging of extremities such as the human wrist. In addition, a new method to detune the resonator is proposed, which would allow integration of receive arrays into the overall design.

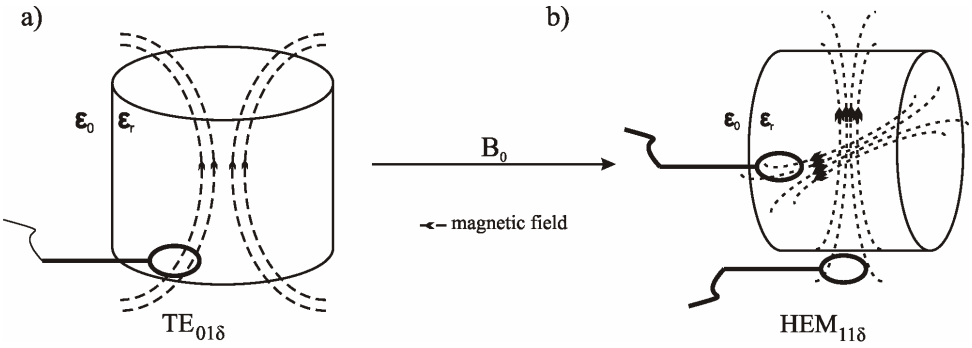


Figure 2.1: Schematic of the magnetic field distributions in the two lowest frequency modes of a cylindrical DR [8]. The $TE_{01\delta}$ mode must be used with the long axis of the cylinder perpendicular to the B0 field, and therefore can only be driven in a linear mode. In contrast, for the $HEM_{11\delta}$ mode the long axis of the cylinder is parallel to B_0 and the two orthogonal modes can be driven in quadrature.

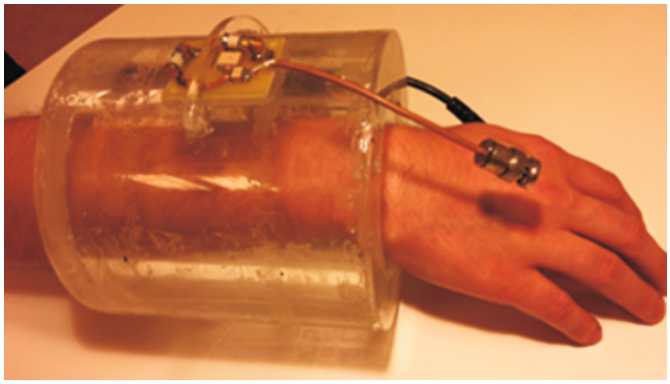
2.2. METHODS

2.2.1. HEM RESONATOR DESIGN

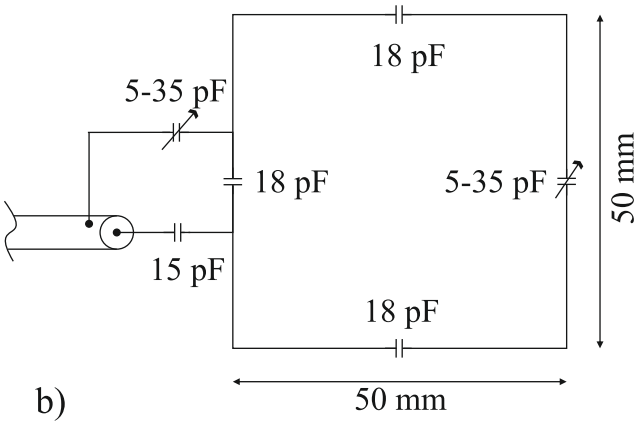
An outer diameter of 140 mm was chosen for the HEM resonator. Based upon Eq.2.1 the HEM_{11} modes resonate at a frequency of 298.1 MHz for a water column height of 72.5 mm. Resonant modes of the water cylinder were detected experimentally using S_{11} measurements from a non-resonant, balanced pick-up loop (diameter 2 cm) on a network analyzer (EN5061, Agilent Technologies, Santa Clara). The $HEM_{11\delta}$ mode was detected using this pick-up loop placed at the side of the resonator: the measured height of the water was 73 mm. The annular HEM_{11} mode resonator was made from two concentric polymethylmethacrylate tubes (Vink Kunststoffen, The Netherlands) creating a cavity of 140 mm outer and 100 mm inner diameters. The height (15.2 cm) of the annulus was obtained empirically on the workbench by filling with distilled water until the HEM_{11} mode was at 298.1 MHz (with a volunteer's wrist in the central bore of the annulus). Polymethylmethacrylate annular rings were constructed and glued to make a closed annulus: filling ports were drilled into the end plates and sealed with a plastic screw and hot glue.

Two inductively coupled impedance matching networks were placed at the centre of the long axis of the resonator at a distance of 3 cm from the outside surface of the resonator, 90 degrees apart from each other. These consisted of 5 cm square coils etched on FR4 PC board, and segmented with three fixed capacitors (American Technical Ceramics, Huntington Station, NY) and two 1–30 pF variable capacitors (Voltronics, Salisbury, MD) for fine tuning. The topology of the coupling loops as well as the impedance matching network is shown in Figure 2.2. The coupling loops were tuned to provide critical coupling to the HEM resonator with a 50 Ohm impedance match. The coil was interfaced to the scanner by using 40 cm long double-shielded 50 Ohm coaxial cables (K02252, Huber & Suhner, Switzerland).

The HEM resonator was matched and tuned when loaded with a human wrist and achieved a S_{11} of –20 dB or better. For different loading conditions (i.e., wrists of different volunteers) the tuning of the HEM resonator itself was not changed, with only slight adjustments to the variable capacitor of the impedance matching circuit required to re-establish critical coupling. A photograph of the HEM coil is shown in Figure 2.2.



a)



b)

Figure 2.2: a) Photograph of the water-based HEM resonator with quadrature inductive feeds. b) Topology of the coupling loops and the impedance matching network.

2.2.2. DETUNING THE HEM RESONATOR

In order to be able to use the HEM resonator with a receive array it must be electronically detunable. Electrical detuning of a DR by mounting a conducting ring on top of the resonator has been suggested in [7]. However, this only produced a very small change (~75 kHz) for the particular configuration used here.

An alternative detuning mechanism was therefore developed. It was observed that a wire bent into a half circle with legs perpendicular to the half circle shifts the frequency of one of the HEM modes by several tens of MHz if the legs are submersed into the dielectric media while having the half-circle submersed in the medium. If the half-circle is not submerged but positioned slightly above the medium (see Fig. 2.3) then the shift is ~8 MHz. In either case the orthogonal mode is not affected. Rotating the detuning structure by 90 degrees produces the corresponding effect on the orthogonal mode. If a gap (open circuit) is introduced into the centre of the half-circle then the mode structure is not affected, suggesting that introduction of a positive intrinsic negative (PIN)-diode can be used to convert the mechanical structure into an electronically controlled detuning mechanism.

The final detuning device was constructed from a half circle etched out of FR4 (Bungard, Germany) with a diameter of half of the annulus wall width and a track width of 5 mm. In the center of the half circle, a PIN-diode (MA4P7441F-1091, Macom, Lowell, MA) was placed with two series RF chokes of 2600 nH, and 1000 pF blocking capacitors either side. Two stiff copper wires (1.6 mm diameter, length 5 cm) were via-mounted and soldered to the half circle. The wires were then submerged into the HEM resonator through holes parallel to the z-axis of the resonator. The topology of the device is given in Figure 2.3. Detuning of the impedance matching loops was performed using a conventional approach using PIN-diode switching: the topology of this circuit is given in Figure 2.3a.

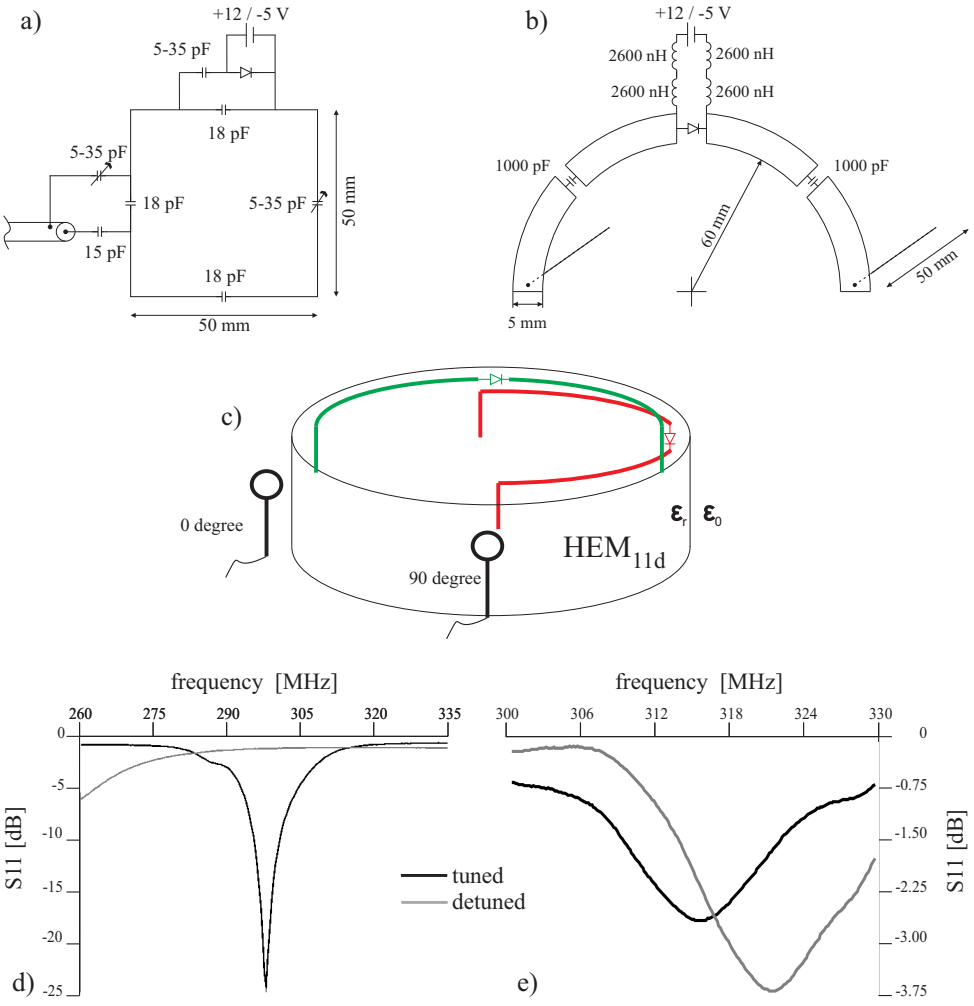


Figure 2.3: a) Topology of the detune-able coupling loops with PIN-diodes. b) Topology of the detuning wire device. c) Schematic of the placement of the detuning devices with respect to the feeding loops. d) S_{11} measurement of the HEM resonator with the coupling loops "tuned" (black line) and "detuned" (gray line). e) S_{11} measurement of the HEM resonator alone (using a nontuned pick-up loop) in the tuned (diodes nonconducting, black line) and detuned (diodes conducting, gray line) cases. Smaller spurious "dips" are due to the pick-up coil itself.

2.2.3. BIRDCAGE COIL

For sensitivity comparisons a quadrature birdcage coil was constructed from the same concentric polymethylmethacrylate tubes (for the RF shield and coil), thus having the same absolute dimensions (outer and inner diameter as well as length) as the HEM resonator. An eight-rung high pass design was used. The rungs and end-rings were constructed from 13 mm wide copper strips (3M, Minneapolis). The end-ring capacitors were 2.1 pF fixed values (American Technical Ceramics, Huntington Station, NY). The two quadrature modes were excited by identical inductive matching networks as those used for the HEM resonator. Fine tuning of the resonance frequency for different loads was performed with additional 1–30 pF variable capacitors in the end rings of the birdcage positioned at 180 degrees to the feed points. The shield was made out of a thin (10 mm) copper sheet wrapped around the outer polymethylmethacrylate cylinder.

2.2.4. COIL CHARACTERIZATION

Two phantoms were used to characterize both coils on the network analyzer: the first phantom consisted of a plastic bottle of 80 mm diameter and a length of 200 mm (1 L volume) filled with mineral oil (ϵ_r 4). The second identically sized phantom was made from 1 L of glycerol solution (Sigma-Aldrich, Germany) with 100 mM NaCl to mimic the relative permittivity (ϵ_r50) and conductivity (σ 0.77 S/m) of human muscle tissue at 298 MHz.

2.2.5. ELECTROMAGNETIC SIMULATIONS

Electromagnetic simulations of the magnetic field distributions for both the cylindrical and annular HEM resonators were performed using a finite difference time-domain (FDTD) solver (XFDTD, Remcom, State College, PA). A single frequency Gaussian excitation pulse was applied at 298.1 MHz, with 30 cycles to ensure steady-state conditions and reached a convergence of –45 dB. The RF shield of the magnet bore was modelled as a thin copper cylinder. A mesh size of 1 by 1 by 1 mm was used for all simulations, as well exact submeshing for all structures smaller than the mesh size. The boundary conditions were chosen as perfectly matched layers with a 30 cell padding around the structure to avoid reflections. As the structure is highly resonant the resonance condition of the unloaded DR was verified by an eigenmode solver simulation (CST, Darmstadt, Germany). Computational time on a 4-core PC was approximately 40 min for the FDTD simulations and 1–2 min for the eigenmode solver. For the evaluation of the local specific absorption

rate (SAR) (10 g average) both coils in the simulation were loaded with a human muscle phantom (relative permittivity 58.2 and conductivity 0.77 S/m) to simulate SAR. Radiation loss in the unshielded HEM was compared to both an unshielded and shielded birdcage.

2.2.6. MRI EXPERIMENTS

All imaging and B_1^+ mapping experiments were conducted on a 7T whole body human MRI scanner (Philips Achieva, Best, The Netherlands). B_1^+1 maps in the oil phantom were produced using the method of Yarnykh et al. [18]. A three-dimensional gradient echo sequence was used with the following parameters: field-of-view (FOV) 160 by 160 by 160 mm^3, voxel resolution 2.5 by 2.5 by 2.5 mm^3, pulse repetition time (TR_1)/TR_2 30/150 ms, echo time 1.5 ms, nominal 45° tip angle at the centre of the phantom. The coil sensitivity was calculated as the B_1^+ per square root Watt of input power, with the power estimated from the measured output power of the RF amplifier taking into account measured power loss in the cables from the amplifier to the coil. Phantom experiments to characterize the linear, quadrature and anti quadrature modes of the HEM resonator used multi-slice gradient echo and spin echo sequences. Gradient echo parameters: FOV 200 by 200 by 52 mm, spatial resolution 1 by 1 by 3 mm, 16 slices, TR 82 ms, echo time 2.6 ms, tip angle 20°. Spin echo parameters: FOV 200 by 200 by 52 mm, spatial resolution 2 by 2 by 3 mm, TR 710 ms, echo time 10 ms. Images of the wrist of a healthy human volunteer were acquired using both gradient echo and spin echo sequences. Gradient echo: multi slice sequence, TR 249.5 ms, echo time 3.9 ms, tip angle 20°, data matrix 320 by 320, slice thickness 2 mm, in-plane resolution 0.5 by 0.5 mm. Spin echo: multi-slice turbo spin echo sequence, TR 8419 ms, echo time 35 ms, turbo spin echo factor 8, data matrix 332 by 216, slice thickness 2 mm, in-plane resolution 0.5 by 0.5 mm, 1 signal average, total imaging time 7 min 50 s. The study adhered to the LUMC Institutional Review Board guidelines and informed consent was obtained prior to the study.

2.3. RESULTS

2.3.1. COIL CHARACTERIZATION

NETWORK analyser measurements gave an S_{11} value for each channel of both the birdcage and HEM resonator less than –20 dB in the loaded (glycerol phantom, human wrist) and unloaded (oil phantom) cases. Isolation between the quadrature channels was also greater than 20 dB in both unloaded and loaded situations.
The performance of the detuning device was then evaluated on the bench. When the PIN-diode in the coupling loop was switched the resonance of the coupling loops was lowered about 50 MHz as shown in Figure 2.4d. The detuning of the HEM mode itself by switching the PIN- diode in the wire detuning device was about 50 MHz with the wires immersed in the water (Fig. 2.4e), with a smaller ~10 MHz shift if only the wire legs were immersed.

2.3.2. SIMULATION RESULTS

From Eq. 2.1 a water cylinder of outer diameter 140 mm has HEM_{11} resonances at 298.1 MHz at a height of 72.5 mm. Figure 2.4 shows the simulated magnetic field produced, with a small excitation loop coil placed at the side of the cylinder (for clarity only one linear mode is shown). The expected HEM_{11} mode is shown, with the magnetic field perpendicular to B_0. If the annular coil with the oil phantom in place is simulated, Figure 2.4b, the basic magnetic field distribution of the HEM_{11} mode is maintained, although the magnitude is reduced. As shown in Figure 2.4c, simulating the human wrist as a cylinder of appropriate dielectric and conductivity values (with a realistic diameter less than the inner diameter of the resonator) increases the magnitude of the magnetic field compared to the case with oil, with high homogeneity restored in the transverse plane.
The simulations showed that the local maximum for the 10 g average SAR for the HEM resonator was ~15% higher compared to the birdcage resonator for the same net system input power (1 W) and normalized to 1 W dissipated power. The radiation losses were ~15% for the (unshielded) HEM resonator, 28% for the unshielded birdcage, and 12 for the shielded birdcage.

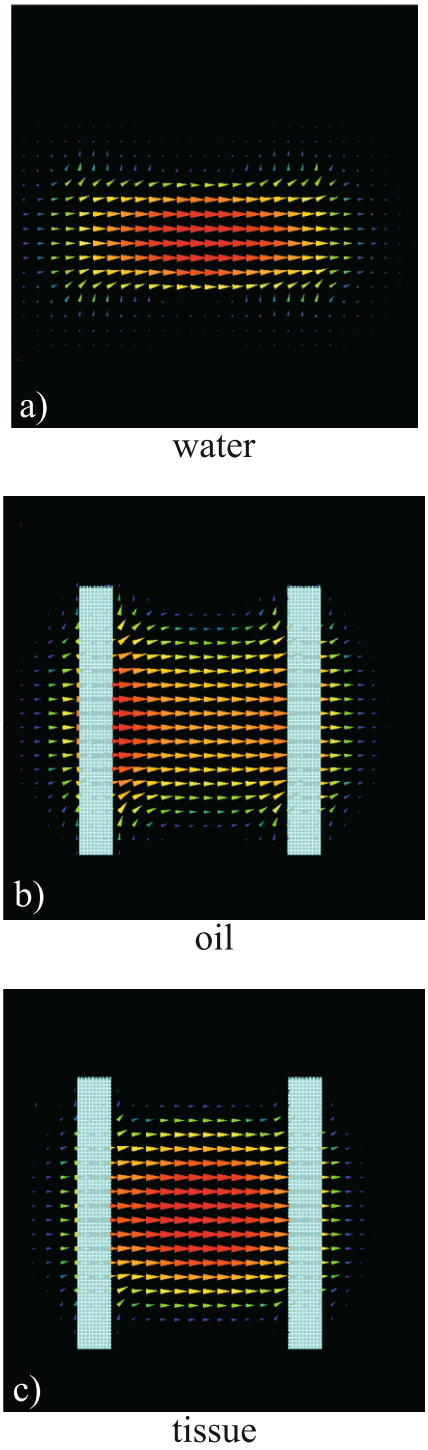


Figure 2.4: Electromagnetic simulations of the magnitude (color) and phase (direction of arrow) of the magnetic field for different configurations of the HEM resonator. a) Cylinder of water, diameter 140 mm, height 72.5 mm. b) Annulus of water, outer diameter 140 mm, inner diameter 100 mm, height 152 mm with an inner cylinder of oil ($\epsilon_r = 4$, outlined by the dotted line) with outer diameter 98 mm. c) Annulus of water, outer diameter 140 mm, inner diameter 100 mm, height 152 mm with an inner cylinder of tissue ($\epsilon_r = 50$, $\sigma = 0.77$ S/m, outlined by the dotted line) with outer diameter 80 mm to simulate the human wrist.

2.3.3. PHANTOM EXPERIMENTS

Figure 2.5 shows axial and coronal images acquired from the oil phantom with the HEM resonator. Both the gradient echo and spin echo images acquired in quadrature mode show a homogeneous signal distribution within the sample. The two separate linear modes show reduced (and mirrored) homogeneity compared to the quadrature mode, as expected. The antiquadrature mode shows very efficient "signal destruction" in the sample, indicating that the two modes are indeed circular polarized.

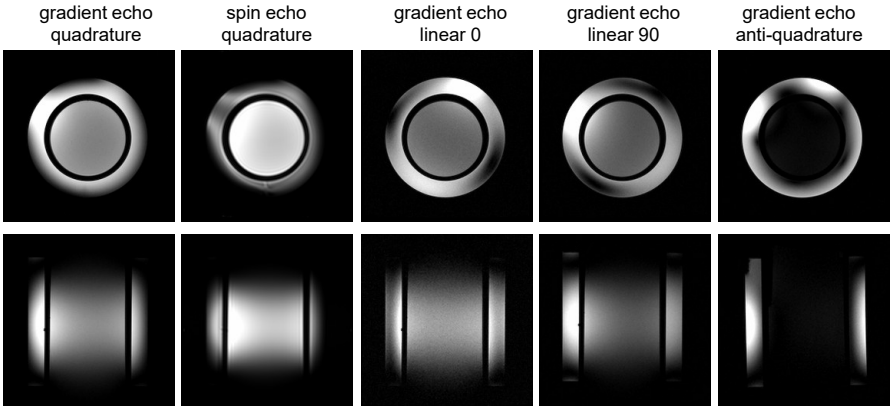


Figure 2.5: Images of an oil phantom placed symmetrically within the HEM resonator.

Experimentally acquired B_1^+ maps are shown in Figure , showing homogeneous fields in both the transverse and longitudinal directions. The magnitude of the B_1^+ field in the oil phantom is very similar to that in the water of the resonator itself. Of course this is also true for the birdcage coil, in which a large amount of energy is stored between the RF coil and the shield (although this is not possible to visualize experimentally). As a measure of the transmit field efficiency, the B_1^+ field at the centre of the phantom was determined to be 2.2 $\mu T/\sqrt{W}$ of power delivered to the coil, i.e., taking into account losses between the

RF amplifier and coil interface.

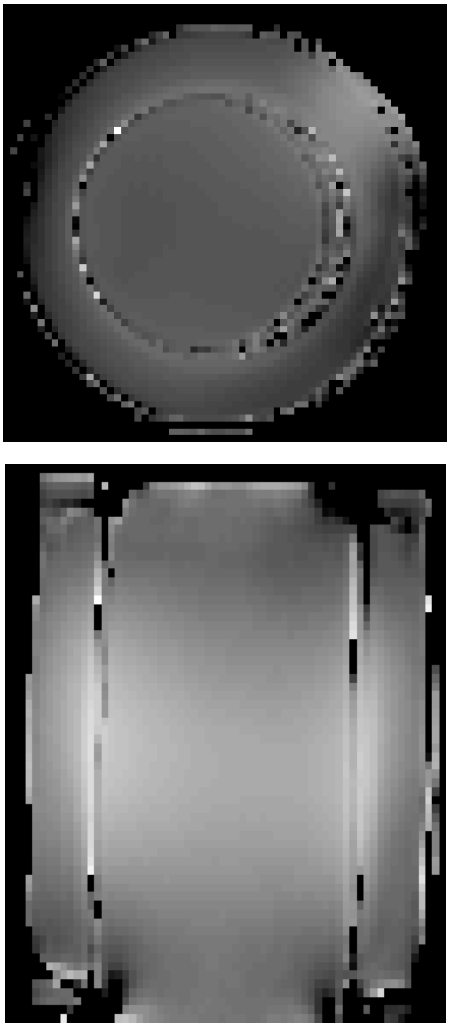


Figure 2.6: Experimentally measured B_1^+ maps in two orthogonal axes from the HEM resonator. The sensitivity at the centre of the coil is 2.2 $\mu T/\sqrt{W}$

The B_1^+ field at the centre of the phantom for the birdcage was slightly higher, with a value of 2.3 $\mu T/\sqrt{W}$. The longitudinal coverage of the HEM and birdcage coils is compared in Figure 2.7. The birdcage is seen to have a slightly broader region of homogeneity

in the centre of the FOV for the particular length-to-diameter ratio used in this article.

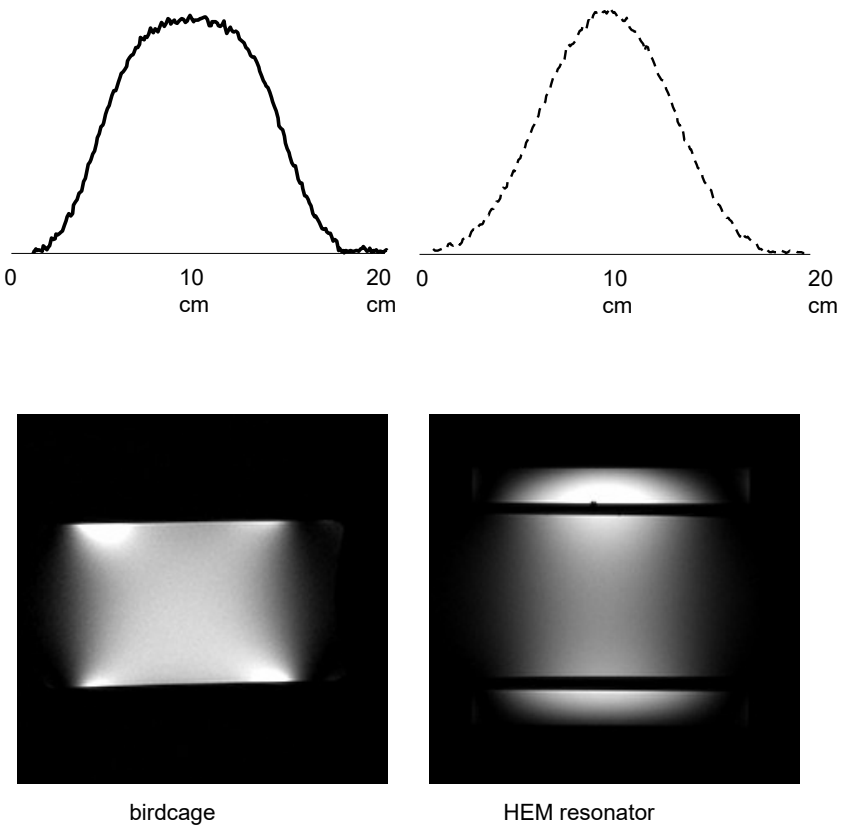


Figure 2.7: Two gradient echo images showing the longitudinal coverage of the birdcage coil (left) and HEM resonator (right).

2.3.4. IN VIVO RESULTS

Figure 2.8 shows coronal gradient echo and spin echo images from the wrist of a healthy volunteer, positioned as shown in Figure 2.2. Good visualization of the cartilage and trabecular bone is evident, as is the reasonable homogeneity in both transverse and axial dimension. No attempt was made to rigorously optimize data acquisition parameters.

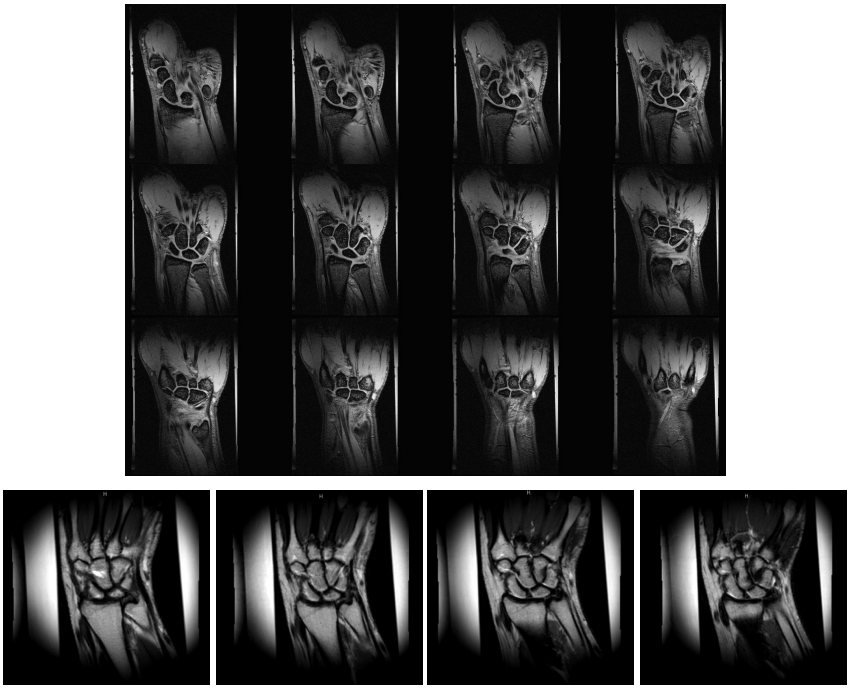


Figure 2.8: (top) Series of coronal multislice gradient echo images acquired in the human wrist using the HEM resonator. (bottom) Spin-echo images acquired using a turbo spin echo sequence

2.4. DISCUSSION

THE results presented here show that the HEM_{11} mode of a water-based DR is a promising new design for high frequency MRI. The design and construction are extremely simple, and the performance has been shown to be essentially identical to that of an equivalently-sized birdcage coil. It should be noted, however, that this sensitivity comparison is extremely conservative in the sense that the dimensions of the resonators are heavily weighted towards the optimum length-to-diameter ratio for the birdcage. Given the intrinsic nature of the HEM mode one can anticipate that a high degree of B_1 uniformity would be maintained for much smaller length-to-diameter ratios, for which the performance of the birdcage resonator degrades significantly. Considering the modes shown in Ref. [16], ratios of as low as 1:4 still produce relatively homogeneous fields, whereas the birdcage would be unusable at such dimensions. In order for the DR to be as flexible as conventional coil designs, it must ideally be possible to integrate with a receive array, which requires that the resonator be detunable. Although one can add a parallel LC tank circuit to the impedance matching network, this does not alter the fact that there is still a tuned resonator. The method investigated involved a simple geometrical arrangement of two wires which shifts the frequency of the HEM mode by tens of MHz if immersed in the water, and ~10 MHz if placed outside the plastic end of the resonator.

One of the potential limitations of the resonator design is that the operating frequency is dictated by only two parameters, namely the size of the resonator and the permittivity of the material used for construction. As such it lacks the inherent flexibility of lumped-element designs in which the use of variable capacitors decouples, to some degree, the resonant frequency from the size of the resonator. Nevertheless, using miscible liquids, it is relatively easy to fine-tune the permittivity of the DR to achieve the desired resonant mode for a particular size of resonator. For a much larger coil, a lower value of permittivity would be required. For example, liquids such as acetone (relative permittivity 20), alcohols (relative permittivities 20–40), and water can be mixed according to simple rules [13] to achieve a given permittivity. While the current demonstration uses water, a practical realization could easily incorporate deuterium oxide to remove the unwanted signal from the coil itself, as also suggested by Wen et al. [17]. Use of high permittivity low loss solid materials would enable smaller resonators to be designed.

The design of DRs is easily extended to higher frequencies and larger coils. Optimization of the exact dimensions/shape/relative permittivity in terms of signal-to-noise and sensitivity is an area in which little research has so far been performed. This general class

of resonators fits into the genre of "leaky waveguides" [6], and share similarities with another coil design suggested for imaging the carotid artery [10]. Given the interplay between resonant conditions and waveguide leakiness it is certainly possible that other geometries can be found which are even more efficient than the one presented here. Mechanistically, it is also possible that "surface waves" [2], which are very familiar from the optical literature, may play a role in the distribution of the RF field throughout the resonator and also, therefore, within the sample.

One area in which this type of resonator may play a role in the future is in the design of PET/MR or SPECT/MR animal and human systems. Although the resonator was fed inductively in the centre of the long-axis in this work, coupling can equally well be performed at the end of the resonator using micro-strips, wave guides, coaxial lines, or dipoles. In terms of the imaging field of view (FOV) the resonator would be completely symmetric, and water results in low attenuation of both PET and SPECT radiation. It is well known that the differential attenuation of spaced conductor structures associated with all conventional RF coil designs cause significant image artefacts in reconstructed nuclear medicine images, and this effect would be eliminated using these types of DRAs.

REFERENCES

[1] G. Adriany, V. de Moortele, F. Wiesinger, S. Moeller, J. P. Strupp, P. Andersen, C. Snyder, X. Zhang, W. Chen, K. P. Pruessmann, et al. Transmit and receive transmission line arrays for 7 tesla parallel imaging. *Magnetic resonance in medicine*, 53(2):434–445, 2005.

[2] V. Agranovich and D. Mills. Surface polaritons: electromagnetic waves at surfaces and interfaces. *Journal of the Optical Society of America B Optical Physics*, 1:410, 1984.

[3] G. Annino, M. Cassettari, I. Longo, M. Martinelli, P. Van Bentum, and E. Van der Horst. A novel probe head for high-field, high-frequency electron paramagnetic resonance. *Review of scientific instruments*, 70(3):1787–1793, 1999.

[4] S. A. Aussenhofer and A. G. Webb. Design and evaluation of a detunable water-based quadrature hem11 mode dielectric resonator as a new type of volume coil for high field mri. *Magnetic Resonance in Medicine*, 68(4):1325–1331, 2012.

[5] K. Haines, T. Neuberger, M. Lanagan, E. Semouchkina, and A. Webb. High q calcium titanate cylindrical dielectric resonators for magnetic resonance microimaging. *Journal of Magnetic Resonance*, 200(2):349–353, 2009.

[6] J. Hu and C. R. Menyuk. Understanding leaky modes: slab waveguide revisited. *Advances in Optics and Photonics*, 1(1):58–106, 2009.

[7] D. Kajfez. *Dielectric Resonators*. INSTITUTION ENGINEERING & TECH, 1998.

[8] D. Kajfez, A. W. Glisson, and J. James. Computed modal field distributions for isolated dielectric resonators. *IEEE transactions on Microwave Theory and Techniques*, 32(12):1609–1616, 1984.

[9] A. Kishk, A. Glisson, and G. Junker. Bandwidth enhancement for split cylindrical dielectric resonator antennas. *Progress In Electromagnetics Research*, 33:97–118, 2001.

[10] W. Koning, J. Bluemink, E. Langenhuizen, A. Raaijmakers, A. Andreychenko, C. den Berg, P. Luijten, J. Zwanenburg, and D. Klomp. High-resolution mri of the carotid arteries using a leaky waveguide transmitter and a high-density receive array at 7 t. *Magnetic Resonance in Medicine*, 69(4):1186–1193, 2013.

[11] G. J. Metzger, C. Snyder, C. Akgun, T. Vaughan, K. Ugurbil, V. de Moortele, et al. Local b1+ shimming for prostate imaging with transceiver arrays at 7t based on subject-dependent transmit phase measurements. *Magnetic Resonance in Medicine*, 59(2):396–409, 2008.

[12] T. Neuberger, V. Tyagi, E. Semouchkina, M. Lanagan, A. Baker, K. Haines, and A. Webb. Design of a ceramic dielectric resonator for nmr microimaging at 14.1 tesla. *Concepts in Magnetic Resonance Part B: Magnetic Resonance Engineering*, 33(2):109–114, 2008.

[13] A. Sihvola. Mixing rules with complex dielectric coefficients. *Subsurface Sensing Technologies and Applications*, 1(4):393–415, 2000.

[14] J. Vaughan, G. Adriany, C. Snyder, J. Tian, T. Thiel, L. Bolinger, H. Liu, L. DelaBarre, and K. Ugurbil. Efficient high-frequency body coil for high-field mri. *Magnetic resonance in medicine*, 52(4):851–859, 2004.

[15] J. T. Vaughan, H. P. Hetherington, J. O. Otu, J. W. Pan, and G. M. Pohost. High frequency volume coils for clinical nmr imaging and spectroscopy. *Magnetic Resonance in Medicine*, 32(2):206–218, 1994.

[16] A. Webb. Visualization and characterization of pure and coupled modes in water-based dielectric resonators on a human 7t scanner. *Journal of Magnetic Resonance*, 216:107–113, 2012.

[17] H. Wen, F. A. Jaffer, T. J. Denison, S. Duewell, A. S. Chesnick, and R. S. Balaban. The evaluation of dielectric resonators containing h 2 o or d 2 o as rf coils for high-field mr imaging and spectroscopy. *Journal of Magnetic Resonance, Series B*, 110(2):117–123, 1996.

[18] V. L. Yarnykh. Actual flip-angle imaging in the pulsed steady state: a method for rapid three-dimensional mapping of the transmitted radiofrequency field. *Magnetic resonance in Medicine*, 57(1):192–200, 2007.

3

HIGH-PERMITTIVITY SOLID CERAMIC RESONATORS FOR HIGH-FIELD HUMAN MRI

Sebastian A. AUSSENHOFER

Andrew G. WEBB

Parts of this chapter have been published in Nuclear magnetic resonance in Biomedicine: **26**, 1555-61 (2013) [1].

The properties of a ceramic-based annular dielectric resonator designed for 7 T MRI have been examined. Electromagnetic simulations and experimentally determined modal frequencies agree to within 1%. The dependence of the resonance frequency of the degenerate quadrature HEM_{11} modes on hole diameter and shield diameter was also investigated. The constructed coil, with a 2.5 cm diameter hole, had an unloaded Q value of 400, which was reduced to 150 when loaded with a human finger. Simulated and experimental B_1^+ maps show a high degree of homogeneity with a sensitivity of $\sim 11.5\ \mu T/\sqrt{W}$ at the centre. A comparison with a loop gap resonator showed an approximately 25% higher sensitivity for the dielectric resonator. High-resolution images of the digital interphalangeal (DIP) and proximal interphalangeal (PIP) joints of volunteers were acquired in imaging times of less than 2 min. Finally, novel methods of double tuning such ceramic resonators to two relatively close frequencies, e.g. proton and fluorine, have been shown.

3.1. INTRODUCTION

THE majority of RF coils for MRI are constructed from electrically conductive elements, usually consisting of copper or silver-coated copper. A potential alternative is to use high-permittivity, low-loss ceramic materials (either as the coil itself or as an insert), as has been shown in a few resonator designs for electron paramagnetic resonance [2], [3] and MR imaging and spectroscopy [4], [5], [6], [7], [8], [9] and [10]. Several different spatially variant electromagnetic modes of magnetic field storage exist for different geometries of the high-permittivity material. The most common geometry is an annulus into which the sample is placed, although arrangements of two disks with a small gap between have also been demonstrated [5]. For the majority of these resonators, the transverse electric (TE_{01}) mode has been used. This is the lowest-frequency mode, but for MR applications has the disadvantage that it is only a linear mode (thus cannot be driven in quadrature), and that the B_1 field lies along the axial dimension of the cylinder, thus making it somewhat disadvantageous for realistic in vivo applications as the coil has to be rotated through 90° perpendicular to the B_0 field [10]. The first practical RF resonator operating in a circularly polarized degenerate hybrid electromagnetic mode (HEM_{11}) was designed with water as the high-permittivity material, and was used to image the human wrist on a 7 T whole-body scanner [11]. One of the major advantages of the resonator was its very easy construction from readily available materials. However, water is a relatively lossy dielectric even at radio frequencies, gives a large background signal (although it can easily be replaced by deuterium oxide), and the relative permittivity of only 80 means that resonators can become quite large.

In this paper the properties and design of a solid, high-permittivity, low-loss ceramic HEM_{11}-mode resonator are described. The resonator is an annular design constructed from barium strontium titanate (BST). This material is based on the most most common high-permittivity material, barium titanate, which is doped with strontium. Doping reduces the Curie temperature (TC) of BST compared with barium titanate, with the result that BST has significantly lower loss than barium titanate, but also a lower relative permittivity (11). The exact value of the permittivity is highly dependent on grain size, generally increasing with decreasing grain size up to the sub-micron range. Commercially available barium titanate has a real component of the permittivity ~1400 with loss tangents ~0.05. Typical values for BST are 150–200 and 0.01, respectively.

The dimensions of the resonator are designed so that high- resolution imaging of human digits (for studies of rheumatoid arthritis) can be acquired with the resonator

having appropriate dimensions for a high filling factor and patient comfort. Extensive resonator characterization is performed, with experimental and simulation results compared. High-resolution in vivo images are acquired showing fine detail, in particular, of the cartilage structure in the finger. Finally, it is shown that one can take advantage of the independence of the single TE and two HEM modes to produce double-tuned probe designs for nuclei such as protons and fluorine whose gyromagnetic ratios are similar.

3.2. EXPERIMENT

3.2.1. HIGH-PERMITTIVITY CERAMIC MATERIALS

BARIUM strontium titanate cylinders with a relative permittivity ~175 (product K-175) and loss tangent less than 0.01 were purchased from TCI Ceramics/National Magnetics Group. The HEM_{11} mode frequency is given by [12]

$$f_{HEM_{11\delta}} = 2.735\frac{c\epsilon_r^{-0.436}}{2\pi a}\left[0.543 + 0.589\frac{a}{h} - 0.05\left(\frac{a}{h}\right)^2\right] \tag{3.1}$$

where c is the speed of light, ϵ_r the relative permittivity, a the radius and h the height of the resonator. Since a hole has to be drilled in the cylinder and a shield placed around the ceramic to reduce radiation losses, and both of these increase the resonant frequency, the diameter was chosen to be less than would be predicted from Equation3.1. Given that the coil was intended to image the finger, a height of at least 6 cm was required, and an inner annular diameter of at least 2.5 cm. Electromagnetic simulations (see below) were used to determine the final height and diameter of the ceramic disk as 6.3 cm and 8.6 cm, respectively, with a 2.5 cm hole in the centre. Ultrasonic-mediated milling was used to produce the central hole in the resonator.

3.2.2. ELETROMAGNETIC SIMULATIONS

Electromagnetic (EM) simulations of the magnetic field distributions for both the cylindrical (i.e. before drilling) and annular HEM resonators were performed using an eigenmode solver (CST Microwave Studio, Darmstadt, Germany). A tetrahedral mesh with 58 264 elements was created using the Delaunay meshing algorithm, with the maximum curved element order of six. Twenty modes were searched for above a frequency of 200 MHz, with an accuracy of 1×10^6, and a second-order convergence criterion. Two-dimensional vector plots were obtained to identify the particular mode based on known distributions of magnetic and electric fields [13]. The magnetic and electric fields are in quadrature, with the maximum values of the electric fields occurring at a phase of 0° and magnetic fields at 90°.

3.2.3. ELECTRICAL CHARACTERIZATION

Modal frequencies were measured using an unmatched, 1 cm diameter shielded loop constructed from semi-rigid 50 Ω coaxial cable (Microstock, West Point, PA). The loop was placed above the centre of the ceramic disc to detect primarily TE modes, and at the side of the resonator at half-height to detect HEM modes. For the HEM resonator standard inductive coupling loops [11] were used for impedance matching, with variable

capacitors for fine adjustment for different loads. For the impedance-matched resonator S_{11} measurements were performed for each quadrature channel, and an S_{12} measurement to determine the orthogonality of the modes. In order to characterize the loading effects on the coil, a saline phantom made of a plastic tube of 24 mm outer diameter and a length of 120 mm, with salt added to give a conductivity of 0.47 S/m, was used. This phantom was also used to produce B_1^+ maps.

3.2.4. MRI EXPERIMENTS

All imaging and B_1^+ mapping experiments were conducted on a 7 T whole-body human MRI scanner (Philips Achieva, Best, The Netherlands) using a dual TR method [14]. A three-dimensional gradient echo sequence was used with the following parameters: field of view $160 \times 160 \times 160$ mm^3, voxel resolution $2.5 \times 2.5 \times 2.5$ mm^3, TR_1/TR_2 30/150 ms, TE 1.5 ms, nominal 45° tip angle at the centre of the phantom. The coil sensitivity was calculated as the B_1^+ per square root watt of input power, with the power estimated from the output power of the RF amplifier taking into account measured power loss in the cables from the amplifier to the coil.

For imaging the finger, after acquiring short scout scans to determine the appropriate field of view, a three-dimensional gradient echo sequence was acquired with the following parameters: TR/TE 10 ms/5 ms, tip angle 10°, field of view $50 \times 100 \times 25$ mm^3, data acquisition matrix $332 \times 340 \times 50$ (zero-filled to $800 \times 800 \times 50$ for image display), spatial resolution $0.15 \times 0.3 \times 0.5$ mm^3, total image acquisition time 86 s. The study adhered to the LUMC Institutional Review Boardguidelines and informed consent was obtained from volunteers prior to the study.

3.2.5. REFERENCE RESONATOR

In order to compare the performance of the dielectric resonator design with a conventional design, a loop gap resonator [15] was built. An inner diameter of 2.5 cm was chosen to allow imaging the same phantom as for the ceramic resonator. The length was ~6 cm, and the loop was constructed from 25 μm thick copper foil (3M, St. Paul, Minnesota) shaped around a custom-produced plastic cylinder with a thickness of 1 mm. A conventional capacitive pi-network was used for impedance matching.

3.3. RESULTS

3.3.1. ELECTROMAGNETIC SIMULATIONS AND ELECTRICAL CHARACTERIZATION

THE properties of the resonator were investigated using a simple unmatched 1 cm diameter shielded pick-up loop. Figure 3.1 shows network analyser plots for the solid resonator, annular resonator with no load, and annular resonator with a tissue-mimicking load. Table **??** shows a comparison between the simulated and measured frequencies of the first five modes. Based upon the mode behaviour with respect to the pick-up loop geometry and position, known modal patterns of the magnetic field distribution [13] and previous MRI-confirmed modal assignations [16], the modes can easily be assigned. The degenerate HEM mode has a well characterized magnetic and electric field distribution [11],[13], with a maximum in the magnetic field and zero electric field at the centre of the resonator. In general, a displacement of the electric and magnetic fields affects the resonant frequency, and its direction of change can be determined from cavity perturbation theory [17],[18].

$$\frac{\omega-\omega_0}{\omega_0} \approx \frac{\int\int\int_{\triangle\nu}\left(\mu|H_0^2|-\epsilon|E_0^2|\right)\partial\nu}{\int\int\int_{\nu}\left(\mu|H_0^2|+\epsilon|E_0^2|\right)\partial\nu} \tag{3.2}$$

where the numerator represents the difference of stored magnetic and electric energy within the volume $\triangle\nu$ and the denominator is the total energy stored within the volume v. Since ϵ is much larger than μ, the dominant factor is the displacement of the electric field. Drilling a hole in the centre of the resonator will have the smallest effect on the frequency of the TE_{011} mode and the largest effect on the TM_{011} mode, as shown in Table 3.1, since the TE mode has zero electric field, whereas the TM mode has its maximum electric field, along the central axis of the cylinder. In terms of an outer shield, if the stored energy outside the resonator is mostly electric, moving a metal shielding wall closer to the resonator will decrease the resonant frequency. Conversely, for a displaced field that is predominantly magnetic, the resonant frequency will increase. The small increases in frequency of the two TE and two HEM modes shows that a fraction of the magnetic energy is indeed stored outside the resonator.

Mode	Solid simulated	Solid experiment	Annular (2.5 cm hole) simulated	Annular (2.5 cm hole) experiment	Annular + shield simulated	Annular + shield experiment
TE_{011}	251.1	251.4	253.3	251.5	269.4	272.2
HEM_{11}	271.3	271.4	296.3	292.5	301.6	301.1
HEM_{12}	350.4	349.0	361.5	362.0	373.2	375.9
TE_{012}	357.4	356.3	368.6	370.9	365.7	366.6
TM_{011}	362.7	362.3	421.8	426.7	419.8	422.1

Table 3.1: Modes simulated and measured.

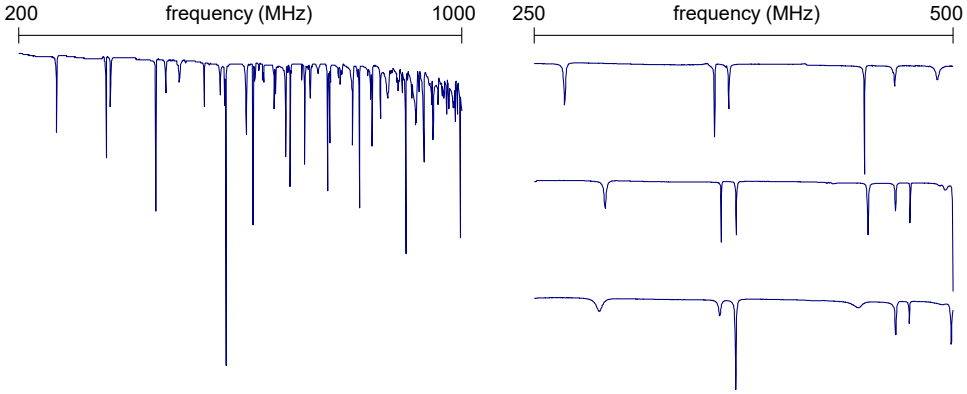


Figure 3.1: (Left) S_{11} plot from a small (1 cm diameter) unmatched pick-up loop placed to the side of the ceramic cylinder at its half-height. A large number of different modes can be detected. (Right) Expanded view of the 250–500 MHz range with the HEM_{11} mode at the lowest frequency: top – full cylinder; centre – cylinder with an empty 2.5 cm diameter hole drilled in the centre; bottom – a human finger is positioned inside the hole

Figure 3.2 shows simulated changes in the resonance frequency for different hole diameters in an unshielded HEM resonator, and for different shield diameters for an HEM resonator with a 2.5 cm diameter hole filled with tissue. Two inductively coupled impedance matching networks were placed at the centre of the long axis of the resonator at a distance of 1.2 cm from the outside surface of the resonator, 90° apart from each other: the topology of the coupling loops is shown in Figure 3.3. The variable capacitors allow fine-tuning for different loads. Figure 3.4 shows a photograph of the assembled HEM resonator. A PMMA cylinder (height 8 cm, inner diameter 14 cm, wall-thickness 9 mm) was used to form a closed annulus centring the ceramic cylinder while allowing access to the bore of the resonator. Inside the PMMA cylinder 25 μm thick copper foil (3M) was glued to form a shield. The coil was interfaced to the scanner by using 40 cm

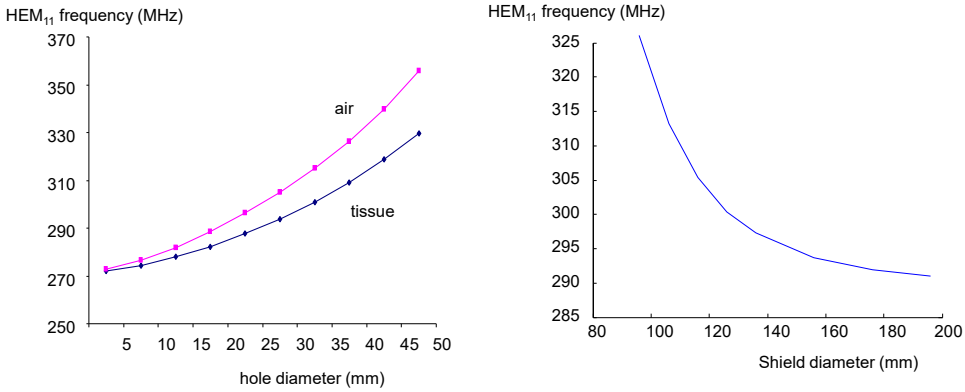


Figure 3.2: (Left) Plot of simulated HEM_{11} frequency versus the diameter of the hole drilled through the centre of the resonator with the hole filled with either air or tissue. (Right) For a resonator with a 25 mm diameter hole filled with tissue, a plot of the HEM_{11} frequency versus diameter of a thin copper shield with height equal to that of the resonator.

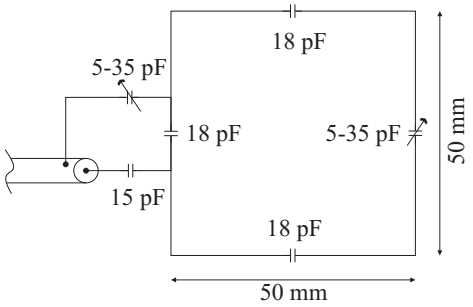


Figure 3.3: Topology of the coupling loop and matching network for the ceramic resonator.

long double-shielded 50 Ω coaxial cables (K 02252, Huber & Suhner, Switzerland). The resonator was matched to 298.1 MHz when loaded with a human finger and each channel achieved an S_{11} of less than –20 dB. The S_{21} between channels was also less than –20 dB. The effect of placing the finger inside the resonator is also shown in Figure 3.4. There is a significant reduction in the Q value of the resonator from 400 in the unloaded case to 150 when the resonator is loaded, with an ~3 MHz decrease in the resonance frequency.

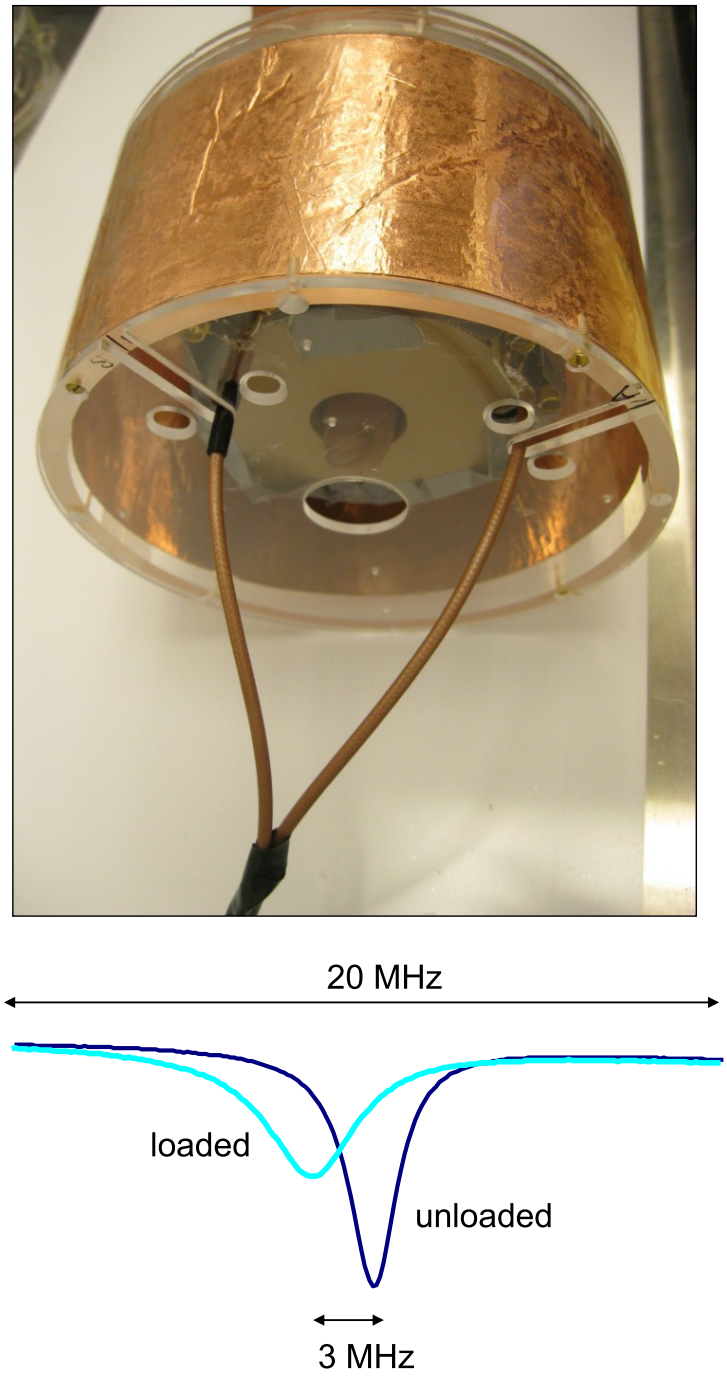


Figure 3.4: (Left) Photograph of the shielded quadrature HEM_{11} resonator with coaxial cables feeding the two orthogonal matching networks. (Right) Effect of loading the resonator with a human finger.

3.3.2. PHANTOM MRI MEASUREMENTS

Experimentally acquired B_1^+ maps from the dielectric resonator are shown in Figure 3.5, depicting relatively homogeneous fields in both the transverse and longitudinal directions. As a measure of the transmit field efficiency, the B_1^+ field at the centre of the phantom was determined to be ~11.5 μT per $\sqrt{W}$ of power delivered to the coil. The acquired B_1^+ maps correspond well to the simulated data also shown in Figure 3.5. For the comparison loop-gap resonator, the B_1^+ field at the centre was measured to be ~8.2 $\mu\text{T}/\sqrt{W}$.

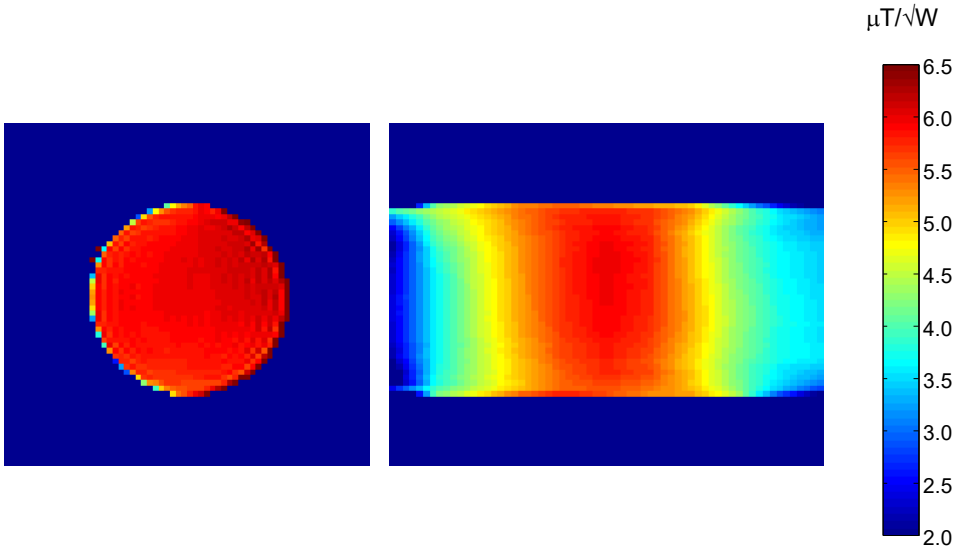


Figure 3.5: (Left) Transverse and coronal B_1^+ maps obtained using a saline phantom in the HEM resonator. (Right) Corresponding B_1^+ maps obtained using electromagnetic simulations. The axial extent of the B_1^+ field greater than 50% of its maximum at the centre is ~5 cm.

3.3.3. IN VIVO MRI EXPERIMENTS

Figure 3.6 shows results obtained from a healthy volunteer with the second digit of the right hand. The volunteer is positioned on the side with the hand placed slightly higher than the head, with the coil firmly held in place at the centre of the magnet. Insertion of every single digit is possible, with the remaining digits resting against the flat bottom of the coil. Best patient comfort occurs if the hand is supported with sandbags or other support materials. The aim is to study mainly the digital interphalangeal (DIP) and proximal interphalangeal (MIP) joints, so the finger does not have to be pushed into the coil to a full and uncomfortable extent. This situation can be favourably compared with conventional scans on 1.5 or 3 T systems in which the body coil is used for excitation, and the coil is placed over the entire wrist with the palm facing the upper part of the femur. The fingers are therefore in a sub-optimal position very close to the coil and gradients, and the specific absorption ratio (SAR)in this configuration is particularly high in body parts such as the arms and hands adjacent to the magnet bore. The images in Figure 6 are acquired at a spatial resolution of $0.15 \times 0.3 \times 0.5$ mm^3,significantly higher than at lower fields, and in a very short imaging time of ~1.5 min. The images show fine structure within the trabecular bone and the cartilage. Higher resolutions are of course possible with longer scanning times.

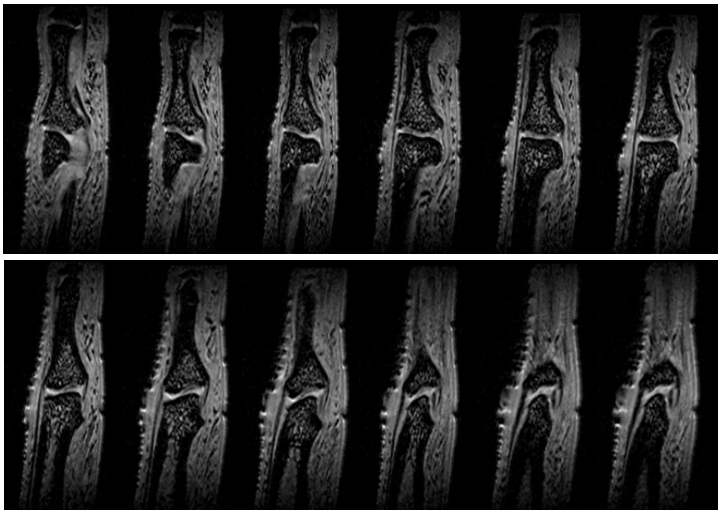


Figure 3.6: Images from a three-dimensional gradient echo sequence of the forefinger of the hand of a healthy volunteer. The spatial resolution is $0.15 \times 0.3 \times 0.5$ mm^3 and the images are acquired in ~1.5 min. The images show the fine resolution in the trabecular bone and cartilage structures.

3.4. DISCUSSION

THIS paper has described the properties of a high-permittivity ceramic cylindrical resonator, and the design of an annular HEM_{11} resonator based upon this material. Electromagnetic simulations have been shown to correspond well to experimental measurements in terms of resonance frequencies, and the effects on these frequencies of a central hole and an outer RF shield. Therefore, resonators using different materials and with different geometries can be designed with a high degree of accuracy through simulations before the highly specialized process of ceramic production is initiated. The in vivo images acquired of the human finger show a high degree of RF homogeneity, and very high spatial resolution can be achieved in a relatively short imaging time.

One question is how large the hole diameter can be before the coil performance degrades severely. As the hole diameter increases, the B_1 field in the centre of the resonator becomes lower. Figure 3.7 shows plots of the magnetic field as a function of hole diameter, with the hole filled with tissue. The B_1 field can be seen to "spread out", but even for diameters which are about one-third of the diameter of the resonator itself the B_1 field maintains a reasonably homogeneous distribution. In the case of the 30 mm hole diameter, the B_1 field at the centre of the resonator is approximately 80% that of the resonator with no hole. Maintenance of the essential mode depends upon the electric field distribution not being disturbed significantly by the presence of a central hole. Since the electric field is zero at the centre for the HEM_{11} mode, increasing radially outwards, a hole diameter up to ~20 mm has minimal effect on the E-field distribution and strength, and therefore also on the magnetic field. However, when the hole "cuts into" volumes where the E-field is significant, then the mode becomes less effective, and the magnetic field much smaller, as is seen when the hole diameter increases to 30 mm.

In terms of building larger coils, what this implies is that one would move to a larger outer diameter for a given inner diameter, or use a material with a lower permittivity so that a larger resonator could be constructed. In this case the sample would have a more similar permittivity to the coil material, thus preserving essentially an undisturbed resonator. This can be seen in a previous paper on HEM mode resonators, in which water was the dielectric (with a permittivity very close to tissue) and the inner diameter of the hole can be made much larger [11].

One interesting aspect of these resonators is that the effects of shielding on the resonance frequency can potentially be used to create a double-tuned resonator for closely

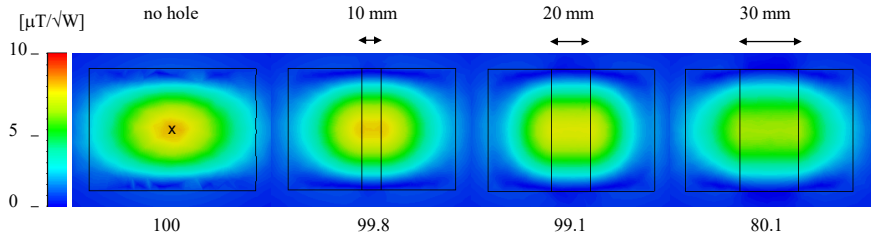


Figure 3.7: Electromagnetic simulations of the B_1^+ field in the HEM resonator as a function of hole diameter, with the hole filled with tissue. The numbers refer to the percentage of the B_1^+ field measured at the centre point (x) of the resonator with no hole present. When the hole diameter reaches 30 mm, the maximum B_1^+ field is no longer at the centre of the resonator, but at the edge of the inner hole, which explains the relatively large drop in value.

spaced frequencies such as fluorine (resonant frequency 280.4 MHz at 7 T) and protons, without the need for lumped element trap-circuits. Two possibilities are shown in Figure 3.8.

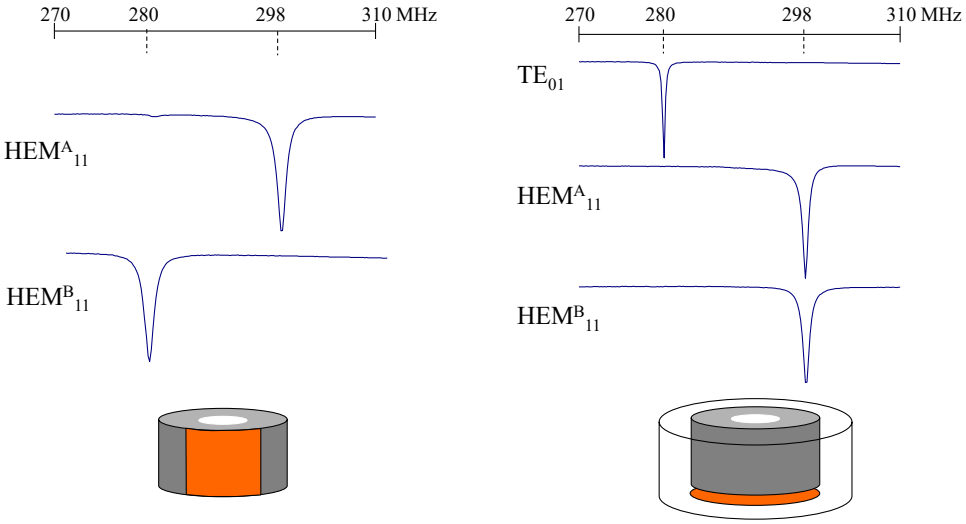


Figure 3.8: Two methods of double-tuning the ceramic resonator to proton (298 MHz) and fluorine (280 MHz) resonant frequencies at 7 T. On the left a partial (~90° coverage) shield shifts one of the HEM modes (denoted HEM^A) up to 298 MHz while the other mode (denoted HEM^B) is unaffected. On the right, an additional shield placed below the resonator shifts the TE mode from 251 MHz to 280 MHz while the two orthogonal HEM modes remain at 298 MHz.

On the left, a close shield, which subtends an angle of ~90°, shifts the frequency of one of the HEM modes upwards, but does not affect the orthogonal mode. The two network

analyser plots acquired with a pick-up loop oriented opposite the shield (detecting the mode denoted HEM^A) and at 90° to the shield (detecting the mode denoted HEM^B) show resonant frequencies at 298 and 280 MHz, respectively. Of course, one disadvantage of this approach is that only linear mode operation is possible for both frequencies. A second possibility, shown on the right in Figure 3.8, is to tune the TE_{01} mode to the fluorine frequency by using a shield on the bottom of the resonator, with the HEM modes largely unaffected by this shielding. Operation of this coil would involve rotation by 90° between using the quadrature HEM modes and the linear TE mode, but this design could be useful for imaging, for example, ex vivo tissue in which coil reorientation between scans is not a problem. Alternatively, one of the proton HEM modes could be used with the proton TE mode without the need for coil reorientation.

3.5. CONCLUSION

THIS work shows that high-permittivity material resonators are feasible for high-field MRI. Due to the material properties it is possible to build compact resonators with good B_1 field homogeneity. Design equations given in the literature allow construction of annular resonators with the aid of electromagnetic simulation software. The possibility to fine-tune the resonators with copper shields also eases the demands on very accurate manufacturing of the resonators. These resonators can also be used for smaller animal MR scanners, where even higher operational frequencies would allow still more compact designs.

REFERENCES

[1] S. Aussenhofer and A. Webb, *High-permittivity solid ceramic resonators for high-field human mri,* NMR in Biomedicine **26**, 1555 (2013).

[2] G. Annino, M. Cassettari, I. Longo, M. Martinelli, P. Van Bentum, and E. Van der Horst, *A novel probe head for high-field, high-frequency electron paramagnetic resonance,* Review of scientific instruments **70**, 1787 (1999).

[3] G. Annino, M. Cassettari, M. Martinelli, and P. Van Bentum, *A nonradiative approach to single-mode dielectric resonators,* Applied Magnetic Resonance **24**, 157 (2003).

[4] K. Haines, T. Neuberger, M. Lanagan, E. Semouchkina, and A. Webb, *High q calcium titanate cylindrical dielectric resonators for magnetic resonance microimaging,* Journal of Magnetic Resonance **200**, 349 (2009).

[5] T. Neuberger, V. Tyagi, E. Semouchkina, M. Lanagan, A. Baker, K. Haines, and A. Webb, *Design of a ceramic dielectric resonator for nmr microimaging at 14.1 tesla,* Concepts in Magnetic Resonance Part B: Magnetic Resonance Engineering **33**, 109 (2008).

[6] P. Daleiden, M.-A. Golombeck, S. Junge, and O. Dössel, *Development and characterisation of a ceramic hf-resonator for the mr-tomography,* Biomedizinische Technik/Biomedical Engineering **47**, 758 (2002).

[7] E. Eriksen, M.-A. Golombeck, S. Junge, and O. Dössel, *Simulation of a birdcage and a ceramic cavity hf-resonator for high magnetic fields in magnetic resonance imaging,* Biomedizinische Technik/Biomedical Engineering **47**, 754 (2002).

[8] S. M. Mattar and S. Y. ElNaggar, *Analysis of two stacked cylindrical dielectric resonators in a te 102 microwave cavity for magnetic resonance spectroscopy,* Journal of Magnetic Resonance **209**, 174 (2011).

[9] A. Neufeld, N. Landsberg, and A. Boag, *Dielectric inserts for sensitivity and rf magnetic field enhancement in nmr volume coils,* Journal of Magnetic Resonance **200**, 49 (2009).

[10] H. Wen, F. A. Jaffer, T. J. Denison, S. Duewell, A. S. Chesnick, and R. S. Balaban, *The evaluation of dielectric resonators containing h 2 o or d 2 o as rf coils for high-field mr imaging and spectroscopy,* Journal of Magnetic Resonance, Series B **110**, 117 (1996).

[11] S. A. Aussenhofer and A. G. Webb, *Design and evaluation of a detunable water-based quadrature hem11 mode dielectric resonator as a new type of volume coil for high field mri,* Magnetic Resonance in Medicine **68**, 1325 (2012).

[12] A. Kishk, A. Glisson, and G. Junker, *Bandwidth enhancement for split cylindrical dielectric resonator antennas,* Progress In Electromagnetics Research **33**, 97 (2001).

[13] D. Kajfez, A. W. Glisson, and J. James, *Computed modal field distributions for isolated dielectric resonators,* IEEE transactions on Microwave Theory and Techniques **32**, 1609 (1984).

[14] V. L. Yarnykh, *Actual flip-angle imaging in the pulsed steady state: a method for rapid three-dimensional mapping of the transmitted radiofrequency field,* Magnetic resonance in Medicine **57**, 192 (2007).

[15] W. Froncisz and J. S. Hyde, *The loop-gap resonator: a new microwave lumped circuit esr sample structure,* Journal of Magnetic Resonance (1969) **47**, 515 (1982).

[16] A. Webb, *Visualization and characterization of pure and coupled modes in water-based dielectric resonators on a human 7t scanner,* Journal of Magnetic Resonance **216**, 107 (2012).

[17] M. Jaworski and M. W. Pospieszalski, *An accurate solution of the cylindrical dielectric resonator problem,* Microwave Theory and Techniques, IEEE Transactions on **27**, 639 (1979).

[18] F. S and A. JELENSKI, *Influence of conducting walls on resonant frequencies of dielectric microwave resonator,* (1971).

4

AN EIGHT-CHANNEL TRANSMIT/RECEIVE ARRAY OF TE_{01} MODE HIGH PERMITTIVITY CERAMIC RESONATORS FOR HUMAN IMAGING AT 7.0 TESLA.

Sebastian A. AUSSENHOFER

Andrew G. WEBB

Parts of this chapter have been published in Magnetic resonance in medicine: official journal of the Society of Magnetic Resonance in Medicine **68**, 1325-31 (2012) [2].

4

This study describes the design, construction and operation of a new type of transmit/receive array using ceramic resonators operating in a transverse electromagnetic (TE) mode. Single element function and performance at 298.1MHz (7.0 Tesla) are analyzed and compared to a lumped element design loop coil with comparable geometry. The results show that ceramic resonators working in the $TE_{01\delta}$ mode configuration produce similar efficiency, defined as the transmit magnetic field B_1^+ per square root of the specific absorption rate (SAR), to conventional surface coils. An array consisting of eight ceramic elements was then designed to operate in transmit/receive mode. This array was driven via power/phase splitters by two independent transmit channels and functional cardiac images were produced from a number of healthy volunteers.

4.1. INTRODUCTION

DUE to the intrinsic wavelength effects at very high frequency (VHF), and the lack of a homogenous excitation source such as the body coil on 3 T systems, resonator design for VHF-MR body imaging requires transmit or transceiver arrays. A variety of different designs have been suggested, including microstrip elements [11, 15, 20], radiative antennas [13], and loop coils [4, 5, 17]. Sophisticated arrays of up to 32 elements have been produced, and the quality of body images at 7.0 T and above continues to improve. Nevertheless,there is currently no general consensus on the best type of resonator to use, and the area remains open to new types of design.

An alternative design, explored here for the first time, is to use dielectric resonator antennas (DRAs) made from very high permittivity materials. The concepts of both resonant [1, 2, 8] and non-resonant [10] high-permittivity structures have been used in recent high field design. Following initial work by Wen et al. [24], it has been shown that numerous modes of a resonant cavity can, in principle, be used for imaging [23]. In this current work we investigate a new application of cylindrical DRAs made from high permittivity, low loss ceramics for forming a transceiver array for body imaging at 7 T. These are designed to operate in the $TE_{01\delta}$ mode [8, 23, 24]. Their performance is compared to that of an identically-sized segmented loop coil in terms of magnetic and electric field distributions, and transmit efficiency. In addition to electromagnetic (EM) simulations and phantom experiments, preliminary experiments using an eight-element transmit/receive array have been performed in cardiac imaging, since this forms one of the major applications at high field [4–6, 12, 14, 17–22, 25]. As has been pointed out by Niendorf et al. [12] the promise of enhanced relative spatial resolution could enable new myocardial tissue characterization as well as micro-structural investigation.

4.2. MATERIALS AND METHODS

4.2.1. DESIGN OF INDIVIDUAL CERAMIC RESONATORS

In order to design a ceramic disk whose $TE_{01\delta}$ mode is resonant at 298 MHz calculations of appropriate dimensions and dielectric constant were carried out using the formula published by Kajfez and Gullion [9]:

$$f_{TE_{01\delta}} = 2.921 \frac{c\epsilon_r^{-0.465}}{2\pi a}\left[0.691 + 0.319\frac{a}{h} - 0.035\left(\frac{a}{h}\right)^2\right] \tag{4.1}$$

where $f_{TE01\delta}$ is the frequency of the $TE_{01\delta}$ mode in MHz, a the radius and h the height of the resonator (both in cm), c the speed of light and ϵ_r the relative permittivity. While this formula gives a good starting point, detailed EM simulations (see below) were carried out to refine the structure before production. A set of $BaSrTiO_3$ resonators with a relative permittivity of 165, designed to be shielded on top with a copper disk, was obtained from TCI Ceramics Inc. (Bethlehem, PA). A height of 39 mm and radius of 43 mm resulted in a resonance frequency of the TE_{01} mode at 270 MHz, which could then be fine tuned to 298 MHz by changing the distance between the coplanar copper shield and the resonator. A photograph of a single resonator is shown in Fig. 4.1(a).

For impedance matching and coupling energy into the ceramic resonator, inductive coupling via a small non-resonant coupling loop was used as shown in Fig. 4.1(b and c). Since large coupling loops would change the boundary condition on the coupling plane of the resonator the coupling loops were designed to be only 35 mm in outer diameter with a track thickness of 2 mm, etched on FR4 PC board The loops were place concentrically on the top side of the ceramic resonators as shown in Fig. 4.1(b) for maximum coupling to the TE mode. The loop was tuned to ~250 MHz by adjusting a variable capacitor (Voltronics, Salisbury, MD). A capacitive matching network consisting of two fixed capacitors (American Technical Ceramics, Huntington Station, NY) was adjusted to obtain critical coupling when loaded with the human body.

The eight element transmit/receive array design consisted of an anterior and posterior section, each comprising four individual housings, one for each element (Fig. 4.1(d)), that were manufactured on a 3D rapid prototyping machine (3D Touch, BitsfromBytes LCC). The position of the anterior elements can be altered with respect to one another, but the four resonators on the posterior side are fixed in place, as shown in Fig. 4.1(e).

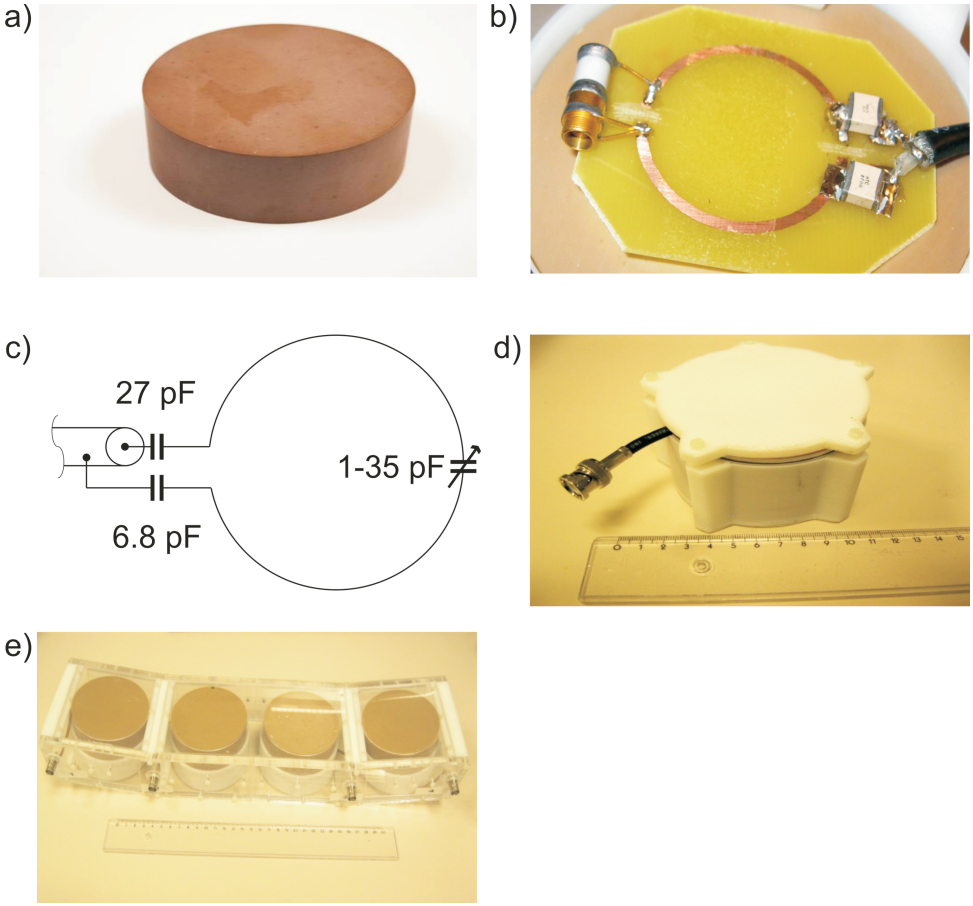


Figure 4.1: (a) shows a single ceramic resonator designed for TE_{01} mode excitation at 298 MHz made from $BaSrTiO_3$. The dimensions are diameter 86 mm and a height of 39 mm with a relative permittivity of 165. (b) Shows the coupling circuit etched on FR4 located on top of a ceramic resonator for impedance matching. (c) Shows the schematic for the coupling loops used for impedance matching. (d) Shows a single anterior element in a custom-built acrylonitrile butadiene styrene (ABS) housing that has a shield integrated into the top section. (e) Shows the posterior elements packed together into a conformal housing made from ABS and acrylic sheets.

4.2.2. REFERENCE LOOP COIL

In order to evaluate the performance of the TE_{01} mode resonators a circular loop coil was constructed for comparison. The coil had the same outer diameter of 8.6 cm with a track thickness of 5 mm and was split into eight segments of equal length. Eight capacitors (15 pF each) were distributed equally in the segment gaps in order to resonate the loop at 298 MHz. A conventional capacitive π-network was used for impedance matching.

4.2.3. ELECTROMAGNETIC SIMULATIONS

Simulations were performed with CST Microwave Studio version 2012 (CST AG, Darmstadt, Germany) on a workstation equipped with two Intel Xeon X5660 central processing units, 48 gigabytes of random access memory and two Nvidia Tesla C1060 graphic processing units (GPUs). Each simulation was set up with 20 lines per wavelength, a lower mesh limit of 10 and a mesh line ratio limit of 50 leading to a total of 47 million mesh cells. A full simulation took about 12 h to run with GPU acceleration computing. After the FDTD simulation all devices were matched to 50 Ω in the circuit simulator, and the fields were recalculated to take the matching into account. All simulations reached a convergence of ~50 dB: the ceramic resonators needed more simulation cycles than the loop coil due to the low loss of the ceramic substrate.

For phantom simulations the loop coil and the shielded ceramic resonator were placed on top of a cubic phantom with an edge length of 200 mm, relative permittivity of 78 and a conductivity of 0.5 Sm. Two distances (3 and 13 mm) between the bottom of the resonator and the phantom were evaluated. The reason to include two distances is that the dielectric resonator is ideally placed as close to the body as possible, whereas the loop coil (with its strong electric fields close to the segmenting capacitors) should be placed a small distance away from the body. An overview of the simulation setup for the single elements is given in Fig. 4.2. Lumped element losses were not included, which may lead to a slight overestimation of the efficiency of the loop coils.

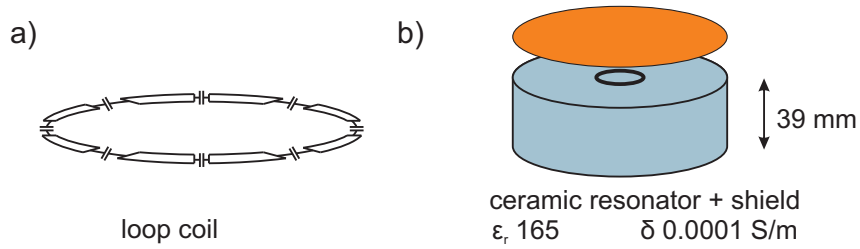


Figure 4.2: Setup of the single elements for the simulation. (a) Shows the surface loop coil capacitively segmented 8 times, (b) shows a ceramic resonator with a height of 39 mm height and a copper shield that is lowered towards the resonator until the TE_{01} mode is at 298 MHz.

Whole body simulations were performed on the virtual family member Gustav [3] positioned inside a metallic tube mimicking the bore of the 7 T MRI system. Eight dielectric resonators were placed anterior (four) and posterior (four) around the chest to evaluate the performance of the array in terms of B_1^+ transmit field and specific absorption rate (SAR). The position of the individual array elements on the chest of Gustav is given in Fig. 4.3. The same positions were used for simulations of both the DRAs and the loop coils.

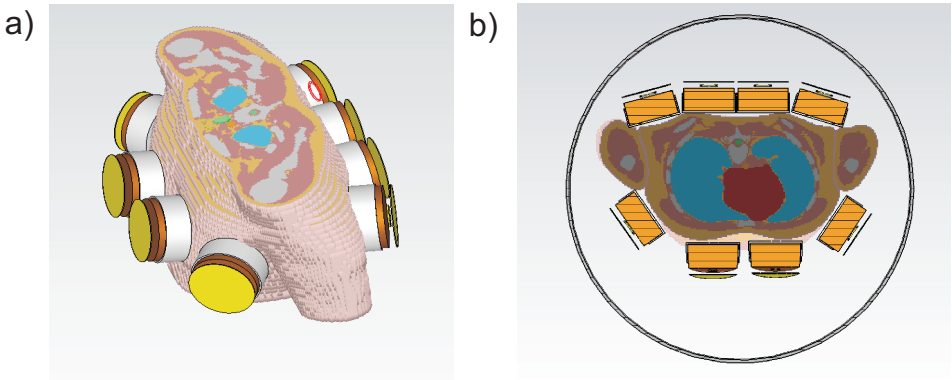


Figure 4.3: Positioning of the elements on the chest of the virtual family member Gustav. For the loop coil simulations the individual loop elements were placed concentric in plastic spacers with their bottom side coincident with the bottom part of the spacer.

4.2.4. HARDWARE SETUP AND CHARACTERIZATION

The Philips system is only equipped with two independent transmit channels, rather than the eight (or more) offered by other vendors. Each of the two channels was split into four channels with homebuilt power splitters (microstrip Wilkinson design) and fed through a homebuilt transmit/receive switch box. The insertion loss through the transmit chain was about 4.2 dB from amplifier to the single coil elements (~2.2 dB in terms of cable loss from RF amplifiers to the coil, and ~2.0 dB loss in the custom-built transmit/receive switches). In order to determine optimal (given the limitations of only two independent channels) phase differences between the upper four and lower four elements of the array, scout images were acquired with 0°, 90°,180° and 270° phase difference. These images were inspected to see which setting gave the least degree of signal voids (usually present as a distinct black band) through the heart. Much more sophisticated B_1-shimming algorithms exist on other commercial systems, but in this case our work was constrained by system hardware limitations. Different optimal phase settings were found for different subjects.

4.2.5. MRI ACQUISITION PROTOCOL AND PARAMETERS

The study adhered to the Leiden University Medical Center Institutional Review Board guidelines and informed consent was obtained from volunteers (N = 14) prior to the study. Phantom experiments used a large rectangular (360 × 200 × 180 mm) container filled with tissue-mimicking material (dielectric constant ~79 and conductivity ~0.5 S/m). B_1^+ mapping was performed using a dual TR method. In vivo experiments were conducted on a 7 T whole-body human scanner (Philips Achieva, Best, The Netherlands). Data obtained from the fourteen healthy volunteers, both male and female (seven each), used a cine sequence during consecutive breath-holds. The volunteers had a mean body mass index of 23.6 ± 7 and mean heart rate of 69 ± 10 beats per minute. Short axis views were obtained with the following parameters: retrospectively EKG triggered turbo field echo sequence with a field-of-view 300 mm (foot–head) × 295 mm (right–left) ×8 mm (anterior–posterior), spatial resolution 1.39 × 1.44 × 8 mm, TR/TE 4.0/2.5 ms, 33 cardiac phases, one breath-hold time 13.4 s per slice, thirteen slices, flip angle 8.5° and an average RF power of 23.5 W. The four-chamber view was acquired with the following parameters: retrospectively EKG triggered turbo field echo sequence with a field-of-view 380 mm (right–left) × 275 mm (anterior–posterior), spatial resolution 1.3 × 1.35 × 8 mm, single slice, TR/TE 4.23/ 2.5 ms, 33 cardiac phases, flip angle 8.5 degrees and an average RF power of 22.4 W. The two chamber view was obtained with the following parameters:

retrospectively EKG triggered turbo field echo sequence with a field-of-view 380 mm (right–left) × 275 mm (anterior–posterior), spatial resolution 1.3 × 1.35 × 8 mm, single slice, TR/TE 4.1/2.1 ms, 33 cardiac phases, flip angle 8.5 degrees and an average RF power of 23.5 W.

4.3. RESULTS

4.3.1. COIL CHARACTERIZATION

AFTER the assembly of the eight individual array elements, all elements were connected to a network analyzer for S-parameter characterization. A reflection coefficient (S_{11}) lower than –15 dB on all elements was measured when loaded with a human body. The plots for a resonator loaded with the human body, as well as that of an unloaded resonator (without any retuning of the impedance matching circuit) are given in Fig. 4.4.

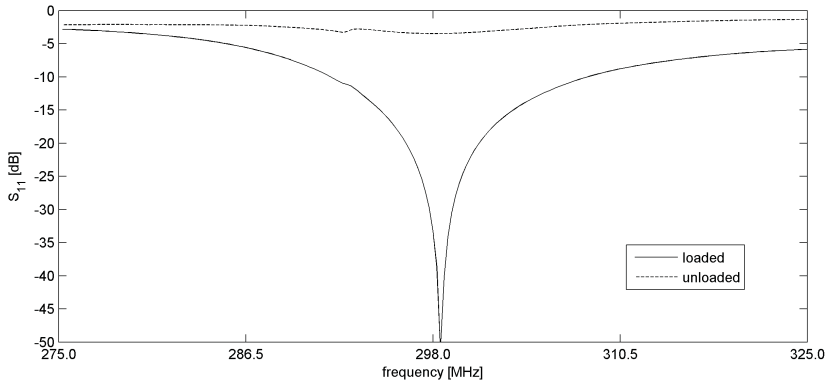


Figure 4.4: S_{11}-parameter plots of the loaded and unloaded shielded ceramic element in the eight-channel array. The data shown here were obtained from a volunteer with a high BMI > 30, the mean SS_{11} for three volunteers (low, medium and high BMI) was ~21.6 dB at 298.1 MHz with a standard deviation of 11.9 dB.

4.3.2. SINGLE ELEMENT ANALYSIS

The electric field and corresponding SAR distributions were examined first. All simulations were scaled to 1 W stimulated power and the IEEE C95.3 [7] averaging method was used to evaluate the 10 g average SAR ($SAR_{10g,avg}$). The IEEE C95.3 method uses a cube which is grown around the specific point P until it contains the required mass. Plots of the electric field and $SAR_{10g,avg}$ along the central plane through the phantom are shown in Fig 4.5.

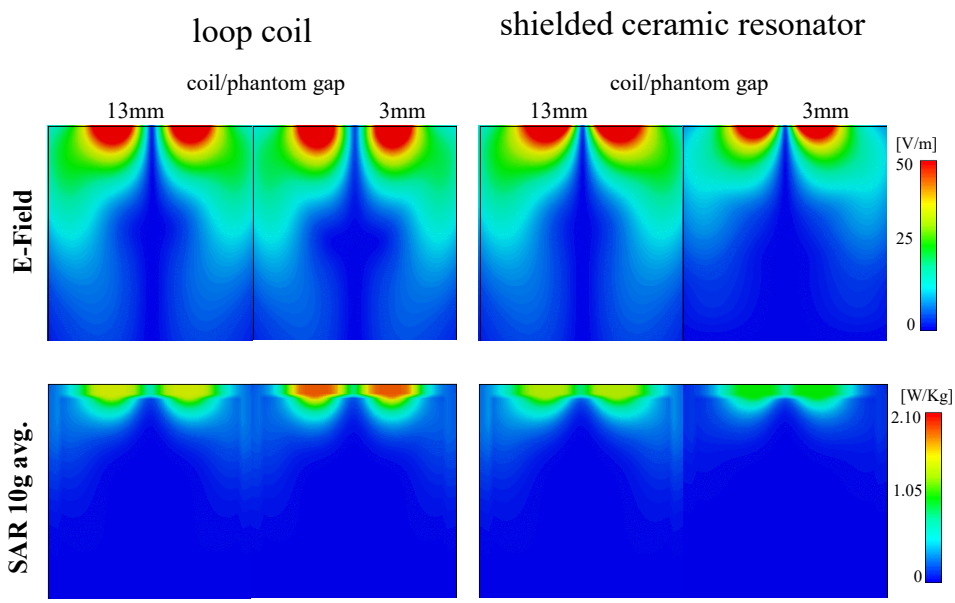


Figure 4.5: Top row: Electric field patterns for the loop coil and shielded dielectric resonator for 3 and 13 mm spacing between the phantom and coil. The bottom row gives the SAR_{10g} distribution for 3 and 13 mm spacing. All SAR plots are scaled to a maximum of 2.1 W/kg.

The simulations show that the general pattern of the electric field for both types of coil is very similar; in general the $SAR_{10g,avg}$ for the loop coil is higher compared to the shielded ceramic resonator. The SAR was also evaluated for the 1 g average (SAR_{1g}) according to the IEEE C95.3 averaging method, with results given in Table 4.1.

Table 4.1: Single element SAR analysis.

	3 mm gap between coil and phantom		13 mm gap between coil and phantom	
	SAR_{max} 10 g avg. (W/kg)	SAR_{max} 1 g avg. (W/kg)	SAR_{max} 10 g avg. (W/kg)	SAR_{max} 1 g avg. (W/kg)
Loop coil	2.06	3.54	1.54	2.29
Shielded ceramic resonator	1.79	2.76	1.40	2.03

The B_1^+ for 1 W input power (rms) and the $B_1^+/\sqrt{SAR_{10g,max}}$ were also evaluated in the same plane and the plots are given in Fig. 4.6. Here the elements all perform quite similarly. Experimental B_1^+ maps obtained with the dual-TR method, also shown in Fig. 4.6, confirm the general pattern from the simulations.

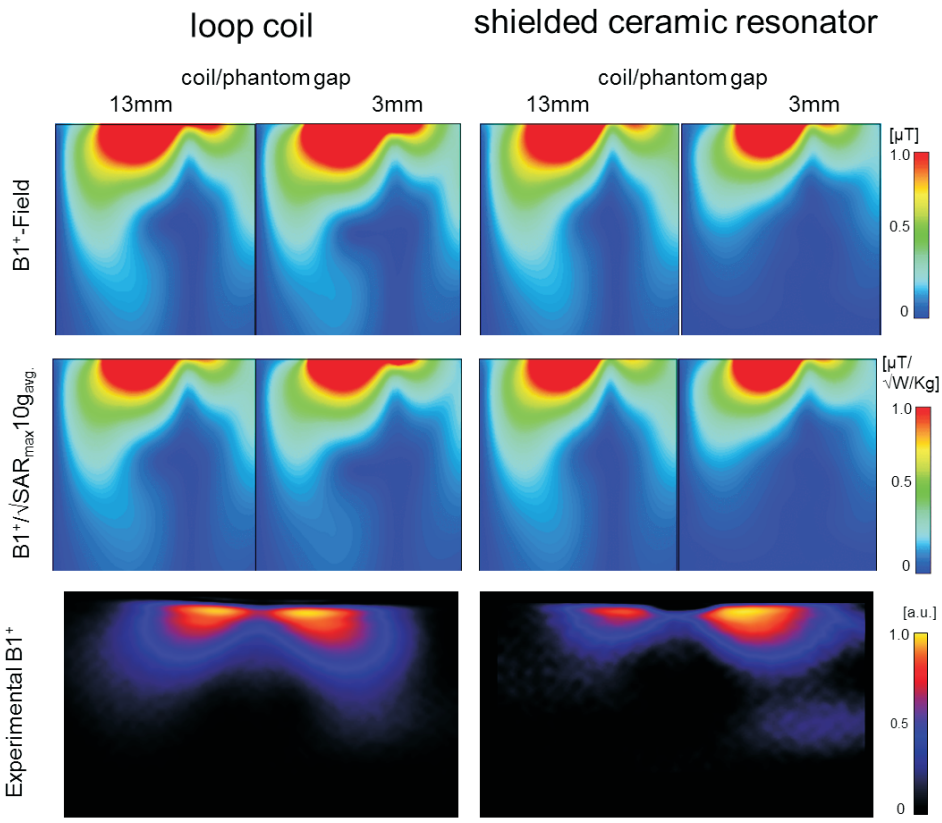


Figure 4.6: (top two rows) Simulated B_1^+ and $B_1^+/\sqrt{\text{SAR}_{10g,\text{max}}}$ distributions for the loop coil and shielded ceramic resonator with 1 Watt (rms) of input power and a uniform phantom. (bottom row) Experimentally-measured B_1^+ maps.

In order to assess the efficiency of the resonators the B_1^+ and maximum SAR ($\text{SAR}_{\text{max,10g}}$) divided by $(B_1^+)^2$ were evaluated along a perpendicular line 35 mm off-centre on the

left-hand side (as shown in Fig. 4.6) of the resonator which corresponds to the region of strongest B_1^+: these results are shown in Figs. 4.7 and 4.8.

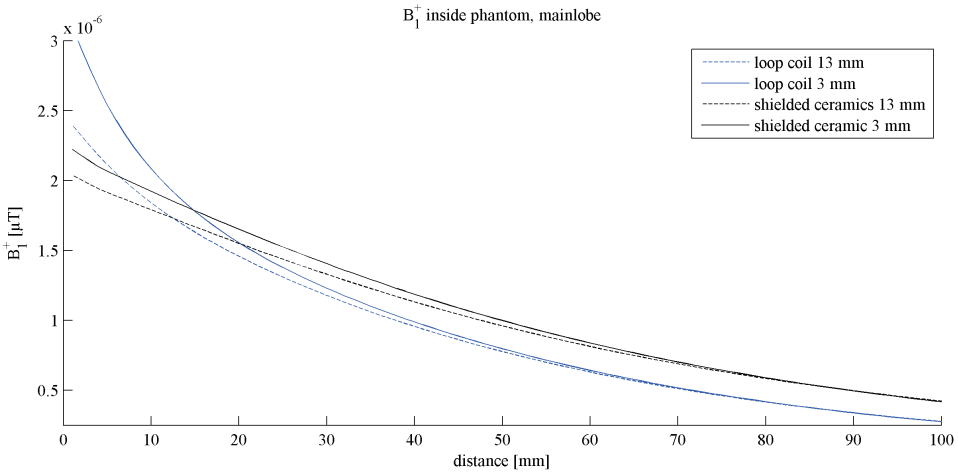


Figure 4.7: Plot of the simulated B_1^+ field as a function of distance from the surface of the resonant element for the loop coil and shielded ceramic for two different spacings (3 mm and 13 mm) of the phantom from the element.

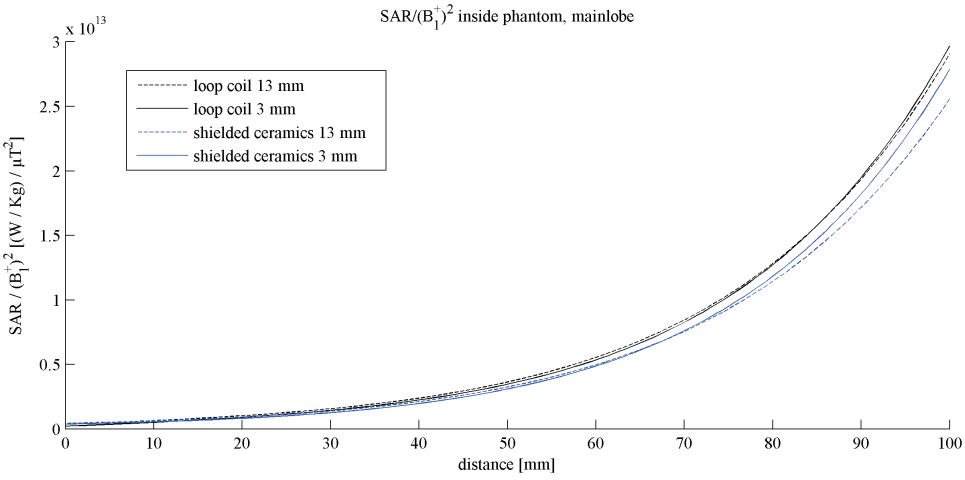


Figure 4.8: Plot of the SAR divided by the square of the B_1^+ field as a function of distance from the two different resonators.

4.3.3. ARRAY ANALYSIS

The coupling between neighboring elements as a function of the inter-element distance was investigated for the shielded ceramic resonator array, with each element spaced 1.5 cm apart, via a series of S_{12}-parameter measurements of a group of three volunteers (body mass index low, medium and high) in the array. The results of the measurement are given in Table 4.2 in terms of mean and standard deviation.

Table 4.2: S-parameter (dB) matrix (mean and standard deviation) for the shielded ceramics array, obtained from three volunteers with different BMIs.

Channel	1	2	3	4	5	6	7	8
1	-15 $\sigma = 4.3$	-16 $\sigma = 1.4$	-27 $\sigma = 5.9$	-39 $\sigma = 7.6$	-25 $\sigma = 3.3$	-39 $\sigma = 11.6$	-35 $\sigma = 7.5$	-36 $\sigma = 2.4$
2		-13 $\sigma = 1.2$	-15 $\sigma = 0.9$	-26 $\sigma = 3.3$	-36 $\sigma = 3.3$	-39 $\sigma = 4.1$	-36 $\sigma = 6.5$	-33 $\sigma = 1.2$
3			-13 $\sigma = 2.2$	-14 $\sigma = 0.5$	-47 $\sigma = 3.7$	-45 $\sigma = 3.8$	-36 $\sigma = 3.3$	-33 $\sigma = 2.4$
4				-23 $\sigma = 6.7$	-47 $\sigma = 10.6$	-44 $\sigma = 5.7$	-39 $\sigma = 8.2$	-33 $\sigma = 2.9$
5					-13 $\sigma = 0.5$	-18 $\sigma = 1.7$	-38 $\sigma = 8.5$	-44 $\sigma = 9.0$
6						-14 $\sigma = 2.5$	-19 $\sigma = 2.4$	-39 $\sigma = 4.1$
7							-16 $\sigma = 3.1$	-19 $\sigma = 1.7$
8								-13 $\sigma = 1.4$

The dual-transmit configuration is only able to provide one degree of freedom in terms of the phase difference between the two sets of anterior and posterior resonators (unlike full phase control for all elements in systems described elsewhere [5, 15]. As described in the methods, an empirical approach was adopted on a subject-specific basis in order to estimate the best relative phase settings. An example is shown in Fig. 4.9, in which the best image quality is produced with zero phase shift between the upper and lower channels. Plots of the simulated B_1^+, SAR and efficiency for the different resonator configurations are given in Fig. 4.10 for an input power of 1 kW for the zero degree phase shift condition shown in Fig. 4.9. It can be seen that the results are very similar for both the loop coil and ceramic resonator. The maximum 10 g averaged SAR was 0.53 W/kg for the loop coil and

0.48 W/kg for the ceramic resonator.

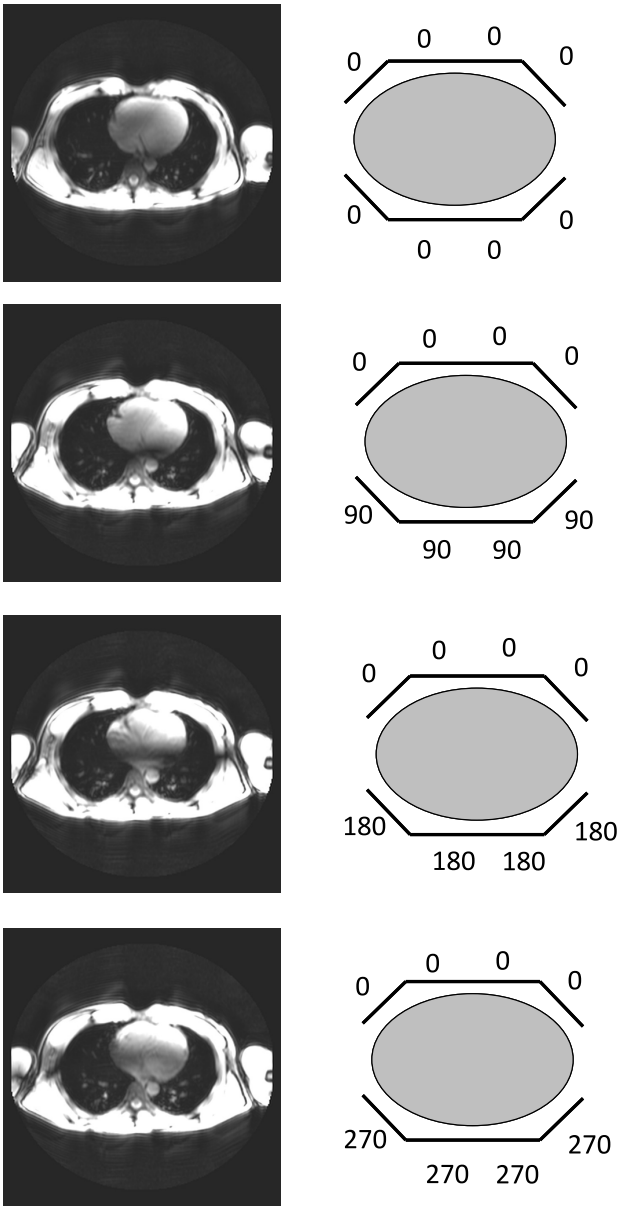


Figure 4.9: Scout images acquired with four different phase shifts between the upper and lower four elements of the array. This very coarse form of B_1-shimming shows that dark bands occur for a 0/90 and 0/180 configuration. The very left and right phase settings shift the dark bands to the right ventricle/atrium.

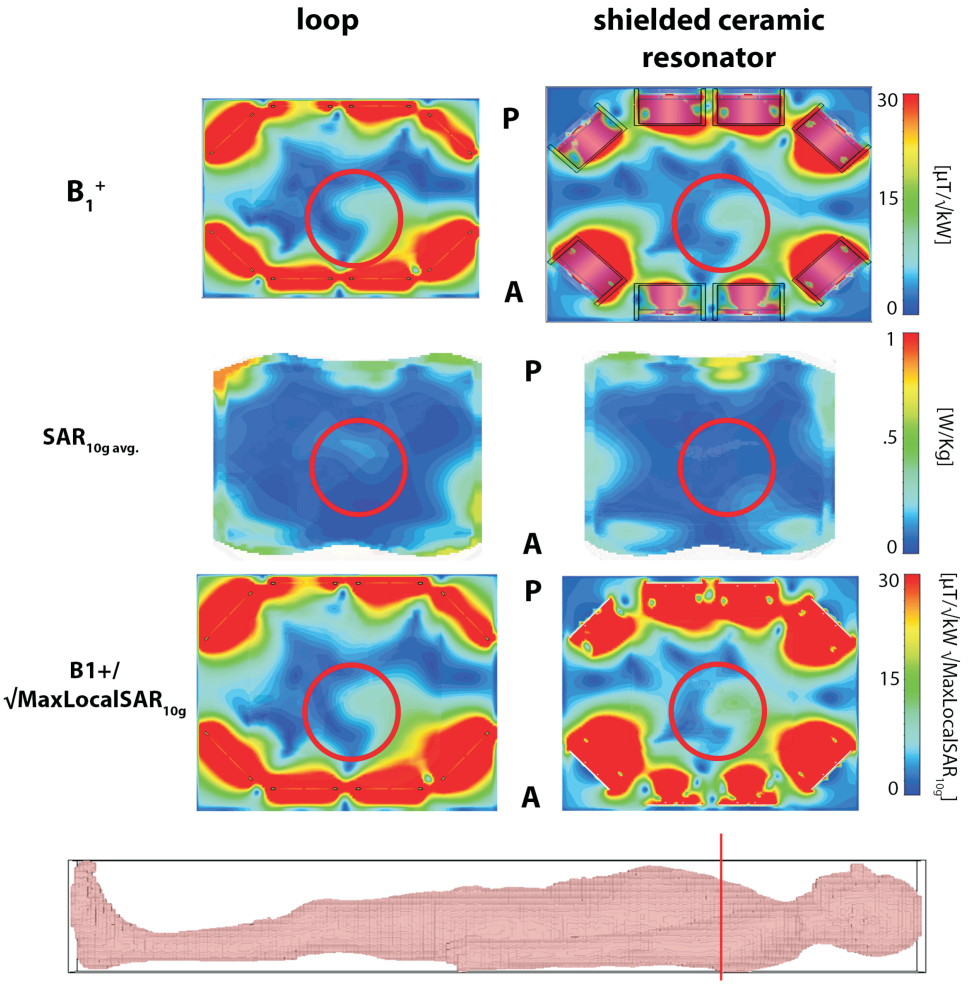


Figure 4.10: Whole body simulations for the loop coil and ceramic resonator with the Gustav model. The phase was set to be equal for all elements. The red circle gives the approximate position of the heart. The position of the cut plane is indicated at the bottom of the figure. The $SAR_{10g,avg}$ figures have been enlarged for better visibility.

4.3.4. IN VIVO RESULTS

Long-axis, short-axis and four-chamber views are shown in Fig. 11, with some views shown for subjects with a low, medium and high BMI. Based on a total power of 20 W time averaged over the whole sequence put out by the system, which corresponds to ~0.27 W/kg for a person with 75 kg body mass (whole body SAR), as the input for the EM simulation, the $SAR_{10g,avg}$ was calculated to be 1.23 W/kg.

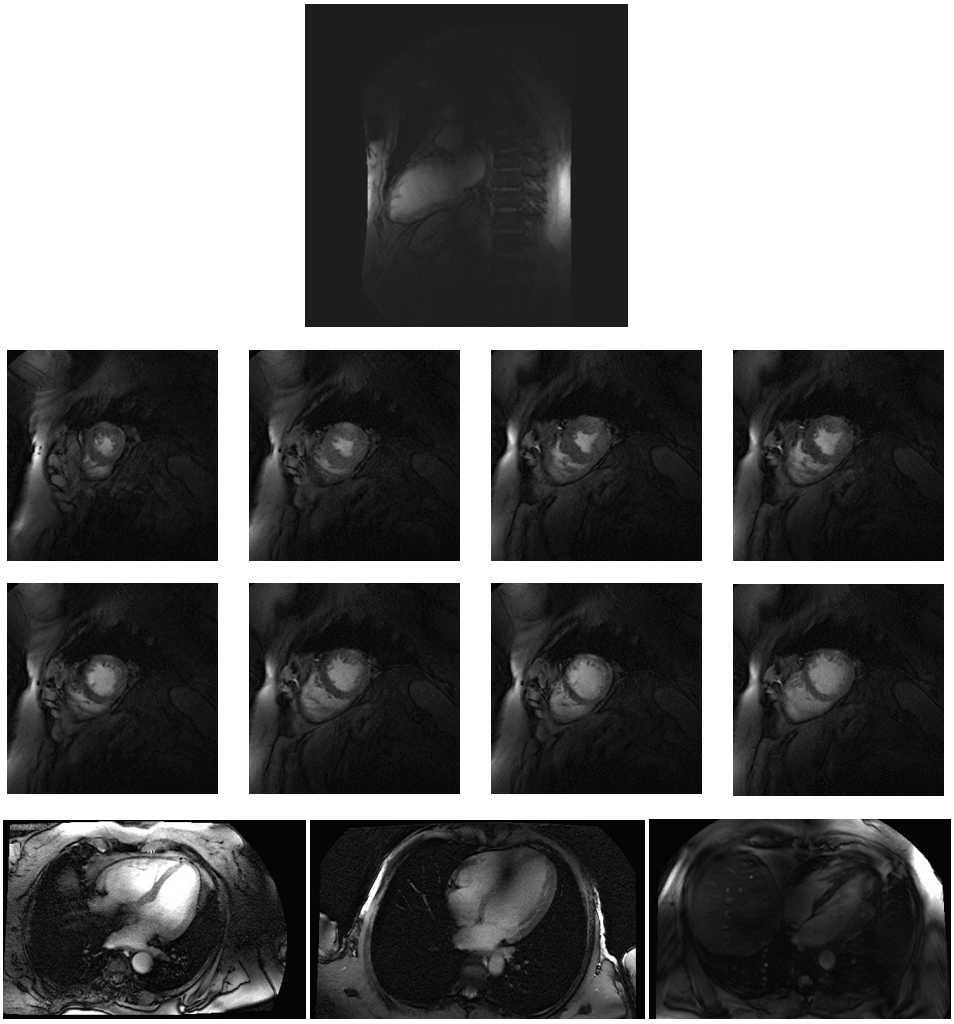


Figure 4.11: Images obtained from a volunteer. (top) two chamber view, (middle two rows) short axis multi-slice images, and (bottom) three four-chamber views obtained from three different volunteers with (BMI low-to-high from left-to-right). Imaging parameters are listed in the main text.

4.4. DISCUSSION

THE results of this work indicate that ceramic resonators can be used as an alternative to loops as surface coil elements at high field strengths. No particular attempt has been made to optimize the size of the resonators in terms of the specific application of cardiac imaging shown here, and so one can anticipate that further improvements could be made. Indeed the use of thinner disks with a larger radius, and/or an elongated rectangular construction, would increase the axial field-of-view. The loop design has been studied for over thirty years, with impressive results shown recently for a very large element-count transmit/receive array for cardiac imaging at 7 T [5]. The basic design of the ceramic resonator has some potential advantages including a smaller number of lumped elements and soldering joints, an inherent high quality factor (>1000 for the ceramic element), and a high degree of isolation between adjacent elements. The fact that the electric field is not concentrated around the lumped elements, but spread over a much larger volume results in a lower SAR for comparable detector sizes for small values of the gap between the body and the coil. However the simulations show for the 3 mm gap case less B_1^+ penetration depth compared to the loop coil. This is most likely due to the fact that the closer the dielectric resonator gets to the phantom the more the boundary condition changed on the contact side of the resonator. One inherent drawback of solid ceramics is of course their relative "inflexibility". Rapid in-house production is usually not possible as special equipment is needed to craft these ceramics, and the required ceramic firing facilities are not standard in academic facilities. There is, however, the possibility to overcome this drawback by using a homogeneous slurry of perovskite powder and a binder such as water as described by Teeuwisse et al. [16]. Those slurries have been shown to achieve even higher relative permittivity of ~300. These slurry can then be put into a plastic former to shape the resonator: simple 3D prototyping capabilities available in most laboratories would then allow the construction of arbitrary conformal shapes.

It should also be noted that these elements can be used as receive-only elements, with very effective detuning of the TE_{01} mode by pin-diode switching using well-established methods [2, 9]. In order to detune the dielectric resonator a conductive loop can either be incorporated into the dielectric resonator, or can be placed on top of the disk, with the diameter of the loop approximately two-thirds that of the resonator, i.e. where the electric field is a maximum. When the conductive loop is complete, this equalizes the electric field around the diameter of the loop, which destroys the modal structure. A pin diode is placed between the ends of the detuning loop, and then can be switched in the normal way.

For this study only two independent RF transmit channels were available, giving relatively minor flexibility in terms of B_1^+ shimming ability. Therefore, one can anticipate that the image quality could be improved by having full phase control over all eight elements, as has been shown by many other groups.

Another drawback for solid ceramic resonator is their weight. With a single element weighing about 1 kg, four resonators put a significant weight on the patient's chest'(one should also note that the weight of a typical commercial cardiac array at 3 T is less than this). However, in our tests all volunteers were comfortable with the extra weight and it did not obstruct breathing: in fact all the volunteers noted that after a couple of minutes they does not feel the extra weight.

Finally, it should be noted that the ceramic disks used in this study are relatively tall, dictated by the relative permittivity of ~170. This means that significant energy is stored within the resonator in the TE_{01} mode. The availability of materials with much higher permittivites, between 1000 and 2000, would allow much thinner DRAs to be designed, in which the TE_{01} mode is intrinsically more "leaky", thus producing a greater magnetic field within the subject. Thinner disks would also reduce the weight considerably.

REFERENCES

[1] S. Aussenhofer and A. Webb. High-permittivity solid ceramic resonators for high-field human mri. *NMR in Biomedicine*, 26(11):1555–1561, 2013.

[2] S. A. Aussenhofer and A. G. Webb. Design and evaluation of a detunable water-based quadrature hem11 mode dielectric resonator as a new type of volume coil for high field mri. *Magnetic Resonance in Medicine*, 68(4):1325–1331, 2012.

[3] A. Christ, W. Kainz, E. G. Hahn, K. Honegger, M. Zefferer, E. Neufeld, W. Rascher, R. Janka, W. Bautz, J. Chen, et al. The virtual family—development of surface-based anatomical models of two adults and two children for dosimetric simulations. *Physics in medicine and biology*, 55(2):N23, 2010.

[4] M. A. Dieringer, W. Renz, T. Lindel, F. Seifert, T. Frauenrath, F. von Knobelsdorff-Brenkenhoff, H. Waiczies, W. Hoffmann, J. Rieger, H. Pfeiffer, et al. Design and application of a four-channel transmit/receive surface coil for functional cardiac imaging at 7t. *Journal of Magnetic Resonance Imaging*, 33(3):736–741, 2011.

[5] A. Graessl, W. Renz, F. Hezel, M. A. Dieringer, L. Winter, C. Oezerdem, J. Rieger, P. Kellman, D. Santoro, T. D. Lindel, et al. Modular 32-channel transceiver coil array for cardiac mri at 7.0 t. *Magnetic Resonance in Medicine*, 72(1):276–290, 2014.

[6] F. Hezel, C. Thalhammer, S. Waiczies, J. Schulz-Menger, and T. Niendorf. High spatial resolution and temporally resolved t 2* mapping of normal human myocardium at 7.0 tesla: an ultrahigh field magnetic resonance feasibility study. *PLoS ONE*, 7:12, 2012.

[7] IEEE. Ieee standard c95.3 recommended practice for measurements and computations of radio frequency electromagnetic fields with respect to human exposure to such fields, 100 khz-300 mhz., 2008.

[8] Int. Soc. Magn. Reson. Med. *J.Y. Lu, X. Zhang, B.K. Rutt, A novel 7 T transmit array using TE01d mode dielectric resonators*, 2013.

[9] D. Kajfez. *Dielectric Resonators*. Institution Engineering & Tech, 1998.

[10] W. Koning, J. Bluemink, E. Langenhuizen, A. Raaijmakers, A. Andreychenko, C. den Berg, P. Luijten, J. Zwanenburg, and D. Klomp. High-resolution mri of the carotid arteries using a leaky waveguide transmitter and a high-density receive array at 7 t. *Magnetic Resonance in Medicine*, 69(4):1186–1193, 2013.

[11] O. Kraff, A. K. Bitz, T. Breyer, S. Kruszona, S. Maderwald, I. Brote, E. R. Gizewski, M. E. Ladd, and H. H. Quick. A transmit/receive radiofrequency array for imaging the carotid arteries at 7 tesla: coil design and first in vivo results. *Investigative radiology*, 46(4):246–254, 2011.

[12] T. Niendorf, A. Graessl, C. Thalhammer, M. A. Dieringer, O. Kraus, D. Santoro, K. Fuchs, F. Hezel, S. Waiczies, B. Ittermann, et al. Progress and promises of human cardiac magnetic resonance at ultrahigh fields: a physics perspective. *Journal of Magnetic Resonance*, 229:208–222, 2013.

[13] A. Raaijmakers, O. Ipek, D. Klomp, C. Possanzini, P. Harvey, J. Lagendijk, and C. Van den Berg. Design of a radiative surface coil array element at 7 t: The single-side adapted dipole antenna. *Magnetic Resonance in Medicine*, 66(5):1488–1497, 2011.

[14] C. Snyder, L. DelaBarre, G. Metzger, P.-F. van de Moortele, C. Akgun, K. Ugurbil, and J. Vaughan. Initial results of cardiac imaging at 7 tesla. *Magnetic resonance in Medicine*, 61(3):517–524, 2009.

[15] C. Snyder, L. DelaBarre, S. Moeller, J. Tian, C. Akgun, P.-F. Van de Moortele, P. Bolan, K. Ugurbil, J. Vaughan, and G. Metzger. Comparison between eight-and sixteen-channel tem transceive arrays for body imaging at 7 t. *Magnetic Resonance in Medicine*, 67(4):954–964, 2012.

[16] W. Teeuwisse, W. Brink, K. Haines, and A. Webb. Simulations of high permittivity materials for 7 t neuroimaging and evaluation of a new barium titanate-based dielectric. *Magnetic Resonance in Medicine*, 67(4):912–918, 2012.

[17] C. Thalhammer, W. Renz, L. Winter, F. Hezel, J. Rieger, H. Pfeiffer, A. Graessl, F. Seifert, W. Hoffmann, F. von Knobelsdorff-Brenkenhoff, et al. Two-dimensional sixteen channel transmit/receive coil array for cardiac mri at 7.0 t: Design, evaluation, and application. *Journal of Magnetic Resonance Imaging*, 36(4):847–857, 2012.

[18] S. G. van Elderen, M. J. Versluis, A. G. Webb, J. J. Westenberg, J. Doornbos, N. B. Smith, A. de Roos, and M. Stuber. Initial results on in vivo human coronary mr angiography at 7 t. *Magnetic Resonance in Medicine*, 62(6):1379–1384, 2009.

[19] S. G. van Elderen, M. J. Versluis, J. J. Westenberg, H. Agarwal, N. B. Smith, M. Stuber, A. de Roos, and A. G. Webb. Right coronary mr angiography at 7 t: A direct quantitative and qualitative comparison with 3 t in young healthy volunteers 1. *Radiology*, 257(1):254–259, 2010.

[20] J. T. Vaughan, C. J. Snyder, L. J. DelaBarre, P. J. Bolan, J. Tian, L. Bolinger, G. Adriany, P. Andersen, J. Strupp, and K. Ugurbil. Whole-body imaging at 7t: Preliminary results. *Magnetic resonance in Medicine*, 61(1):244–248, 2009.

[21] F. von Knobelsdorff-Brenkenhoff, T. Frauenrath, M. Prothmann, M. A. Dieringer, F. Hezel, W. Renz, K. Kretschel, T. Niendorf, and J. Schulz-Menger. Cardiac chamber quantification using magnetic resonance imaging at 7 tesla—a pilot study. *European radiology*, 20(12):2844–2852, 2010.

[22] F. von Knobelsdorff-Brenkenhoff, V. Tkachenko, L. Winter, J. Rieger, C. Thalhammer, F. Hezel, A. Graessl, M. A. Dieringer, T. Niendorf, and J. Schulz-Menger. Assessment of the right ventricle with cardiovascular magnetic resonance at 7 tesla. *J Cardiovasc Magn Reson*, 15(23):10–1186, 2013.

[23] A. Webb. Visualization and characterization of pure and coupled modes in water-based dielectric resonators on a human 7t scanner. *Journal of Magnetic Resonance*, 216:107–113, 2012.

[24] H. Wen, F. A. Jaffer, T. J. Denison, S. Duewell, A. S. Chesnick, and R. S. Balaban. The evaluation of dielectric resonators containing h_2o or d_2o as rf coils for high-field mr imaging and spectroscopy. *Journal of Magnetic Resonance, Series B*, 110(2):117–123, 1996.

[25] L. Winter, P. Kellman, W. Renz, A. Gräßl, F. Hezel, C. Thalhammer, F. von Knobelsdorff-Brenkenhoff, V. Tkachenko, J. Schulz-Menger, and T. Niendorf. Comparison of three multichannel transmit/receive radiofrequency coil configurations for anatomic and functional cardiac mri at 7.0 t: implications for clinical imaging. *European radiology*, 22(10):2211–2220, 2012.

5

EVALUATION OF PLASMA-BASED TRANSMIT COILS FOR MAGNETIC RESONANCE

Sebastian A. AUSSENHOFER

Andrew G. WEBB

Parts of this chapter have been published in Journal of Magnetic Resonance **261**, 49-53 (2015) [1].

5

In this work a new concept for designing transmit coils for magnetic resonance using a plasma is introduced. Unlike conventional coils, a plasma can be turned on and off, eliminating electrical interactions between coils, and enabling radiofrequency-invisibility when desired. A surfatron has been designed to produce a surface-mode wave which propagates along the inner surface of a commercial fluorescent lighting tube. NMR spectra and images have been produced using the plasma as the transmit coil and a copper-based monopole to receive the signal. The transmit efficiency of the plasma tube was estimated, and is currently much lower than that of an equivalently-sized metal-based structure: however, there are many potential methods for increasing the efficiency using a custom-built plasma tube.

5.1. INTRODUCTION

NUCLEAR magnetic resonance (NMR) spectroscopy and magnetic resonance imaging (MRI) both use radiofrequency (RF) coils which are constructed from conductive metallic elements. Although there are a large number of different coil geometries used for various NMR and MRI applications [2], the use of metallic elements is almost universal (a few publications have used high permittivity ceramic dielectric resonators [3]). In this paper, a new concept for an MR transmit coil is introduced, which uses a reconfigurable conducting plasma rather than a fixed-geometry metallic conductor. A plasma consists of an electrically neutral medium of positive and negative particles, and is used in applications as diverse as non-invasive surgery and nuclear fusion. A plasma can be characterized in terms of its plasma frequency, ω_p, given in Anderson (p32) [4]:

$$\omega_p = \sqrt{\frac{n_e q_e^2}{\epsilon_0 m_e}} \tag{5.1}$$

where n_e is the electron number density (measured in m^{-3}), m_e the electron mass, ϵ_0 the permittivity of free space, and q_e the electron charge. Evaluating the fundamental constants this gives:

$$\omega_p \approx 56.4\sqrt{n_e} \tag{5.2}$$

A plasma can be conveniently created within a dielectric (usually glass, quartz or plastic) tube. The plasma is typically created at one end of the tube and propagates very rapidly along the tube via a surface-mode wave between the plasma and dielectric. The propagation vector of this surface-mode wave is real along the plasma/dielectric boundary and imaginary in the direction perpendicular to the boundary, which corresponds to the condition that the real part of the relative permittivity of the plasma is less than –1 [5, 6]. The frequency-dependent permittivity of the plasma is given by:

$$\epsilon(\omega) = \epsilon_0 \left(1 - \frac{\omega_p^2}{\omega^2} - j\frac{\omega_p^2}{\omega \nu_{cc}}\right) \tag{5.3}$$

where ν_{cc} is the electron-neutral collision frequency of the plasma. The condition that

$\epsilon < -1$ means that $\omega_p > \omega\sqrt{2}$. In practice, as described in Anderson (p46) [4], a general rule-of-thumb is that the plasma frequency must be at least twice the operational frequency for the plasma to act similarly to a metal antenna.

The feasibility of using a plasma as a transmitter in MR experiments was investigated using a commercial fluorescent lighting tube. For this type of fluorescent tube $n_e \sim 10^{17} m^{-3}$, which gives a plasma frequency of ~2.8 GHz from Eq. 5.2, which is much higher than the Larmor frequencies in NMR and MRI, thus satisfying the conditions in Eq. 5.3. Experiments have been performed to characterize the plasma performance in terms of transmit efficiency compared to a conventional metallic conductor, and plasma relaxation times.

5.2. PRODUCTION OF THE PLASMA

INITIAL experiments were performed using a simple commercially-available fluorescent tube (Master TL 8W/827, 14 mm diameter, 30 cm length, Osram) to generate the plasma. The glass tube is filled with Argon at a pressure of ~2.5 Torr, with a mercury vapor pressure of 6–10 mTorr. Experiments were performed on a 7 T human MRI system (Philips Achieva). Lower clinical field strengths of 3 T and 1.5 T could equally well have been used: the 7 T was chosen due to the ease of interfacing custom built hardware to the scanner.

There are many ways to create a plasma within the tube. For example, the normal lighting mode uses an external DC source (via rectification of the AC mains) to heat the internal tungsten electrodes which emit free electrons via thermionic emission: these electrons ionize the argon gas atoms close to the filament to form a plasma via impact ionization. In this study the RF pulse used for MR excitation was used to create a non-ionizing surface wave which propagates along the interface between the glass tube and the plasma column. This wave can be produced most easily using a "surfatron", a device to create a strong electric field (on the order of several kV/m) which passes through the plasma tube to a ground plane. Different surfatron devices for various frequency bands have been reviewed by Moisan and Zakrzewski [7]. The particular surfatron design for these feasibility experiments consisted of a single wide copper band, impedance-matched to 50 Ω at 298.1 MHz (i.e. a design essentially identical to a loop gap resonator [8]), with a ground plane in close proximity, as shown in Fig. 5.1. The RF pulse from the amplifier establishes the plasma effectively instantaneously (typical plasma rise times are less than 1 μs.

A copper tube with the same length as the plasma tube and similarly-sized ground plane was used as a monopole element in order to compare the relative transmit sensitivity of the plasma and metal conductor, as well as being used as the receive element for spectroscopy experiments using the plasma as the transmitting source.

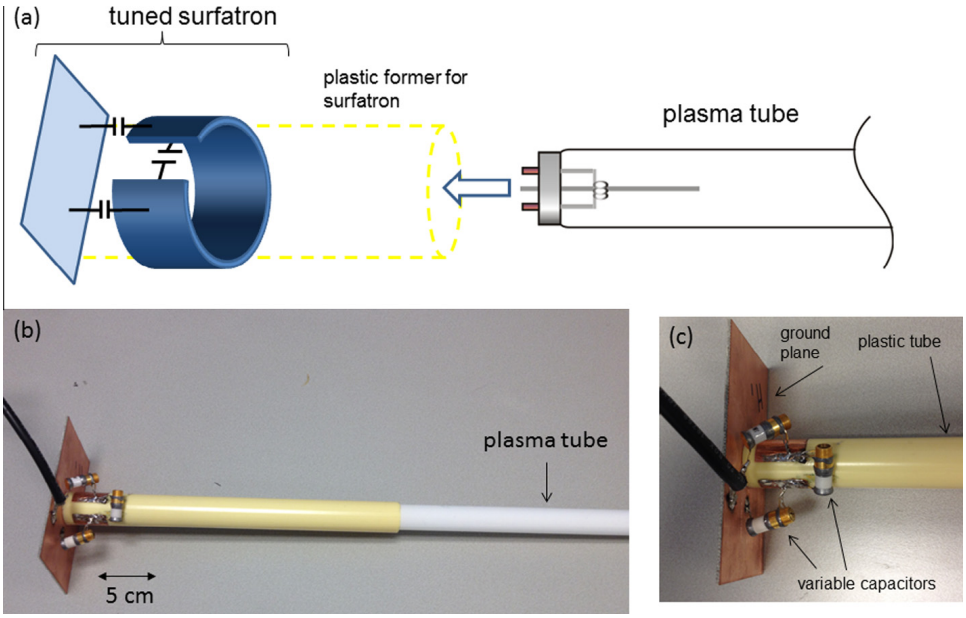


Figure 5.1: (a) Schematic of the surfatron used to produce the plasma. The circuit formed by the copper band and ground plane is resonated and impedance matched to 50 Ω at 298.1 MHz using three capacitors in a π-configuration. The surfatron is constructed on a thin plastic tube for mechanical support (yellow dotted line), and the tube is also used to center the plasma tube within the surfatron. The plasma tube is inserted through the copper band. The strong electric field (~2 kV/m) produced between the copper band and the ground plane passes through the tube and creates the plasma via a traveling surface wave. (b) Photograph of the assembled surfatron on the plastic former (yellow tube), and the plasma tube inserted into the plastic former. (c) Expanded view of the constructed surfatron showing the three variable capacitors (1–30 pF, Voltronics) used for impedance matching. The copper band has a width of 2 cm.

5.3. RESULTS

IN order to determine whether the idea of a plasma-based coil is feasible a small sample (1 × 1 × 1 cm) of paraffin oil was placed next to the axial mid-point of the plasma tube. Fig. 5.2a shows the free induction decay measured using the plasma to transmit and receive the signal. The signal decays very rapidly, effectively providing a measure of the plasma decay time after the RF pulse has been turned off. The signal decays with a time constant of ~4 ms, the primary relaxation mechanism being ambipolar diffusion to the lamp walls. The fact that the rapid signal decay is indeed caused by this relaxation was tested by using the plasma to transmit the RF pulse and the monopole (placed ~10 cm away from the plasma tube and sample to ensure that there is no coupling between the two elements) to receive the signal: the resulting FID is shown in Fig. 5.2b, clearly indicating that the very rapid signal decay shown in Fig. 5.2a is due to decay of the plasma. These results indicate that, in this particular configuration the plasma would only be suitable for signal detection in experiments in which the acquisition bandwidth is extremely large, e.g. for solid samples or for short echo time high-readout-bandwidth imaging.

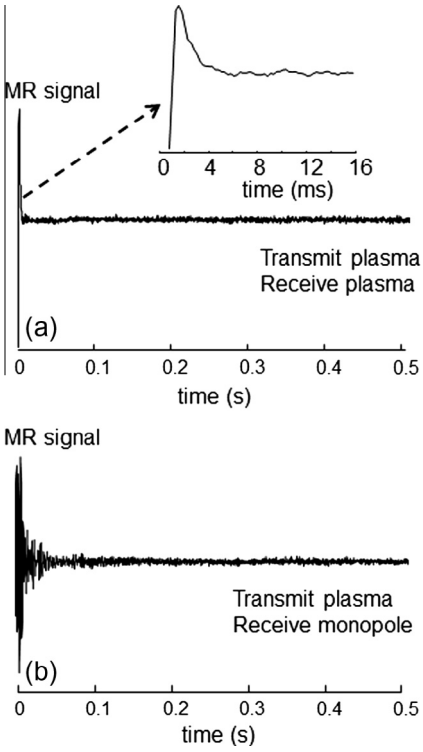


Figure 5.2: Experiments using a plasma tube and copper monopole in different transmit/receive configurations. (a) If the plasma tube is used both to transmit the RF pulse and receive the signal, then the time-domain MR signal is strongly damped since the plasma relaxes with a time constant on the order of 4 ms. (b) When the plasma is used to transmit the RF pulse, and a conventional conductor-based coil is used to receive the MR signal, the free induction decay lasts much longer, determined by the T_2/relaxation time.

The second experiment was performed in order to determine whether any component of the signal shown in Fig. 2 arises from the surfatron itself rather than the plasma, since it is well-established that traveling-wave effects [9, 10] can occur on human magnets at 7 and 9.4 T. A thin tube of water (diameter 2 cm, length 20 cm) was placed next to the plasma tube. Fig. 5.3 shows the results from a low tip angle 3D gradient echo imaging experiment (TR 25 ms, TE 1.1 ms, data matrix 132 × 136 × 20, field-of-view 10 × 40 × 10 cm). Fig. 5.3a shows one slice through the center of the water sample. Fig. 5.3b shows the corresponding experiment under identical conditions except with the plasma tube removed. These results indeed indicate that there is no measurable travelling wave component, and that the entire spectroscopic and imaging signal intensities shown in Figs. 5.2 and 5.3 arises from

the magnetic field created by current flowing in the plasma. A similar experiment was performed in which the gas was removed from the plasma tube: again no signal was detected.

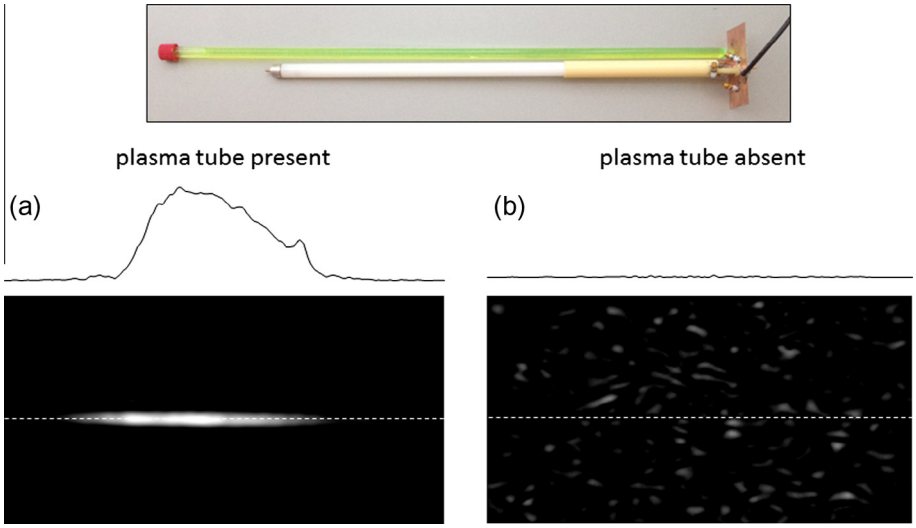


Figure 5.3: Top – physical arrangement of a long glass tube filled with water (and a dye for visibility purposes only) placed next to the plasma tube. Gradient echo images acquired (a) with and (b) without the plasma tube positioned in the surfatron. A line plot along the dotted line is shown above each image. The lack of signal in (b) shows that there is no traveling wave component to the signal detected in (a).

Fig. 5.4a shows the results of a pulse width calibration to measure the transmit efficiency of the plasma using the small paraffin oil sample described earlier. The signal intensity was measured as a function of input power to the surfatron: a block pulse with duration 2.6 ms was used. The input power (measured at the input to the plasma coil) required for the maximum signal intensity was 700 W. Since a small sample was used, one can approximate the maximum signal intensity as corresponding to a 90° pulse (despite the intrinsically inhomogeneous B_1^+ field produced by a rod-like structure) which translates to a transmit coil efficiency, defined as B_1^+ (Watt)$^{1/2}$, of 0.09 μT/$\sqrt{W}$. A similar experiment was performed using the monopole, with the sample positioned identically to that using the plasma tube, with the results plotted on the same power scale in Fig. 5.4b. In this case a transmit coil efficiency of 0.75 μT/$\sqrt{W}$ was measured, a factor of 8.3 greater than the plasma.

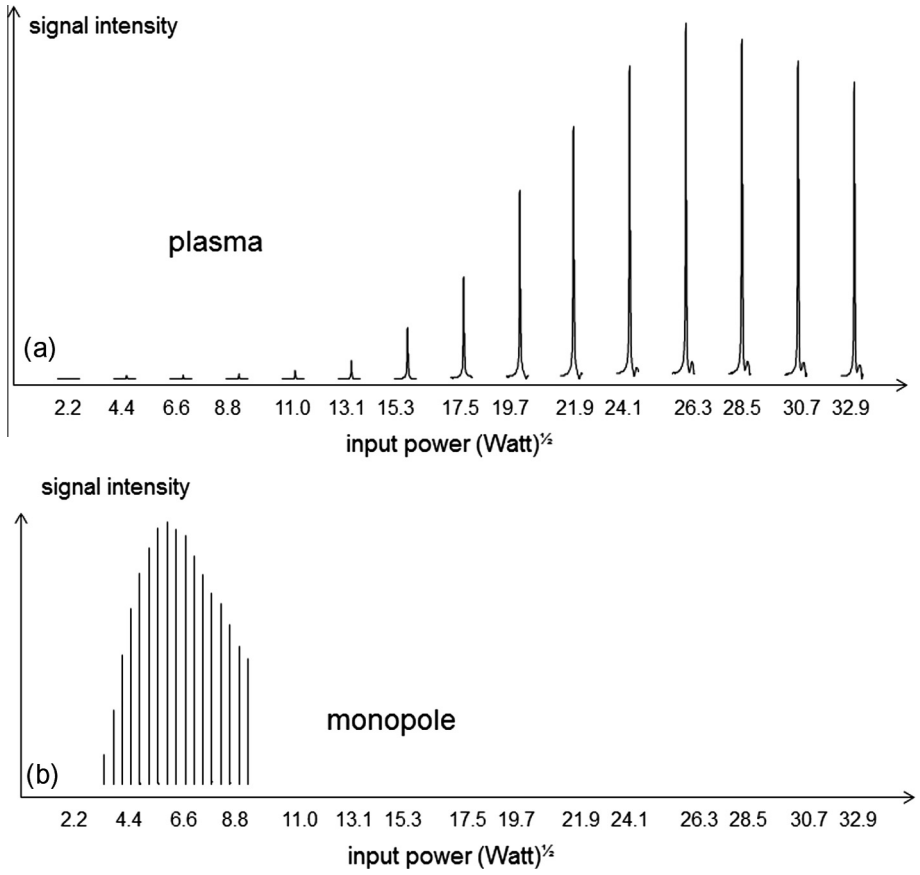


Figure 5.4: Pulse width calibrations used to measure the coil transmit efficiency by plotting signal intensity vs. the square root of input power. A 2.6 ms long hard pulse was used. (a) Plasma transmit, monopole receive. The maximum signal intensity occurs at an input power of ~700 W. (b) Monopole transmit, monopole receive, plotted on the same power scale for ease of comparison. The maximum signal intensity occurs at an input power of ~40 W.

5.4. DISCUSSION

INITIAL experiments outlined in this work illustrate the feasibility of using plasmas for magnetic resonance, even with very simple fluorescent tubes. The efficiency of the current plasma setup is much lower than that of an equivalently-sized copper conductor element. However, this is unsurprising given that an off-the-shelf lighting tube has been used as the plasma element. Significant improvements in the plasma performance can be anticipated if a custom-built tube is manufactured. The diameter of the tube can be reduced substantially reducing the power required to ionize the gas, and the gas pressure can also be adjusted. If the plasma pressure and electron density are increased then the plasma current increases, but the collision frequency increases which increases losses in the plasma, and so a compromise would have to be determined. Alternative plasma sources such as cold cathode fluorescent lamps (CCFLs) may be more appropriate since they do not require electrode heating to form the plasma. The geometry of the tube can also be improved: in the current implementation the plasma tube is fed from one end, effectively producing an electrical monopole. Symmetric central feeding of a two-tube element in a "dipole would produce a field more suitable for MRI. Finally, a more efficient surfatron can certainly be designed, since in the current configuration only a small fraction of the electric field passes through the plasma: for example Fig. 5.4a shows that at input powers up to ~100 W, the plasma is not fully ignited.

The current implementation uses the plasma as the transmit coil and a conventional conductor-based device to receive the MR signal. However, it may also be possible in the future to design a system in which the plasma is used for both transmission and reception, if desired. This would involve having two inputs to the plasma tube: one continuous low-frequency plasma excitation signal to maintain the plasma during signal detection by exciting the $m = 0$ surface wave [11, 12], and the other the high frequency input for producing RF pulses at the MR operating frequency. Since these signals are well-separated in frequency there would be negligible cross-talk. Alternatively, it may be feasible to alter the gas composition and/or pressure such that the plasma relaxation rate is decreased significantly. If the plasma were to be used as a receiver it is also important to consider the relevant noise characteristics and noise sources. These have been reported in several publications [13, 14], and are summarized in Chapter 12 of Ref. [4]. The noise spectrum of a plasma is given by

$$H(\nu) = 4RkT\left(\frac{1}{1+\frac{(2\pi\nu)^2}{\nu_{cc}^2}}\right) \tag{5.4}$$

where υ is the frequency of the transmitter in Hertz and υ_{cc} is the electron-gas atom collision frequency. Comparing this to the standard equation for Johnson noise for a conductor, one can see that whether the plasma has a higher or lower noise level than a conductor depends upon the relationship between the Larmor frequency and the collision frequency, the latter of which can be manipulated via the gas pressure in the plasma.

It should be emphasized that there are several important differences between the operation of a plasma and a conductor-based coil for MR applications. For example, under the pure travelling wave conditions of the propagating surface-mode wave, the electron density decreases as a function of distance from the surfatron, which means that the conductivity along the plasma tube also decreases. Below a certain critical value of plasma density, $n_{critical}$, the conductivity becomes zero:

$$n_{critical} = \frac{4\pi\epsilon_0 m_e}{e^2} f^2 (1+\epsilon_d) \tag{5.5}$$

The higher the applied power the higher the plasma density, and so the effective length of the plasma column depends on the input power: one can either view this as an extra degree-of-freedom in designing new types of experiments in which the spatial distribution of B_1^+ can be controlled by effectively altering the length of the RF coil, or alternatively as an inconvenient nuisance in that the peak input impedance is no longer a fixed value. As with conventional conductor-based RF coils it is important that the plasma tube not come into direct contact with the object/subject being studied, since this may alter the plasma distribution slightly. If the transmit efficiency of the plasma can be increased, one of the major advantages of using this approach would be that there would be no interaction between a plasma transmit coil and a conductor or plasma receive coil, which means that electrical isolation circuits could be eliminated. Other potential advantages include the increased radiation transparency of plasmas versus metals for hybrid imaging systems such as PET/MRI and SPECT/MRI.

5.5. ACKNOWLEDGMENTS

Support for this study was provided by the FP7 Grant SUBLIMA (AGW and SAA) and an ERC Advanced Grant (AGW). We would like to thank Drs. Ted Anderson and Fred Dyer of Haleakala Industries, and Prof. Gary Eden at the University of Illinois at Urbana-Champaign for discussion of plasma properties. Dr. Paul de Bruin and Prof. Wouter Teeuwisse aided with data acquisition.

REFERENCES

[1] S. Aussenhofer and A. Webb, *An eight-channel transmit/receive array of te 01 mode high permittivity ceramic resonators for human imaging at 7t,* Journal of Magnetic Resonance **243**, 122 (2014).

[2] S. A. Aussenhofer and A. G. Webb, *Design and evaluation of a detunable water-based quadrature hem11 mode dielectric resonator as a new type of volume coil for high field mri,* Magnetic Resonance in Medicine **68**, 1325 (2012).

[3] A. Webb, N. Smith, S. Aussenhofer, and H. Kan, *Use of tailored higher modes of a birdcage to design a simple double-tuned proton/phosphorus coil for human calf muscle studies at 7 t,* Concepts in Magnetic Resonance Part B: Magnetic Resonance Engineering **39**, 89 (2011).

[4] T. Anderson, *Plasma Antennas* (Artech House, 2011).

[5] A. Shivarova and I. Zhelyazkov, *Surface waves in a homogeneous plasma sharply bounded by a dielectric,* Plasma Physics **20**, 1049 (1978).

[6] A. Trivelpiece and R. Gould, *Space charge waves in cylindrical plasma columns,* Journal of Applied Physics **30**, 1784 (1959).

[7] M. Moisan and Z. Zakrzewski, *Plasma sources based on the propagation of electromagnetic surface waves,* Journal of Physics D: Applied Physics **24**, 1025 (1991).

[8] W. Froncisz and J. S. Hyde, *The loop-gap resonator: a new microwave lumped circuit esr sample structure,* Journal of Magnetic Resonance (1969) **47**, 515 (1982).

[9] D. O. Brunner, N. De Zanche, J. Fröhlich, J. Paska, and K. P. Pruessmann, *Travelling-wave nuclear magnetic resonance,* Nature **457**, 994 (2009).

[10] J. T. Vaughan, C. J. Snyder, L. J. DelaBarre, P. J. Bolan, J. Tian, L. Bolinger, G. Adriany, P. Andersen, J. Strupp, and K. Ugurbil, *Whole-body imaging at 7t: Preliminary results,* Magnetic resonance in Medicine **61**, 244 (2009).

[11] J. P. Rayner, A. P. Whichello, and A. D. Cheetham, *Physical characteristics of plasma antennas,* Plasma Science, IEEE Transactions on **32**, 269 (2004).

[12] V. Kumar, M. Mishra, and N. Joshi, *Study of a fluorescent tube as plasma antenna.* Progress in electromagnetics research letters **24**, 17 (2011).

[13] G. Borg, J. Harris, N. Martin, D. Thorncraft, R. Milliken, D. Miljak, B. Kwan, T. Ng, and J. Kircher, *Plasmas as antennas: Theory, experiment and applications,* Physics of Plasmas (1994-present) **7**, 2198 (2000).

[14] G. G. Borg, J. H. Harris, D. G. Miljak, and N. M. Martin, *Application of plasma columns to radiofrequency antennas,* Applied physics letters **74**, 3272 (1999).

6

General Discussion and Future Developments

This is a concluding chapter wherein the scientific and technical implications for society of the research findings of this thesis are discussed, possible future developments are also identified.

6.1. General Discussion

6.1.1. Discussion on Dielectric Resonators

Dielectric resonators are promising new RF coils for human magnetic resonance imaging.Whilst they have been previously described in the literature for human imaging by Wen [37], through the presently described work we have systematically developed dielectric resonators to a stage that they are now usable by other researchers and RF engineers in the field of human ultra-high field magnetic resonance imaging.

Through the research described in chapter 2, it was for the first time demonstrated that dielectric resonators can be used as effective transmit and receive coils for high field magnetic resonance imaging. The use of the HEM mode and thus the possibility to use quadrature feeding of the coil offers an increase in efficiency of $\sqrt{2}$ over the linear drive mode. Also, the coaxial orientation of the HEM resonator with respect to B_0 is advantageous when building dielectric resonators conformal to the human body.

It was shown that with a very simple and inexpensive design, RF coils that use water as a dielectric can be designed and built. These dielectric coils can be used for human magnetic resonance imaging with a performance very similar to the established birdcage resonator design. This is not surprising if one considers how a birdcage resonator is constructed. It also allows a stable, time-invariant electromagnetic wave to exist in its lumped element network. The higher order modes of the birdcage resonator can be viewed as a small sample of possible higher order modes of a similar sized dielectric resonator. This analogy becomes even more clear when the number of rungs of the birdcage resonator is increased; as the number of rungs approaches infinity, the structure of the bird cage resonator approaches that of a dielectric resonator coil.

One major aspect of RF coil design, besides improving efficiency, is that the specific absorption rate of the human body must be taken into consideration as it imposes conditions for safe operation of the RF coil. In a birdcage resonator, the electric fields which cause tissue heating emanate from the capacitors thereof. The electric field strength is highest around these components. The dielectric resonator has an advantage in that there are no lumped elements and thus the electric field that interacts with the human body is distributed out over a much larger surface area thus potentially lowering the SAR value.

A further advantage of dielectric resonators over birdcage coils is that much smaller

length to diameter ratios can be used. This is useful to the coil builder; or access to extremities, shorter coils are desirable as they restrict the motion less and bring more patient comfort.

It has been shown that the earlier published empirical formulas, although derived from dielectrics with a lower permittivity and at an operating frequency in the GHz range, are still quite accurate for water as a dielectric and in the MHz range.

While our first resonator used water as a dielectric, it was desired to use a more common dielectric material (like barium titanate for example): water has a relatively high loss tangent when compared to barium titanate or perovskites in general. However, it has to be born in mind that the Q-value of a dielectric resonator is only very high in the unloaded case ($Q_{unloaded} = \frac{1}{tan\delta}$). A very high Q would be favorable in a situation where the dielectric resonator is used as a radiative element, such as as described in chapter 4 for the 7 Tesla cardiac array, in order to radiate power away from the element into the body. If the DRA is to be used similarly to a conventional birdcage or loop gap resonator, as described in chapters 2 and 3, one might choose a lower Q in order to maximize the field within the resonator instead of radiating it away from the coil.

Effective detuning of an RF coil is needed if the coil is to be run in a transmit or receive only mode as is common nowadays in commercial magnetic resonance imaging scanners for humans. Spin excitation is usually achieved using the large body coil during the transmit phase. The body coil is then detuned and a local receive coil is switched from a detuned to a tuned state. It is thus very important for any new coil design to also have this capability. We have shown in chapter one that it is possible to effectively detune a dielectric resonator with a simple PIN-diode circuit that is very common in RF coil design. The detune capability was a major step forward into using the dielectric resonator technology for human magnetic resonance imaging.

It is also important to be able to fine tune the resonance frequency of a coil. This can be needed in daily practice in order to compensate for different loads but even before that, it is important to have some mechanism to fine tune the resonance frequency of a RF coil on the workbench. This problem becomes even more pertinent if sintered high Q ceramics are used for dielectric resonators. Despite accurate estimation of the mode and thus the needed dielectric constant using electromagnetic simulations, small deviations from the specified dielectric constant and dimensions can sometimes not be avoided due

to imperfections in the production process. As the production of high Q ceramics is a lengthy and costly effort, the facility to be able to fine tune a resonator that is "a couple of MHz off" becomes even more important. As we have shown in chapter two, this is possible by simply changing the boundary condition of the dielectric resonator with an inexpensive copper foil. We have shown that by changing the boundary condition, it is even possible to double, and triple tune a cylindrical DRA. This feature could be for example exploited for double tuned water / fluorine imaging.

To be able to design dielectric resonators as effective RF coils, certain formulas are needed that help the design process. These formulas can be obtained from the literature [13, 19, 28, 32, 35] and work well in the frequency regime for current human MRI. Thus, lengthy trial-and-error builds of coils can be avoided. We were able to show that the empirically derived formulas from dielectric resonators in the GHz range and with much lower permittivity are still valid for much larger dielectric resonators that work in the MHz range. We have also shown in chapters 1, 2 and 3 that these dielectric resonators can be designed using numerical simulations. Especially eigenmode analysis proved to be a quick and reliable tool for the design and field pattern prediction of cylindrical DRAs. While similar results can also be obtained with a time-domain simulation approach using the FDTD [31, 36] method, the eigenmode analysis proved to be much faster producing results in minutes as compared to hours with the FDTD method. Our results should encourage other research groups also to carry out investigation into dielectric resonators as electromagnetic simulation software is nowadays widely available among the ultra-high field magnetic resonance imaging laboratories of the world.

6.1.2. DISCUSSION ON PLASMA BASED RF COILS

In chapter 4 we have described for the first time a novel MRI coil that uses plasma as a conductor. We were able to show that a plasma based RF coil cannot only be used to transmit and excite the spin system but also that it can be used to receive the magnetic resonance signal.

This truly novel concept of an RF coil for magnetic resonance imaging was realized using inexpensive fluorescent lamps. While those have a too high internal gas pressure to be really power efficient at 300 MHz, they are largely abundant in hardware stores all around the world. Other research groups can easily rebuild our designs to start research on this new resonator technology.

Plasma technology offers unique and attractive features that cannot be achieved with conventional lumped element RF coils or dielectric resonator RF coils. The conductor in a plasma coil is the plasma itself. Plasma can be switched on and off as wished for example for the purposes of detuning for reasons mentioned in the last section. The difference here is that while a lumped element coil such as a birdcage resonator or a dielectric resonator can also be detuned, there will always be a physical conductor left. This is unavoidable and undesirable as it alters the receive field and attenuates the gamma rays in case of multi-modal imaging like PET-MRI. A plasma in contrast, if switched off, is physically no longer present. Only the container of the plasma and the gas it contains is present. This will allow for very compact designs of transmit and receive RF coils that are very close to each other.

We were also able to show that the length of which the plasma ignites inside its tube can be adjusted by the input RF power that is also used for ignition of the plasma. This gives an additional degree of freedom to control the extent of the B_1 field. We showed that a simple surfatron can be built that acts simultaneously as a plasma igniter and at the same time as a coupler for the RF into the plasma antenna.

Our experiments show that the fear of increased noise from the plasma leading to no useful MRI at all is unsubstantiated. In fact in theory even lower noise floors than those of metal antennas should be possible if the right plasma configurations are chosen [2].

The efficiency of all plasma experiments conducted so far was lower than when using a conventional RF coil. One should however not forget that the current state of

conventional RF coil design is based on research collated over more than 40 years from all around the world. Also, so far, no efficient coupling to the plasma column has been realized in MRI. We thus can hope for increased efficiency from this new promising coil design.

One first step to increase overall efficiency and usability of plasma MRI coils would be to produce custom plasma columns. These could be made from glass but also certain foams like SynFoam [2] can be used to contain a plasma. These new columns or housings can also have an arbitrary shape. Once manufactured they need to be filled with a suitable gas. One option would be to use atmospheric air and then lower the pressure to allow forming of plasma. The density of the plasma needs to be lower than in current fluorescent light tubes. This would allow the plasma frequency to be steered (also known as Langmuir frequency) into a regime interesting for MRI.

The second step to improve overall efficiency and usability of plasma based MRI coils would be to design, built and test improved coupling schemes to the plasma. Plasma physics is not an entirely new field. In fact, plasma physics research in the twentieth century has produced numerous solutions for this problem [4, 6, 26, 27, 30]. These solutions need to be revised and tested to determine whether they are suitable for MRI.

The third step to improve overall efficiency and usability of plasma coils in MRI would be to look into alternative plasma ignition and mean of sustaining the plasma. We so far used only the transmit pulse as an ignition source. This has so far proven to be not very effective. Perhaps much better results could be achieved if the plasma were to be ignited by another mechanism. Also, here the plasma research of the last century is a vast source for inspiration. One example that was recently published is that DC biased plasma columns can be used as antennas [5]. Also, classical literature can give more hints about how plasma behaves in a strong magnetic field. These results have been published [12] and should be studied to gain insights on how to improve plasma based antenna technology in general and plasma base MRI coils in particular.

Overall, we can conclude that plasma based applications in MRI are in their infancy. The field is now open for a lot of new ideas and solutions to be found. These efforts will hopefully help one day to make MRI and human imaging diagnostics of the future better for all mankind.

6.2. FUTURE DEVELOPMENTS

6.2.1. IMPROVED COUPLING SCHEMES FOR DRAS

While we used an inductive coupling scheme for all our dielectric resonators, numerous other coupling schemes are conceivable and have been described in the literature [11, 13, 19, 32]. The direct coaxial feed is a very interesting application and candidate for an improved coupling scheme. With such a feed, the resonator could be made even more compact, as space for critically coupled loops would be no longer needed. Especially if one considers dense radiative arrays that are made up of DRAs similar to the array of chapter 3, feeding of individual elements via a printed circuit board and micro-striplines might be considered. This would permit thinner arrays to be built.

While in chapters 2 and 3 the dielectric resonator was used to surround the object to be imaged, in chapter 4 an array that works based on TE mode resonators was described. In such an array it is desirable to radiate as efficiently as possible the applied power into the human body in order to increase SNR. The efficiency of such an array could be further optimized by choosing a better suited dielectric permittivity for the resonators. It is conceivable to shrink the resonators to such an extent that one single DRA would have dimensions in the order of a few centimeters. Such resonators could then be placed on a pcb board that is equipped with micro-striplines to couple energy into the DRAs. In this way, a dense high channel count array could be produced similar to that described in [19]. With phase steering using PIN-diode based phase shifters one could imagine that the image quality for cardiac imaging at ultra-high fields could be further improved in the future.

In our research we used exclusively cylindrical DRAs. However, one can essentially use any shape of DRA provided that the mode is suitable for the experiment to be carried out. It is thus conceivable to use very high permittivity (>1000) materials [38] that could be manufactured into thin slabs. This way an even thinner array could be realized having a thickness that approaches the thickness of lumped element circuits. Such a thin DRA could then be used as a substrate for other lumped elements coils, for example a receive array. One could use the DRAs for the high power transmit and the lumped element coil array to receive the MR signal. This way ultra-compact transmit/receive arrays could be realized.

6.2.2. Odd ratio DRAs

Dielectric resonator can be built with odd ratios of height to length when compared to classical MRI coils. For example, in the birdcage resonator, the ratio between length and diameter should be around $\sqrt{2}$. We were able to build such a coil and early results for a simple prototype are given in figure 6.1.

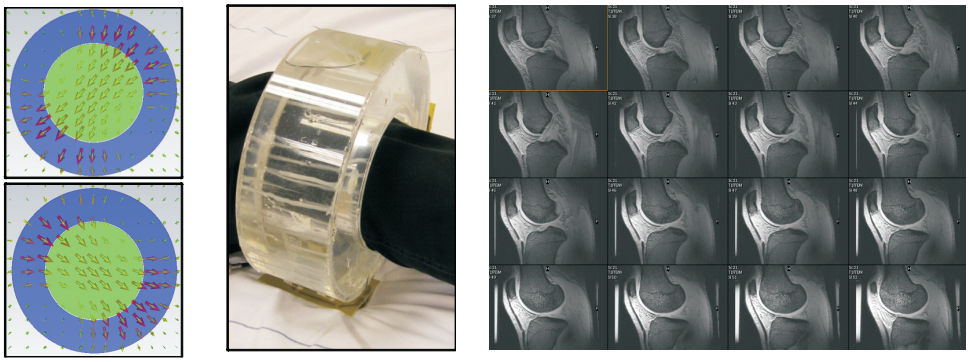


Figure 6.1: Principle of a odd length to diameter ratio dielectric resonator MRI coil: (left)Simulated magnetic field components corresponding to the two frequency degenerate HEM11δ modes resonant at 298.1 MHz. Blue represents the outer annulus filled with water and the green is a homogeneous tissue phantom assigned dielectric properties of tissue. (center) Photograph of the assembled dielectric resonator placed around a volunteer's knee. The two coupling networks can be seen underneath the resonator. (right) A sub-series of adjacent slices from a three-dimensional T1-weighted imaging sequence.

The benefit of such designs could be increased patient comfort while using less space within the MRI bore. Clearly this design needs to be further improved. For example, should the ring be split-able into two half circles, the bottom half could be then put on the patient bed of the MRI system, the knee of a patient would be then placed in the center of this half and thus when the patient would be rested, the top half would be attached. This work shows that odd ratio diameter DRAs are feasible and can be used for MRI as theorized in the discussion of chapter two [3].

6.2.3. HYBRID DRA / PLASMA RF COILS

It is also conceivable to combine dielectric resonators with plasma RF coil technology. One can for example think about nesting plasma columns inside a water based DRA. This would then allow double tuning while perfectly decoupling the two coils from each other. The need for switching circuits will be minimal like shown in chapter 2.

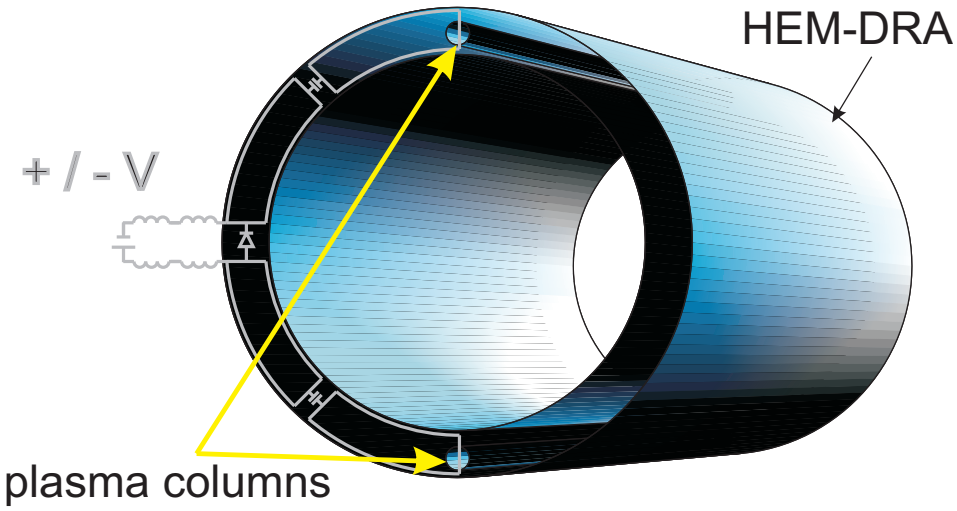


Figure 6.2: Principle of a hybrid plasma / dielectric resonator MRI coil: a DRA using the HEMδ modes is constructed. Within the dielectric resonator plasma columns are nested. In the operation of the DRA for example at proton frequency the plasma is switched off. In order to detune the DRA the plasms is switched to the on stage. Thus, it is also possible to use the plasma columns for excitation of a second frequency, for example phosphor.

We have shown that detuning of a DRA works with the circuit as described in chapter 2. Detuning of the circuit works because the rods shorten the electric field in the HEM resonator. This would also happen if plasma were used as a conductor instead of the copper we used in the experiments of chapter 2. One might speculate that even this simple switching circuit may no longer be needed as the off state of the plasma basically is essentially an open circuit, i.e functioning like the diode in the circuit in figure 6.2.

6.2.4. Silent Plasma Gradient Coils

We have shown in our work in chapter four that plasma can be used as a conductor in MRI to transmit and receive an MR signal. Another possible application for plasma in MRI would be to use it as a conductor in a gradient coil instead of a copper conductor. Gradient coils have basically been constructed in the same way for the last 40 years: a copper conductor is wound around a stiff glass-fiber carrier tube, water cooling pipes are added and the whole package is then immersed in resin and cured. This is needed to provide the necessary stiffness to counteract the massive Lorenz forces that are present during operation of a gradient coil. These forces are also responsible for the characteristic loud noise and banging as well as vibrations inside MRI system [20]. The noise and banging are one major issue with regards to patient comfort and hearing safety for MRI in its current state [7]. Much effort has been put into reducing these effects including putting the gradient coil in a vacuum vessel [14], active noise control [21, 22], using specialized pulse sequences [9] as well as using swept radio frequency [10]. However, all those efforts do not remove the problem but cure some of the symptoms - the vibrations of the gradient coil are still present. Over time those vibrations can cause massive material stress leading to material failure, in best case only the clamps that hold the gradient c

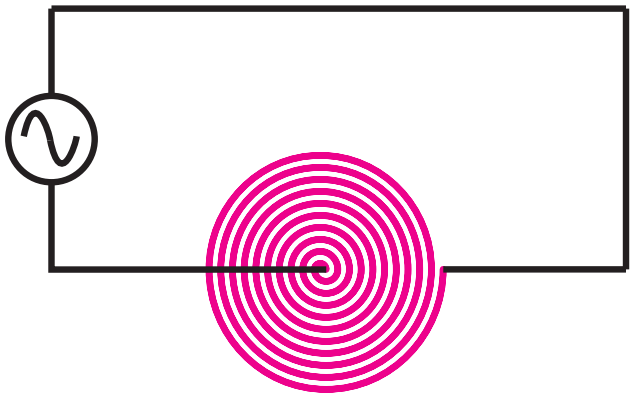


Figure 6.3: Principle of a plasma conductor based gradient coil. The copper conductor is removed and replaced by a plasma conductor.

It might be possible to overcome these unwanted properties of gradient coils if the copper conductor were to be removed and replaced with a plasma guide structure as

illustrated in 6.3. Plasma can handle very high powers (for example millions of amperes are conducted to earth in lightning bolts); theseveral hundred amperes needed for a gradient coil nowadays should not be overly problematic. The Lorenz force will still work upon the plasma; however, one can speculate that much less mass will be moved as the density of the plasma is of course much lower than that of copper metal. If the Lorenz force is significant enough to allow for noise and vibration generation, one could use a trick that would not be possible with a metal conductor to still get a truly silent gradient coil: the Lorenz force will produce a pressure inside the containment filament. This overpressure might be conducted out of the plasma coil into another expansion chamber wherein the pressure could be absorbed by a dampening system. One could consider either a form of silencer or even just an open box with a valve. Such a system would have the added advantage that the plasma ceases to conduct if expanded. This would help to ensure that power is only conducted inside of the plasma gradient coil and not in the expansion /silencer box.

In general, two different designs are conceivable:

1. Ignition on demand with coupled power (gradient wave form) feed over a single surfatron

2. Continuous ignition of the plasma and separate feed of power (gradient wave form)

For the first design a high power surfatron would need to be build. One question that comes to mind for configuration is whether plasma over the whole length of the coil could be switched on and off fast enough. If this should prove not to be possible, design number two provides an alternative. Here the plasma could be pumped and thus sustained with a different frequency than the gradient pulse frequency. This has been previously shown to work for plasma antennas in the MHz regime [34, 39].

6.2.5. Nonlinear Plasma Coils for multi-band MRI

In multi-band MRI the time required for acquisition of the MR image is reduced by exciting not only one slice but at least two slices simultaneously [25]. In order to decode the receive signal it is desirable to have clearly identifiable coil sensitivity profiles. Mostcoils nowadays are built from equal coil elements to from an array. If one would use plasma coils as elements, it would be possible to dynamically alter the coil sensitivity profile for each element by adjusting the amount of ionization of the plasma, for example by driving a single element with more or less power. If the plasma coil were to be used also as a transmit coil, one could dynamically alter the B_1^+ field and thus add a degree of freedom. This behavior was tested experimentally;the results are shown in 6.4.

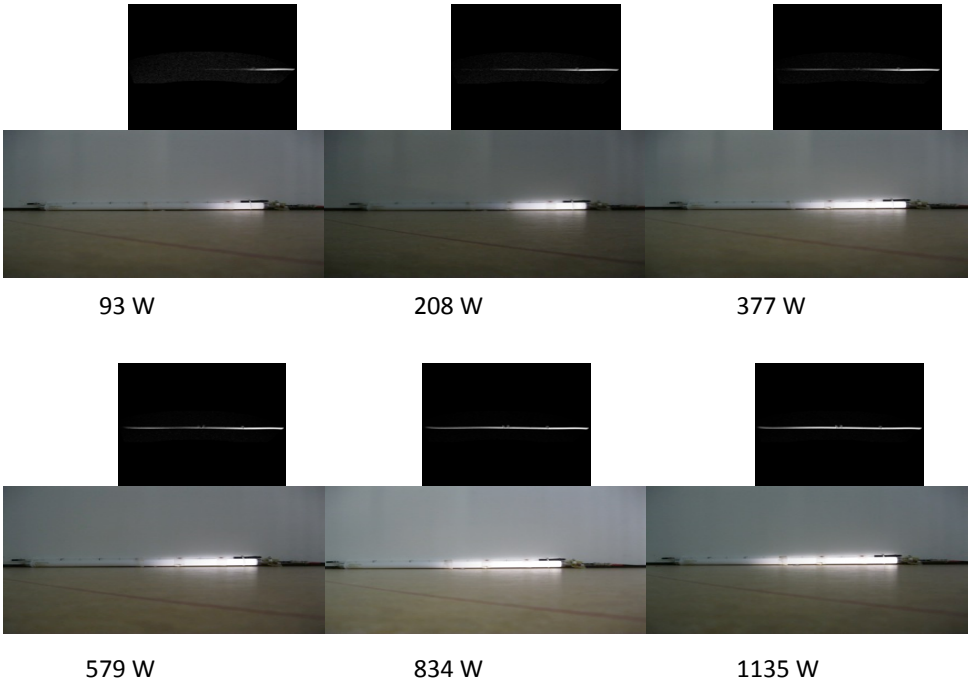


Figure 6.4: Demonstration of non-linear plasma based MRI coils (unpublished data). The plasma coil consists of a fluorescent tube that is connected to the RF transmit power of the MRI scanner via a 50 Ohm line and a surfatron. In order to visualize the extension of the B_1 field a small tube filled with water was attached coaxial to the fluorescent tube. Then different transmit pulses were sent with different power levels ranging from 93 to 1135 Watts. The glow was photographed, and the same experiment repeated with the same powers in the MRI scanner and a very large field of view to cover the entire length of the plasma coil. The length of the visible water phantom corresponds very well to the length of the plasma glow and is thus directly proportional to the applied power.

It is already known from Rayner et al. [34], that the length of a plasma column (argon plasma at 500 MHz) depends on the power applied. They were able to show that the length of the column increases as the square root of the applied RF power. They conclude that these findings will help to design an electronically controllable length that would allow for rapid reconfiguration for different frequencies.

6.2.6. PLASMA BASED RF SHIELDS

RF shielding is usually achieved using copper shields. When using such shields for shielding a coil, the number of eddy currents needs to be minimised to prevent the formation of image artefacts. One interesting property of plasma is that it can be transparent as well as opaque for certain RF frequencies. The plasma frequency can be reconfigured by changing, for example, the pressure inside the plasma coil. If an electromagnetic wave hits a plasma two outcomes are possible, which depend on the frequency of the incident electromagnetic wave and the plasma frequency [17, 18]:

1. If the frequency of the incident ω_i is larger than the plasma frequency ω_p the incident wave will pass through the plasma

2. If the frequency of the incident ω_i is smaller than the plasma frequency ω_p the incident wave will not pass through the plasma

One could use this property of plasmas to build switch-able RF shields like in figure 6.5. Such shields could be used to shield and/or decouple transmit/receive arrays. When the plasma is switched on it provides RF blocking like a conventional copper shield that helps to reduce radiation of power away from the element during transmit. During the receive, the switch can be switched off to improve receive sensitivity of the element. Such a switch-able plasma based RF shield would address the problem of increasing radiation losses of RF coils at higher field strength MRI and also would help to protect body parts that are outside of the field of view from radiation. One could imagine, for example, switch-able shields incorporated into the body coil to reduce SAR in the arms and shoulders.

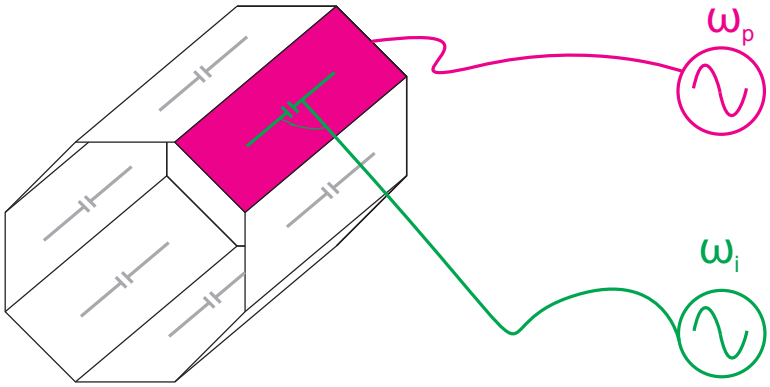


Figure 6.5: Principle of a plasma conductor based RF shielded coil. The copper conductor is removed and replaced by a plasma conductor sheet. The coil would consist of 8 transmit elements with 8 respective plasma shields. Each shield can be switched on individually.

6.2.7. RECONFIGURABLE PLASMA RF COILS

Plasma coils can be reconfigured during operation [1, 15, 16, 23, 29, 33]. One can for example change the gas pressure. By changing the gas pressurethe plasma frequency becomes shifted and thus the optimal noise frequency band. It is thus conceivable to use this feature to build dual tuned coils. One nice feature of a plasma antenna is that it can be switched off. In the off state the conductor completely vanishes, what remains is an space with a low pressure gas. This low-pressure gas has of course a much smaller radiation absorption coefficient than metal. In this way very transparent coils could be build. One could imagine using such a coil for example for PET-MRI or SPECT-MRI.

It might also be possible to drive one and the same plasma coil with two different RF frequencies: simply by using both ends of a plasma tube whereby at one end the surfatron for frequency one (maybe proton), and on the other end the surfatron for frequency two (maybe phosphor), could be excited.

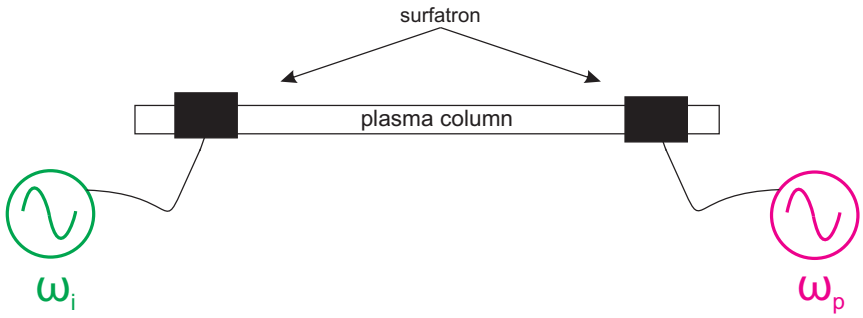


Figure 6.6: Principle of a double tuned plasma MRI coil: a single plasma column is fed be two different frequencies via a separate surfatron for each frequency.

This arrangement is interesting because it has been shown in the literature that a plasma antenna can be pumped. This means that the plasma is produced by a higher frequency RF source igniting the plasma while a lower frequency uses the ignited plasma column as an antenna.

6.2.8. HYBRID PLASMA / LUMPED ELEMENT RF COILS

It is also conceivable to combine established lumped element RF coil technology [24] with a plasma conductor. One could for example make the rungs of a birdcage resonator [8] from plasma conductors. This would then allow for perfect decoupling, For example for making a coil double tuned or for use with a receive array. Switching circuits would be no longer needed, and thus construction of transmit birdcages simplified.

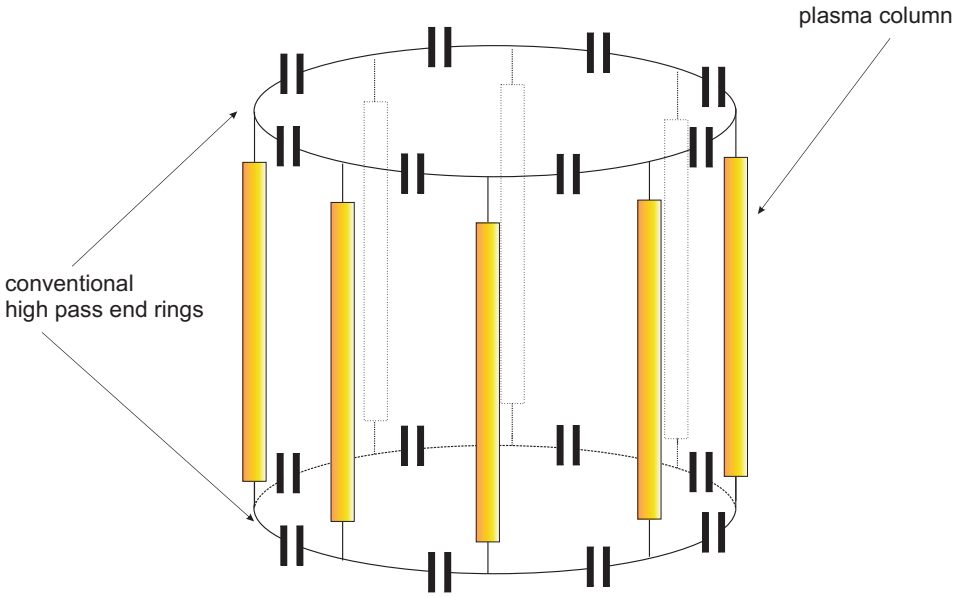


Figure 6.7: Principle of a hybrid plasma / lumped elements birdcage MRI coil: The single rungs of the birdcage are replaced by plasma columns. If the columns are switched on e.g. into the plasma state, the birdcage resonator will work like a conventional lumped elements birdcage. If the plasma in the columns is switched off, the birdcage modes disappear from the RF spectrum: only the modes of the end-rings are still present.

If a birdcage such as shown in figure 6.7 were to be realized it, could be effectively detuned to be used with a receive array when switching the plasma columns off.

6.2.9. DOUBLE TUNED BIRDCAGE COILS

Ifa birdcage as suggested in figure 6.7 were to be built, it could also be used in another interesting way: one could switch on only single legs. In this way, with the same capacitance in the end-rings but a different inductance, other modes of the birdcage resonator on other frequencies could be realized.

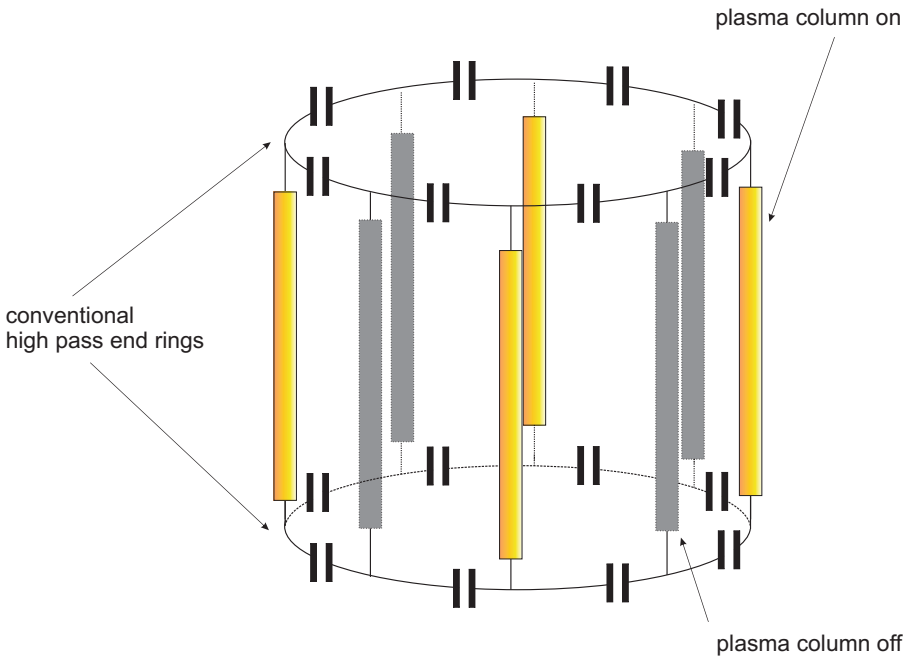


Figure 6.8: Principle of a double tuned hybrid plasma / lumped elements birdcage MRI coil: The single rungs of the birdcage are replaced by plasma columns. The columns can be switched on and off individually e.g. birdcage resonator will work as a four-rung birdcage at one time but can be also switched on to become an eight rung birdcage.

Such a birdcage could use modes that are associated with a small number of switched-on rungs for proton imaging, as there is sufficient signal, and all rungs for e.g. phosphor imaging. Again, such a solution would have the inherent beauty of not needing any detuning circuitry, when one wants to combine such a birdcage with a dedicated receive array.

REFERENCES

[1] I. Alexeff, T. Anderson, E. Farshi, N. Karnam, and N. R. Pulasani. Recent results for plasma antennas. *Physics of Plasmas*, 15(5):057104, 2008.

[2] T. Anderson. *Plasma Antennas*. Artech House, 2011.

[3] S. A. Aussenhofer and A. G. Webb. Design and evaluation of a detunable water-based quadrature hem11 mode dielectric resonator as a new type of volume coil for high field mri. *Magnetic Resonance in Medicine*, 68(4):1325–1331, 2012.

[4] M. Chung, W.-S. Chen, B.-R. Huang, C.-C. Chang, K.-Y. Ku, Y.-H. Yu, and T.-W. Suen. Capacitive coupling return loss of a new pre-ionized monopole plasma antenna. In *TENCON 2007-2007 IEEE Region 10 Conference*, pages 1–4. IEEE, 2007.

[5] M. Chung, W.-S. Chen, Y.-H. Yu, and Z. Y. Liou. Properties of dc-biased plasma antenna. In *Microwave and Millimeter Wave Technology, 2008. ICMMT 2008. International Conference on*, volume 3, pages 1118–1120. IEEE, 2008.

[6] H. Conrads and M. Schmidt. Plasma generation and plasma sources. *Plasma Sources Science and Technology*, 9(4):441, 2000.

[7] S. A. Counter, A. Olofsson, H. Grahn, and E. Borg. Mri acoustic noise: sound pressure and frequency analysis. *Journal of Magnetic Resonance Imaging*, 7(3):606–611, 1997.

[8] C. Hayes, W. Edelstein, J. Schenk, O. Mueller, and M. Eash. An efficient, highly homogeneous radiofrequency coil for whole-body nmr imagingat 1.5t. *Journal of Magnetic Resonance*, 63:662–628, 1985.

[9] F. Hennel, F. Girard, and T. Loenneker. Silent mri with soft gradient pulses. *Magnetic resonance in medicine*, 42(1):6–10, 1999.

[10] D. Idiyatullin, C. Corum, J.-Y. Park, and M. Garwood. Fast and quiet mri using a swept radiofrequency. *Journal of Magnetic Resonance*, 181(2):342–349, 2006.

[11] G. P. Junker, A. A. Kishk, and A. Glisson. Input impedance of dielectric resonator antennas excited by a coaxial probe. *IEEE Transactions on Antennas and Propagation*, 42(7):960–966, 1994.

[12] B. Kadomtsev and O. Pogutse. Electric conductivity of a plasma in a strong magnetic field. *Soviet Journal of Experimental and Theoretical Physics*, 26:1146, 1968.

[13] D. Kajfez. *Dielectric Resonators*. Institution Engineering & Tech, 1998.

[14] A. Katsunuma, H. Takamori, Y. Sakakura, Y. Hamamura, Y. Ogo, and R. Katayama. Quiet mri with novel acoustic noise reduction. *Magnetic Resonance Materials in Physics, Biology and Medicine*, 13(3):139–144, 2001.

[15] R. Kumar and D. Bora. A reconfigurable plasma antenna. *Journal of Applied Physics*, 107(5):053303, 2010.

[16] V. Kumar, M. Mishra, and N. Joshi. Study of a fluorescent tube as plasma antenna. *Progress in electromagnetics research letters*, 24:17–26, 2011.

[17] M. Laroussi and W. T. Anderson. Attenuation of electromagnetic waves by a plasma layer at atmospheric pressure. *International journal of infrared and millimeter waves*, 19(3):453–464, 1998.

[18] M. Laroussi and J. R. Roth. Numerical calculation of the reflection, absorption, and transmission of microwaves by a nonuniform plasma slab. *IEEE Transactions on Plasma Science*, 21(4):366–372, 1993.

[19] K. Luk. *Dielectric Resonator Antennas*. Research Studies Press Ltd., 2003.

[20] P. Mansfield, P. M. Glover, and J. Beaumont. Sound generation in gradient coil structures for mri. *Magnetic resonance in medicine*, 39(4):539–550, 1998.

[21] P. Mansfield, B. Haywood, and R. Coxon. Active acoustic control in gradient coils for mri. *Magnetic resonance in medicine*, 46(4):807–818, 2001.

[22] M. McJury, R. Stewart, D. Crawford, and E. Torna. The use of active noise control (anc) to reduce acoustic noise generated during mri scanning: Some initial results. *Magnetic Resonance Imaging*, 15:319–322, 1997.

[23] C. Metz. Reconfigurable plasma antenna with interconnected gas enclosures, Dec. 5 2006. US Patent 7,145,512.

[24] J. Mispelter. *NMR Probeheads for Biophysical and Biomedical Experiments: Theoretical Principles and Practical Guidelines: Theoretical Principles and Practical Guidelines*. Imperial College Press, 2015.

[25] S. Moeller, E. Yacoub, C. A. Olman, E. Auerbach, J. Strupp, N. Harel, and K. Uğurbil. Multiband multislice ge-epi at 7 tesla, with 16-fold acceleration using partial parallel imaging with application to high spatial and temporal whole-brain fmri. *Magnetic Resonance in Medicine*, 63(5):1144–1153, 2010.

[26] M. Moisan, M. Chaker, Z. Zakrzewski, and J. Paraszczak. The waveguide surfatron: a high power surface-wave launcher to sustain large-diameter dense plasma columns. *Journal of Physics E: Scientific Instruments*, 20(11):1356, 1987.

[27] M. Moisan, Z. Zakrzewski, and R. Pantel. The theory and characteristics of an efficient surface wave launcher (surfatron) producing long plasma columns. *Journal of physics D: Applied physics*, 12(2):219, 1979.

[28] R. K. Mongia and P. Bhartia. Dielectric resonator antennas. a review and general design relations for resonant frequency and bandwidth. *International Journal of Microwave and Millimeter-Wave Computer-Aided Engineering*, 4(3):230–247, 1994.

[29] E. G. Norris, T. Anderson, and I. Alexeff. Reconfigurable plasma antenna, Apr. 9 2002. US Patent 6,369,763.

[30] H. Nowakowska, Z. Zakrzewski, and M. Moisan. Propagation characteristics of electromagnetic waves along a dense plasma filament. *Journal of Physics D: Applied Physics*, 34(10):1474, 2001.

[31] S. O Keefe, S. Kingsley, and S. Saario. Fdtd simulation of radiation characteristics of half-volume hem- and te-mode dielectric resonator antennas. *IEEE Transactions on Antennas and Propagation*, 50(2):175–179, 2002.

[32] A. Petosa. *Dielectric Resonator Antenna Handbook*. Artech House Publishers, 2007.

[33] M. Pourbagher, J. Nourinia, and N. Pourmahmud. Reconfigurable plasma antennas. *Indian Journal of Science and Technology*, 5(6):2928–2932, 2012.

[34] J. P. Rayner, A. P. Whichello, and A. D. Cheetham. Physical characteristics of plasma antennas. *IEEE Transactions on plasma science*, 32(1):269–281, 2004.

[35] J. Sethares and S. Naumann. Design of microwave dielectric resonators. *IEEE Transactions on Microwave Theory and Techniques*, 14(1):2–7, 1966.

[36] S.-M. Shum and K.-M. Luk. Fdtd analysis of probe-fed cylindrical dielectric resonator antenna. *IEEE Transactions on Antennas and Propagation*, 46(3):325–333, 1998.

[37] H. Wen, F. A. Jaffer, T. J. Denison, S. Duewell, A. S. Chesnick, and R. S. Balaban. The evaluation of dielectric resonators containing h_2o or d_2o as rf coils for high-field mr imaging and spectroscopy. *Journal of Magnetic Resonance, Series B*, 110(2):117–123, 1996.

[38] A. R. West, T. B. Adams, F. D. Morrison, and D. C. Sinclair. Novel high capacitance materials:-batio 3: La and cacu 3 ti 4 o 12. *Journal of the European Ceramic Society*, 24(6):1439–1448, 2004.

[39] A. Zhu, Z. Chen, J. Lv, and J. Liu. Characteristics of ac-biased plasma antenna and plasma antenna excited by surface wave. *Journal of Electromagnetic Analysis and Applications*, 4(7):279–284, 2012.

7

Acknowledgements

7

FIRST I have to thank Prof. Dr. A.G. Webb. Dear Andrew, thanks a lot for the opportunity to do my Ph.D. at the C.J. Gorter Center. I have to thank you for excellent guidance throughout the past years. I also have to be thankful for the wonderful work environment that was provided by you. Also the chance to go for my own ideas and scientific freedom was something that I enjoyed tremendously.

I furthermore have to thank Prof. Dr. Itamar Ronen for providing good talks on the weekends in the laboratory. Also his steady stream of excellent espresso helped a lot to keep this thesis going.

I also have to thank my all my colleagues and co-workers at the Gorter Center that are not named here. I have to thank Nathalie Dorenweerd for distractions from work and regular visits to the swimming hall. Ece Ercan has helped out often in the weekend as a volunteer and was also a good conversation partner on Sunday afternoons. XingXing Zhang was a very pleasant room mate, a helpful volunteer and a very good scout for fine Chinese foods at numerous occasions. Eidrees Ghariq was also a very pleasant and polite room mate, a good chatting partner and volunteer. Last but not last Mathijs Buijs also was there to lighten the mood in our office room. Special thanks go to Dana and Robert Poole and her family for many nice dinners and BBQs in the summers as well as proof reading of this thesis.

Not all my wishes in power tools could be fulfilled, my own lathe for example. As the capacity of the hospital's tool shop was soon exceeded by my various projects we had to outsource them to a local prototype machining tool-shop: Mascal Design, Leiden. It was in here in Marcel's tool-shop were lots of my ideas took physical shape in many late night and weekend sessions. Without the professional help of Marcel van Schie many of my projects, that are not described in this thesis, would not have been possible like for example the 7 T sodium knee coil for Paul de Bruin.

Speaking of Paul de Bruin: I have to thank you for countless hours in the weekends in the laboratory building coils and listening to good music. I really enjoyed those sessions.

Another builder by heart is Wouter Teeuwisse. He gave very valuable input into the mechanical parts of my project and was always a good room mate at various conferences.

I also would like to thank Dr. Ted Anderson and Fred Dyer from Haleakala Industries

for their excellent support of project THOR. Their input was very valuable in getting the plasma experiments going.

I would like to thank the two paranymphs Wouter and Dana for all their work and help.

Finally I have to thank my family. When this thesis started it consisted of my parents Otto and Ilse Aussenhofer as well as my brother Michael Aussenhofer. Without their support I would have not been able to make this journey. Now, I have my own family: my dear wife Changjuan and our lovely daughter Annika. Without your support and continuous motivation this work would not have been possible.

8

BIBLIOGRAPHY

REFERENCES

[1] G. Adriany, V. de Moortele, F. Wiesinger, S. Moeller, J. P. Strupp, P. Andersen, C. Snyder, X. Zhang, W. Chen, K. P. Pruessmann, et al. Transmit and receive transmission line arrays for 7 tesla parallel imaging. *Magnetic resonance in medicine*, 53(2):434–445, 2005.

[2] V. Agranovich and D. Mills. Surface polaritons: electromagnetic waves at surfaces and interfaces. *Journal of the Optical Society of America B Optical Physics*, 1:410, 1984.

[3] I. Alexeff, T. Anderson, E. Farshi, N. Karnam, and N. R. Pulasani. Recent results for plasma antennas. *Physics of Plasmas*, 15(5):057104, 2008.

[4] T. Anderson. *Plasma Antennas*. Artech House, 2011.

[5] G. Annino, M. Cassettari, I. Longo, M. Martinelli, P. Van Bentum, and E. Van der Horst. A novel probe head for high-field, high-frequency electron paramagnetic resonance. *Review of scientific instruments*, 70(3):1787–1793, 1999.

[6] G. Annino, M. Cassettari, M. Martinelli, and P. Van Bentum. A nonradiative approach to single-mode dielectric resonators. *Applied Magnetic Resonance*, 24(2):157–175, 2003.

[7] S. Aussenhofer and A. Webb. High-permittivity solid ceramic resonators for high-field human mri. *NMR in Biomedicine*, 26(11):1555–1561, 2013.

[8] S. Aussenhofer and A. Webb. An eight-channel transmit/receive array of te 01 mode high permittivity ceramic resonators for human imaging at 7t. *Journal of Magnetic Resonance*, 243:122–129, 2014.

[9] S. A. Aussenhofer and A. G. Webb. Design and evaluation of a detunable water-based quadrature hem11 mode dielectric resonator as a new type of volume coil for high field mri. *Magnetic Resonance in Medicine*, 68(4):1325–1331, 2012.

[10] P. Bellan. *Fundamentals of plasma physics*. Cambridge University Press, 2006.

[11] F. Bloch. Nuclear induction. *Physical review*, 70(7-8):460, 1946.

[12] G. Borg, J. Harris, N. Martin, D. Thorncraft, R. Milliken, D. Miljak, B. Kwan, T. Ng, and J. Kircher. Plasmas as antennas: Theory, experiment and applications. *Physics of Plasmas (1994-present)*, 7(5):2198–2202, 2000.

[13] G. Borg, J. Harris, D. Miljak, and N. Martin. Application of plasma columns to radiofrequency antennas. *Applied physics letters*, 74(22):3272–3274, 1999.

[14] D. O. Brunner, N. De Zanche, J. Fröhlich, J. Paska, and K. P. Pruessmann. Travelling-wave nuclear magnetic resonance. *Nature*, 457(7232):994–998, 2009.

[15] I. I. Burykin, S. Levitskii, and V. Martynenko. The radiation of electromagnetic waves by a variable cross section cylindrical plasma waveguide. *Radio Engineering and Electronic Physics*, 20:86–91, 1975.

[16] A. Christ, W. Kainz, E. G. Hahn, K. Honegger, M. Zefferer, E. Neufeld, W. Rascher, R. Janka, W. Bautz, J. Chen, et al. The virtual family—development of surface-based anatomical models of two adults and two children for dosimetric simulations. *Physics in medicine and biology*, 55(2):N23, 2010.

[17] M. Chung, W.-S. Chen, B.-R. Huang, C.-C. Chang, K.-Y. Ku, Y.-H. Yu, and T.-W. Suen. Capacitive coupling return loss of a new pre-ionized monopole plasma antenna. In *TENCON 2007-2007 IEEE Region 10 Conference*, pages 1–4. IEEE, 2007.

[18] M. Chung, W.-S. Chen, Y.-H. Yu, and Z. Y. Liou. Properties of dc-biased plasma antenna. In *Microwave and Millimeter Wave Technology, 2008. ICMMT 2008. International Conference on*, volume 3, pages 1118–1120. IEEE, 2008.

[19] C. M. Collins, W. Liu, W. Schreiber, Q. X. Yang, and M. B. Smith. Central brightening due to constructive interference with, without, and despite dielectric resonance. *Journal of Magnetic Resonance Imaging*, 21(2):192–196, 2005.

[20] H. Conrads and M. Schmidt. Plasma generation and plasma sources. *Plasma Sources Science and Technology*, 9(4):441, 2000.

[21] S. A. Counter, A. Olofsson, H. Grahn, and E. Borg. Mri acoustic noise: sound pressure and frequency analysis. *Journal of Magnetic Resonance Imaging*, 7(3):606–611, 1997.

[22] W. Crookes. On a fourth state of matter. *Proceedings of the Royal Society of London*, 30(200-205):469–472, 1879.

[23] P. Daleiden, M.-A. Golombeck, S. Junge, and O. Dössel. Development and characterisation of a ceramic hf-resonator for the mr-tomography. *Biomedizinische Technik/Biomedical Engineering*, 47(s1b):758–761, 2002.

[24] M. A. Dieringer, W. Renz, T. Lindel, F. Seifert, T. Frauenrath, F. von Knobelsdorff-Brenkenhoff, H. Waiczies, W. Hoffmann, J. Rieger, H. Pfeiffer, et al. Design and application of a four-channel transmit/receive surface coil for functional cardiac imaging at 7t. *Journal of Magnetic Resonance Imaging*, 33(3):736–741, 2011.

[25] O. Dietrich, M. F. Reiser, and S. O. Schoenberg. Artifacts in 3-t mri: physical background and reduction strategies. *European journal of radiology*, 65(1):29–35, 2008.

[26] E. Eriksen, M.-A. Golombeck, S. Junge, and O. Dössel. Simulation of a birdcage and a ceramic cavity hf-resonator for high magnetic fields in magnetic resonance imaging. *Biomedizinische Technik/Biomedical Engineering*, 47(s1b):754–757, 2002.

[27] W. Froncisz and J. S. Hyde. The loop-gap resonator: a new microwave lumped circuit esr sample structure. *Journal of Magnetic Resonance (1969)*, 47(3):515–521, 1982.

[28] U. Gersch and A. Loesche. Untersuchungen der paramagnetischen kernresonanzabsorption im kondensatorfeld. *Annals of Physics*, 455(1-6):167–172, 1957.

[29] A. Graessl, W. Renz, F. Hezel, M. A. Dieringer, L. Winter, C. Oezerdem, J. Rieger, P. Kellman, D. Santoro, T. D. Lindel, et al. Modular 32-channel transceiver coil array for cardiac mri at 7.0 t. *Magnetic Resonance in Medicine*, 72(1):276–290, 2014.

[30] J. Griffiths. *Introduction to Electrodynamics*. Prentice Hall, 1999.

[31] E. Haacke, R. Brown, M. Thompson, and R. Venkatesan. *Magnetic Resonance Imaging: Physical Principles and Sequence Design*. John Wiley & Sons, 1999.

[32] K. Haines, T. Neuberger, M. Lanagan, E. Semouchkina, and A. Webb. High q calcium titanate cylindrical dielectric resonators for magnetic resonance microimaging. *Journal of Magnetic Resonance*, 200(2):349–353, 2009.

[33] J. Harry. *Introduction to Plasma Technology*. Wiley-VCH, 2010.

[34] C. Hayes, W. Edelstein, J. Schenk, O. Mueller, and M. Eash. An efficient, highly homogeneous radiofrequency coil for whole-body nmr imagingat 1.5t. *Journal of Magnetic Resonance*, 63:662–628, 1985.

[35] F. Hennel, F. Girard, and T. Loenneker. Silent mri with soft gradient pulses. *Magnetic resonance in medicine*, 42(1):6–10, 1999.

[36] F. Hezel, C. Thalhammer, S. Waiczies, J. Schulz-Menger, and T. Niendorf. High spatial resolution and temporally resolved t 2* mapping of normal human myocardium at 7.0 tesla: an ultrahigh field magnetic resonance feasibility study. *PLoS ONE*, 7:12, 2012.

[37] P. Hofmann. *Solid State Physics: An Introduction*. Wiley-VCH, 2008.

[38] J. Hu and C. R. Menyuk. Understanding leaky modes: slab waveguide revisited. *Advances in Optics and Photonics*, 1(1):58–106, 2009.

[39] D. Idiyatullin, C. Corum, J.-Y. Park, and M. Garwood. Fast and quiet mri using a swept radiofrequency. *Journal of Magnetic Resonance*, 181(2):342–349, 2006.

[40] IEEE. Ieee standard c95.3 recommended practice for measurements and computations of radio frequency electromagnetic fields with respect to human exposure to such fields, 100 khz-300 mhz., 2008.

[41] U. Inan and A. Golkowski. *Principles of Plasma Physics for Engineers and Scientists*. Cambridge University Press, 2011.

[42] Int. Soc. Magn. Reson. Med. *J.Y. Lu, X. Zhang, B.K. Rutt, A novel 7 T transmit array using TE01d mode dielectric resonators*, 2013.

[43] O. Ipek, A. Raaijmakers, J. Lagendijk, P. Luijten, and C. van den Berg. Optimization of the radiative antenna for 7-t magnetic resonance body imaging. *Concepts in Magnetic Resonance Part B: Magnetic Resonance Engineering*, 43(1):1–10, 2013.

[44] J. Jackson. *Classical Electrodynamics*. Wiley, 1962.

[45] M. Jaworski and M. W. Pospieszalski. An accurate solution of the cylindrical dielectric resonator problem. *Microwave Theory and Techniques, IEEE Transactions on*, 27(7):639–643, 1979.

[46] G. P. Junker, A. A. Kishk, and A. Glisson. Input impedance of dielectric resonator antennas excited by a coaxial probe. *IEEE Transactions on Antennas and Propagation*, 42(7):960–966, 1994.

[47] B. Kadomtsev and O. Pogutse. Electric conductivity of a plasma in a strong magnetic field. *Soviet Journal of Experimental and Theoretical Physics*, 26:1146, 1968.

[48] D. Kajfez. *Dielectric Resonators*. Institution Engineering & Tech, 1998.

[49] D. Kajfez, A. W. Glisson, and J. James. Computed modal field distributions for isolated dielectric resonators. *IEEE transactions on Microwave Theory and Techniques*, 32(12):1609–1616, 1984.

[50] A. Katsunuma, H. Takamori, Y. Sakakura, Y. Hamamura, Y. Ogo, and R. Katayama. Quiet mri with novel acoustic noise reduction. *Magnetic Resonance Materials in Physics, Biology and Medicine*, 13(3):139–144, 2001.

[51] A. Khanna. Review of dielectric resonator oscillator technology. In *1987 IEEE International Frequency Control Symposium Proceedings*, pages 478–486, 1987.

[52] A. Kishk, A. Glisson, and G. Junker. Bandwidth enhancement for split cylindrical dielectric resonator antennas. *Progress In Electromagnetics Research*, 33:97–118, 2001.

[53] W. Koning, J. Bluemink, E. Langenhuizen, A. Raaijmakers, A. Andreychenko, C. den Berg, P. Luijten, J. Zwanenburg, and D. Klomp. High-resolution mri of the carotid arteries using a leaky waveguide transmitter and a high-density receive array at 7 t. *Magnetic Resonance in Medicine*, 69(4):1186–1193, 2013.

[54] O. Kraff, A. K. Bitz, T. Breyer, S. Kruszona, S. Maderwald, I. Brote, E. R. Gizewski, M. E. Ladd, and H. H. Quick. A transmit/receive radiofrequency array for imaging the carotid arteries at 7 tesla: coil design and first in vivo results. *Investigative radiology*, 46(4):246–254, 2011.

[55] R. Kumar and D. Bora. A reconfigurable plasma antenna. *Journal of Applied Physics*, 107(5):053303, 2010.

[56] V. Kumar, M. Mishra, and N. Joshi. Study of a fluorescent tube as plasma antenna. *Progress in electromagnetics research letters*, 24:17–26, 2011.

[57] M. Laroussi and W. T. Anderson. Attenuation of electromagnetic waves by a plasma layer at atmospheric pressure. *International journal of infrared and millimeter waves*, 19(3):453–464, 1998.

[58] M. Laroussi and J. R. Roth. Numerical calculation of the reflection, absorption, and transmission of microwaves by a nonuniform plasma slab. *IEEE Transactions on Plasma Science*, 21(4):366–372, 1993.

[59] P. C. Lauterbur. Image formation by induced local interactions: examples employing nuclear magnetic resonance. *Nature*, 1973.

[60] K. Luk. *Dielectric Resonator Antennas*. Research Studies Press Ltd., 2003.

[61] P. Mansfield. Multi-planar image formation using nmr spin echoes. *Journal of Physics C: Solid State Physics*, 10(3):L55, 1977.

[62] P. Mansfield, P. M. Glover, and J. Beaumont. Sound generation in gradient coil structures for mri. *Magnetic resonance in medicine*, 39(4):539–550, 1998.

[63] P. Mansfield, B. Haywood, and R. Coxon. Active acoustic control in gradient coils for mri. *Magnetic resonance in medicine*, 46(4):807–818, 2001.

[64] S. M. Mattar and S. Y. ElNaggar. Analysis of two stacked cylindrical dielectric resonators in a te 102 microwave cavity for magnetic resonance spectroscopy. *Journal of Magnetic Resonance*, 209(2):174–182, 2011.

[65] M. McJury, R. Stewart, D. Crawford, and E. Torna. The use of active noise control (anc) to reduce acoustic noise generated during mri scanning: Some initial results. *Magnetic Resonance Imaging*, 15:319–322, 1997.

[66] C. Metz. Reconfigurable plasma antenna with interconnected gas enclosures, Dec. 5 2006. US Patent 7,145,512.

[67] G. J. Metzger, C. Snyder, C. Akgun, T. Vaughan, K. Ugurbil, V. de Moortele, et al. Local b1+ shimming for prostate imaging with transceiver arrays at 7t based on subject-dependent transmit phase measurements. *Magnetic Resonance in Medicine*, 59(2):396–409, 2008.

[68] J. Mispelter. *NMR Probeheads for Biophysical and Biomedical Experiments: Theoretical Principles and Practical Guidelines: Theoretical Principles and Practical Guidelines*. Imperial College Press, 2015.

[69] S. Moeller, E. Yacoub, C. A. Olman, E. Auerbach, J. Strupp, N. Harel, and K. Uğurbil. Multiband multislice ge-epi at 7 tesla, with 16-fold acceleration using partial parallel imaging with application to high spatial and temporal whole-brain fmri. *Magnetic Resonance in Medicine*, 63(5):1144–1153, 2010.

[70] M. Moisan, M. Chaker, Z. Zakrzewski, and J. Paraszczak. The waveguide surfatron: a high power surface-wave launcher to sustain large-diameter dense plasma columns. *Journal of Physics E: Scientific Instruments*, 20(11):1356, 1987.

[71] M. Moisan, A. Shivarova, and A. Trivelpiece. Experimental investigations of the propagation of surface waves along a plasma column. *Plasma physics*, 24(11):1331, 1982.

[72] M. Moisan and Z. Zakrzewski. Plasma sources based on the propagation of electromagnetic surface waves. *Journal of Physics D: Applied Physics*, 24(7):1025, 1991.

[73] M. Moisan, Z. Zakrzewski, and R. Pantel. The theory and characteristics of an efficient surface wave launcher (surfatron) producing long plasma columns. *Journal of physics D: Applied physics*, 12(2):219, 1979.

[74] R. K. Mongia and P. Bhartia. Dielectric resonator antennas. a review and general design relations for resonant frequency and bandwidth. *International Journal of Microwave and Millimeter-Wave Computer-Aided Engineering*, 4(3):230–247, 1994.

[75] T. Neuberger, V. Tyagi, E. Semouchkina, M. Lanagan, A. Baker, K. Haines, and A. Webb. Design of a ceramic dielectric resonator for nmr microimaging at 14.1 tesla. *Concepts in Magnetic Resonance Part B: Magnetic Resonance Engineering*, 33(2):109–114, 2008.

[76] A. Neufeld, N. Landsberg, and A. Boag. Dielectric inserts for sensitivity and rf magnetic field enhancement in nmr volume coils. *Journal of Magnetic Resonance*, 200(1):49–55, 2009.

[77] T. Niendorf, A. Graessl, C. Thalhammer, M. A. Dieringer, O. Kraus, D. Santoro, K. Fuchs, F. Hezel, S. Waiczies, B. Ittermann, et al. Progress and promises of human cardiac magnetic resonance at ultrahigh fields: a physics perspective. *Journal of Magnetic Resonance*, 229:208–222, 2013.

[78] E. G. Norris, T. Anderson, and I. Alexeff. Reconfigurable plasma antenna, Apr. 9 2002. US Patent 6,369,763.

[79] H. Nowakowska, Z. Zakrzewski, and M. Moisan. Propagation characteristics of electromagnetic waves along a dense plasma filament. *Journal of Physics D: Applied Physics*, 34(10):1474, 2001.

[80] S. O Keefe, S. Kingsley, and S. Saario. Fdtd simulation of radiation characteristics of half-volume hem- and te-mode dielectric resonator antennas. *IEEE Transactions on Antennas and Propagation*, 50(2):175–179, 2002.

[81] OECD. *Health at a glance 2015: OECD Indicators*. OECD Publishing, 2015.

[82] A. Okaya and L. Barash. The dielectric microwave resonator. *Proceedings of the IRE*, 50(10):2081–2092, 1962.

[83] A. Petosa. *Dielectric Resonator Antenna Handbook*. Artech House Publishers, 2007.

[84] M. Pourbagher, J. Nourinia, and N. Pourmahmud. Reconfigurable plasma antennas. *Indian Journal of Science and Technology*, 5(6):2928–2932, 2012.

[85] D. Pozar. *Microwave Engineering*. Wiley, 2011.

[86] E. M. Purcell, H. Torrey, and R. V. Pound. Resonance absorption by nuclear magnetic moments in a solid. *Physical review*, 69(1-2):37, 1946.

[87] A. Raaijmakers and C. Berg. Antennas as surface array elements for body imaging at ultrahigh field strengths. *eMagRes*, 2012.

[88] A. Raaijmakers, O. Ipek, D. Klomp, C. Possanzini, P. Harvey, J. Lagendijk, and C. Van den Berg. Design of a radiative surface coil array element at 7 t: The single-side adapted dipole antenna. *Magnetic Resonance in Medicine*, 66(5):1488–1497, 2011.

[89] A. Raaijmakers, P. Luijten, and C. Berg. Dipole antennas for ultrahigh-field body imaging: a comparison with loop coils. *NMR in Biomedicine*, 2015.

[90] H. Rahbar, S. C. Partridge, W. B. DeMartini, B. Thursten, and C. D. Lehman. Clinical and technical considerations for high quality breast mri at 3 tesla. *Journal of Magnetic Resonance Imaging*, 37(4):778–790, 2013.

[91] J. P. Rayner, A. P. Whichello, and A. D. Cheetham. Physical characteristics of plasma antennas. *IEEE Transactions on plasma science*, 32(1):269–281, 2004.

[92] T. Redpath. Signal-to-noise ratio in mri. *The British Journal of Radiology*, 71(847):704–707, 1998.

[93] R. Richtmyer. Dielectric resonators. *Journal of Applied Physics*, 10(6):391–398, 1939.

[94] M. Rogalski and S. Palmer. *Solid State Physics*. Gordon and Breach Science Publishers, 2000.

[95] F. S and A. JELENSKI. Influence of conducting walls on resonant frequencies of dielectric microwave resonator, 1971.

[96] O. Sager and F. Tisi. On eigenmodes and forced resonance-modes of dielectric spheres. *Proceedings of the IEEE*, 56(9):1593–1594, 1968.

[97] J. Sethares and S. Naumann. Design of microwave dielectric resonators. *IEEE Transactions on Microwave Theory and Techniques*, 14(1):2–7, 1966.

[98] A. Shivarova and I. Zhelyazkov. Surface waves in a homogeneous plasma sharply bounded by a dielectric. *Plasma Physics*, 20(10):1049, 1978.

[99] S.-M. Shum and K.-M. Luk. Fdtd analysis of probe-fed cylindrical dielectric resonator antenna. *IEEE Transactions on Antennas and Propagation*, 46(3):325–333, 1998.

[100] A. Sihvola. Mixing rules with complex dielectric coefficients. *Subsurface Sensing Technologies and Applications*, 1(4):393–415, 2000.

[101] J. E. M. Snaar, W. M. Teeuwisse, M. J. Versluis, M. A. van Buchem, H. E. Kan, N. B. Smith, and A. G. Webb. Improvements in high-field localized mrs of the medial temporal lobe in humans using new deformable high-dielectric materials. *NMR in biomedicine*, 24(7):873–9, aug 2011.

[102] C. Snyder, L. DelaBarre, G. Metzger, P.-F. van de Moortele, C. Akgun, K. Ugurbil, and J. Vaughan. Initial results of cardiac imaging at 7 tesla. *Magnetic resonance in Medicine*, 61(3):517–524, 2009.

[103] C. Snyder, L. DelaBarre, S. Moeller, J. Tian, C. Akgun, P.-F. Van de Moortele, P. Bolan, K. Ugurbil, J. Vaughan, and G. Metzger. Comparison between eight-and sixteen-channel tem transceive arrays for body imaging at 7 t. *Magnetic Resonance in Medicine*, 67(4):954–964, 2012.

[104] B. J. Soher, B. M. Dale, and E. M. Merkle. A review of mr physics: 3t versus 1.5 t. *Magnetic resonance imaging clinics of North America*, 15(3):277–290, 2007.

[105] W. Teeuwisse, W. Brink, K. Haines, and A. Webb. Simulations of high permittivity materials for 7 t neuroimaging and evaluation of a new barium titanate-based dielectric. *Magnetic Resonance in Medicine*, 67(4):912–918, 2012.

[106] C. Thalhammer, W. Renz, L. Winter, F. Hezel, J. Rieger, H. Pfeiffer, A. Graessl, F. Seifert, W. Hoffmann, F. von Knobelsdorff-Brenkenhoff, et al. Two-dimensional sixteen channel transmit/receive coil array for cardiac mri at 7.0 t: Design, evaluation, and application. *Journal of Magnetic Resonance Imaging*, 36(4):847–857, 2012.

[107] L. Tonks and I. Langmuir. Oscillations in ionized gases. *Physical Review*, 33(2):195, 1929.

[108] A. Trivelpiece and R. Gould. Space charge waves in cylindrical plasma columns. *Journal of Applied Physics*, 30(11):1784–1793, 1959.

[109] K. Uchino. Glory of piezoelectric perovskites. *Science and Technology of Advanced Materials*, 2016.

[110] S. G. van Elderen, M. J. Versluis, A. G. Webb, J. J. Westenberg, J. Doornbos, N. B. Smith, A. de Roos, and M. Stuber. Initial results on in vivo human coronary mr angiography at 7 t. *Magnetic Resonance in Medicine*, 62(6):1379–1384, 2009.

[111] S. G. van Elderen, M. J. Versluis, J. J. Westenberg, H. Agarwal, N. B. Smith, M. Stuber, A. de Roos, and A. G. Webb. Right coronary mr angiography at 7 t: A direct quantitative and qualitative comparison with 3 t in young healthy volunteers 1. *Radiology*, 257(1):254–259, 2010.

[112] P. Van Musschenbroek. *Essai de physique*, volume 2. Chez Samuel Luchtmans, Imprimeur de l'Université, 1751.

[113] T. Vanderah. Talking Ceramics. *Science*, 298(5596):1182–1184, 2002.

[114] J. Vaughan, G. Adriany, C. Snyder, J. Tian, T. Thiel, L. Bolinger, H. Liu, L. DelaBarre, and K. Ugurbil. Efficient high-frequency body coil for high-field mri. *Magnetic resonance in medicine*, 52(4):851–859, 2004.

[115] J. T. Vaughan, H. P. Hetherington, J. O. Otu, J. W. Pan, and G. M. Pohost. High frequency volume coils for clinical nmr imaging and spectroscopy. *Magnetic Resonance in Medicine*, 32(2):206–218, 1994.

[116] J. T. Vaughan, C. J. Snyder, L. J. DelaBarre, P. J. Bolan, J. Tian, L. Bolinger, G. Adriany, P. Andersen, J. Strupp, and K. Ugurbil. Whole-body imaging at 7t: Preliminary results. *Magnetic resonance in Medicine*, 61(1):244–248, 2009.

[117] F. von Knobelsdorff-Brenkenhoff, T. Frauenrath, M. Prothmann, M. A. Dieringer, F. Hezel, W. Renz, K. Kretschel, T. Niendorf, and J. Schulz-Menger. Cardiac chamber quantification using magnetic resonance imaging at 7 tesla—a pilot study. *European radiology*, 20(12):2844–2852, 2010.

[118] F. von Knobelsdorff-Brenkenhoff, V. Tkachenko, L. Winter, J. Rieger, C. Thalhammer, F. Hezel, A. Graessl, M. A. Dieringer, T. Niendorf, and J. Schulz-Menger. Assessment of the right ventricle with cardiovascular magnetic resonance at 7 tesla. *J Cardiovasc Magn Reson*, 15(23):10–1186, 2013.

[119] A. Webb. Visualization and characterization of pure and coupled modes in water-based dielectric resonators on a human 7t scanner. *Journal of Magnetic Resonance*, 216:107–113, 2012.

[120] A. Webb, N. Smith, S. Aussenhofer, and H. Kan. Use of tailored higher modes of a birdcage to design a simple double-tuned proton/phosphorus coil for human calf muscle studies at 7 t. *Concepts in Magnetic Resonance Part B: Magnetic Resonance Engineering*, 39(2):89–97, 2011.

[121] H. Wen, F. A. Jaffer, T. J. Denison, S. Duewell, A. S. Chesnick, and R. S. Balaban. The evaluation of dielectric resonators containing h_2o or d_2o as rf coils for high-field mr imaging and spectroscopy. *Journal of Magnetic Resonance, Series B*, 110(2):117–123, 1996.

[122] A. R. West, T. B. Adams, F. D. Morrison, and D. C. Sinclair. Novel high capacitance materials:-batio 3: La and cacu 3 ti 4 o 12. *Journal of the European Ceramic Society*, 24(6):1439–1448, 2004.

[123] L. Winter, P. Kellman, W. Renz, A. Gräßl, F. Hezel, C. Thalhammer, F. von Knobelsdorff-Brenkenhoff, V. Tkachenko, J. Schulz-Menger, and T. Niendorf. Comparison of three multichannel transmit/receive radiofrequency coil configurations for anatomic and functional cardiac mri at 7.0 t: implications for clinical imaging. *European radiology*, 22(10):2211–2220, 2012.

[124] L. Winter, C. Özerdem, W. Hoffmann, D. Santoro, A. Müller, H. Waiczies, R. Seemann, A. Graessl, P. Wust, and T. Niendorf. Design and evaluation of a hybrid radiofrequency applicator for magnetic resonance imaging and rf induced hyperthermia: electromagnetic field simulations up to 14.0 tesla and proof-of-concept at 7.0 tesla. *PloS one*, 8(4):e61661, 2013.

[125] Q. Yang, J. Wang, and X. Zhang. Analysis of wave behavior in lossy dielectric samples at high field. *Magnetic Resonance in Medicine*, 47(5):982–989, 2002.

[126] V. L. Yarnykh. Actual flip-angle imaging in the pulsed steady state: a method for rapid three-dimensional mapping of the transmitted radiofrequency field. *Magnetic resonance in Medicine*, 57(1):192–200, 2007.

[127] A. Zhu, Z. Chen, J. Lv, and J. Liu. Characteristics of ac-biased plasma antenna and plasma antenna excited by surface wave. *Journal of Electromagnetic Analysis and Applications*, 4(7):279–284, 2012.

SUMMARY

In this thesis novel transmitter designs for human magnetic resonance imaging for high static magnetic field strengths (7 Tesla) were developed. The theory for both dielectric resonators as well as plasma based resonators have been described in the introduction and outline.

It was shown that by using empirically derived formulas and computer simulations dielectric resonators can be designed also by using water as a dielectric (**chapter 2**). Beside the design itself it was also shown that established techniques in the design of magnetic resonators like the more efficient quadrature drive. Especially a first method to detune the dielectric resonator is essential for the future work of these resonators in magnetic resonance imaging if combination with high density receiver arrays is desired.

In **chapter 3** it was shown that alternative dielectric materials, especially high dielectric materials can be used instead of water. This opens the field for even more compact and more efficient designs. The technology of dielectric resonators for magnetic resonance imaging was further improved by showing solutions for fine tuning ceramic based resonators.

Chapter 4 shows the advanced usage of the technology developed in chapter 2 and chapter 3. Here an array for human cardiac magnetic resonance imaging at 7 Tesla field strength was designed and constructed. The dielectric resonators were used as an alternative to loops as surface coil elements. The performance of the loop coil and the dielectrics resonator was compared and showed similar performance for both designs.

In **chapter 5** a first practical design for a plasma based transmit coil for magnetic resonance imaging was demonstrated. It was shown that it is possible to guide a surface wave via the plasma sheath within the magnetic resonance imaging system.

The thesis ends with **chapter 6** a general discussion and an outlook to possible future developments. Both new resonator designs that were investigated in this thesis have still a lot of potential for improved future designs and and innovations. Especially the combination of dielectric resonators with receive arrays, an alternative coupling scheme and improved dielectrics are fields of interest for future research. As the theory of both plasma and dielectric resonators is well understood improved practical designs are desirable as a next step in this field of research on transmitter designs for magnetic resonance imaging.

SAMENVATTING

Dit proefschrift beschrijft de ontwikkeling van nieuwe radiofrequente (RF) zendspoelen voor magnetische resonantie beeldvorming (MRI) in de mens, in het specifiek voor hoogveld MRI systemen op 7 Tesla. Deze systemen zijn vele malen krachtiger dan standaard MRI systemen en laten hierdoor meer detail zien. De hieraan gekoppelde toename van de radiofrequentie leidt er echter toe dat nieuwe ontwerpen voor RF zendspoelen nodig zijn om deze systemen optimaal in te zetten. Dit proefschrift is daarom gewijd aan de ontwikkeling van zowel diëlektrische resonatoren alsook plasma-gebaseerde resonatoren, waarvoor een beknopte achtergrondtheorie staat beschreven in de inleiding (**hoofdstuk 1**).

Allereerst wordt aangetoond dat, door gebruik te maken van empirisch afgeleide formules en computersimulaties, diëlektrische resonatoren als RF zendspoel kunnen worden ontworpen door water als een diëlektricum te gebruiken (**hoofdstuk 2**). Naast richtlijnen voor het ontwerp wordt ook aangetoond dat gevestigde technieken, zoals de meer efficiënte kwadratuuraandrijving, eveneens toegepast kunnen worden op deze structuren. Daarnaast presenteren we een eerste methode om de verkregen diëlektrische resonator dynamisch af te stemmen, wat essentieel is voor het gebruik van deze resonatoren in combinatie met meerderkanaals ontvangstspoelen.

In **hoofdstuk 3** wordt aangetoond dat alternatieve diëlektrische materialen, met name keramische materialen met een hoge diëlektrische constante, ook kunnen worden gebruikt voor het ontwerp van diëlektrische resonatoren als RF zendspoel. Dit biedt mogelijkheden voor compactere en efficiëntere ontwerpen dan wanneer hiervoor water gebruikt wordt. De technologie van diëlektrische resonatoren voor MRI wordt verder verbeterd door oplossingen te tonen voor het nauwkeurig afstemmen van de op keramiek gebaseerde resonatoren.

Hoofdstuk 4 toont het geavanceerde gebruik van de zendtechnologie die is ontwikkeld in hoofdstuk 2 en hoofdstuk 3. Hier is een rangschikking van meerdere diëlektrische resonatoren ontwikkeld voor toepassing op 7 Tesla MRI systemen. De diëlektrische resonatoren worden hierbij vergeleken met conventionele elementen gebaseerd op lusvormige oppervlaktespoelen, met vergelijkbare prestaties.

In **hoofdstuk 5** wordt een eerste praktisch ontwerp voor een op plasma gebaseerde zendspoel gedemonstreerd. Er wordt aangetoond dat het mogelijk is om een oppervlaktegolf via de plasmamantel van een commerciële TL-buis te geleiden en te gebruiken voor MR

excitatie. NMR spectra en MRI beelden zijn verkregen door de op plasma gebaseerde zendspoel te combineren met een conventionele op koper gebaseerde ontvangstspoel.

Het proefschrift eindigt met in **hoofdstuk 6** een algemene discussie en een vooruitblik op mogelijke toekomstige ontwikkelingen. De beide nieuwe resonatorontwerpen die in dit proefschrift zijn onderzocht bieden nog veel potentieel voor toekomstige verbeteringen en verdere innovaties. Vooral de combinatie van diëlektrische resonatoren met meerderkanaals ontvangstspoelen, alternatieve koppelingsmethoden en verbeterde diëlektrische materialen met lagere verliezen zijn veelbelovende gebieden voor toekomstig onderzoek. Aangezien de theorie van zowel plasma- als diëlektrische resonatoren middels dit proefschrift goed gefundeerd zijn, zijn vervolgstappen voor verbeterde ontwerpen wenselijk in de zoektocht naar efficiëntere zendstrategieën voor MRI.

CURRICULUM VITÆ

Sebastian Arnold AUSSENHOFER

Sebastian Arnold Aussenhofer was born on July 22nd in 1981 in Karlstadt, Germany. He was trained as a biological technical assistant at the Biozentrum of the Julius-Maximilians-Unversity of Wuerzburg from 1998 to 2002. After his training he worked as a technical assistant at the Institute for Experimental Physics Department V at the University of Wuerzburg. Sebastian studied from 2005 to 2010 at the School of Applied Science Hochschule Ulm in Germany and graduated as Diplomingenieur in Medical Engineering. After a short excursion to the medical device industry in 2010 he joined the C.J. Corter Center for High Field MRI at the Leiden University Medical Center in the Netherlands as a graduate student for his PhD. His thesis with the title "Novel Transmitter Designs for Magnetic Resonance Imaging" was in the subject of hardware development for magnetic resonance imaging under the supervision of Prof. Dr. A. Webb.

After his thesis Sebastian joined the medical device industry again and is working since then as project manager for NORAS MRI products GmbH in Germany. He mainly works on MRI guided intervention devices and the coordination of EU funded research projects.

During his time as a PhD student Sebastian was awarded with the ISMRM Merit award magna cum laude in 2012 for his Abstract "A quadrature HEM_{11} mode resonator as a new volume coil for high field MRI" and also in 2013 with the ISMRM Merit award magna cum laude for his abstract on "Design of a Resonant Ceramic Array for Cardiac Imaging at High Field Strengths".

Sebastian is married and has one child. In his free time he enjoys books and tries to improve his command of the Chinese language.

List of Publications

JOURNAL PUBLICATIONS

1. **S.A. Aussenhofer** and A.G. Webb, *Design and evaluation of a detunable water-based quadrature HEM_{11} mode dielectric resonator as a new type of volume coil for high field MRI*, Magnetic Resonance in Medicine **68**, 1325-31 (2012).

2. **S.A. Aussenhofer** and A.G. Webb, *High-permittivity solid ceramic resonators for high-field human MRI.*, NMR in Biomedicine **243**, 11 1555-61 (2013).

3. **S.A. Aussenhofer** and A.G. Webb, *An eight-channel transmit/receive array of TE01 mode high permittivity ceramic resonators for human imaging at 7T.*, Journal of Magnetic Resonance **26**, 122-9 (2014).

4. **S.A. Aussenhofer** and A.G. Webb, *Evaluation of plasma-based transmit coils for magnetic resonance*, Journal of Magnetic Resonance **261**, 49-53 (2015).

5. A.G. Webb, N.B. Smith, **S.A.Aussenhofer** and H. Kan, *Use of tailored higher modes of a birdcage to design a simple double tuned proton/phosphorus coil for human calf muscle studies at 7T.*, Concepts in Magnetic Resonance, 89-97 (2011).

6. P.W. de Bruin, P. Koken, M.J. Versluis, **S.A. Aussenhofer**, I. Meulenbelt, P. Boernert, and A.G. Webb, *Time-efficient interleaved human 23Na and 1H data acquisition at 7 T.* NMR in Biomedicine., 28, 1228–1235(2015).

7. A.J. Gonzales, S. Majewski, F. Sanchez, **S.A.Aussenhofer** and J.M. Benlloch, *The MINDView brain PET detector, feasibility study based on SiPM arrays.*, Journal of Nuclear Instruments and Methods in Physics Research Section A, 818, 82- 90. (2016).

CONFERENCE PROCEEDINGS

1. A.J. Gonzales, S. Majewski, F. Sanchez, **S.A.Aussenhofer** and J.M. Benlloch, *A novel brain PET insert for the MINDView project.*, IEEE Nuclear Science Symposium and Medical Imaging Conference(NSS/MIC)(2014).

2. **S.A.Aussenhofer**, J. Hubensteiner, and A. G. Webb. A quadrature HEM11 mode resonator as a new volume coil for high field MRI. 20th Annual ISMRM Meeting. Melbourne, Australia (2012). Awarded with the ISMRM Merit award magna cum laude.

3. **S.A.Aussenhofer**, and A. G. Webb. Design of a resonant ceramic array for cardic imaging at high field strengths. 21st Annual ISMRM Meeting. Salt Lake City, USA (2013). Awarded with the ISMRM Merit award magna cum laude.

4. **S.A.Aussenhofer**, and A. G. Webb. Plasma based MRI. 23rd Annual ISMRM Meeting. Toronto, Canada (2015).

5. **S.A.Aussenhofer**, and A. G. Webb. A large volume HEM dielectric resonator for musculoskeletal applications at ultra high field. 22nd Annual ISMRM Meeting. Milan, Italy (2014). Traditional Poster.

6. **S.A.Aussenhofer**, and A. G. Webb. A hybrid dielectric/birdcage double tuned volume resonator for high field MRI. 22nd Annual ISMRM Meeting. Milan, Italy (2014). Traditional Poster.

7. **S.A.Aussenhofer**, and A. G. Webb. A variable diameter resonator for high field proton and sodium musculoskeletal MRI. 22nd Annual ISMRM Meeting. Milan, Italy (2014). Traditional Poster.

8. **S.A.Aussenhofer**, and A. G. Webb. High permittivity solid ceramic resonators for High Field Human MRI. 21st Annual ISMRM Meeting. Salt Lake City, USA (2013). Traditional Poster.

9. **S.A.Aussenhofer**, and A. G. Webb. Flexible radiative antennas as transmit elements for high field MRI. 20th Annual ISMRM Meeting. Melbourne, Australia (2012). E-Poster.